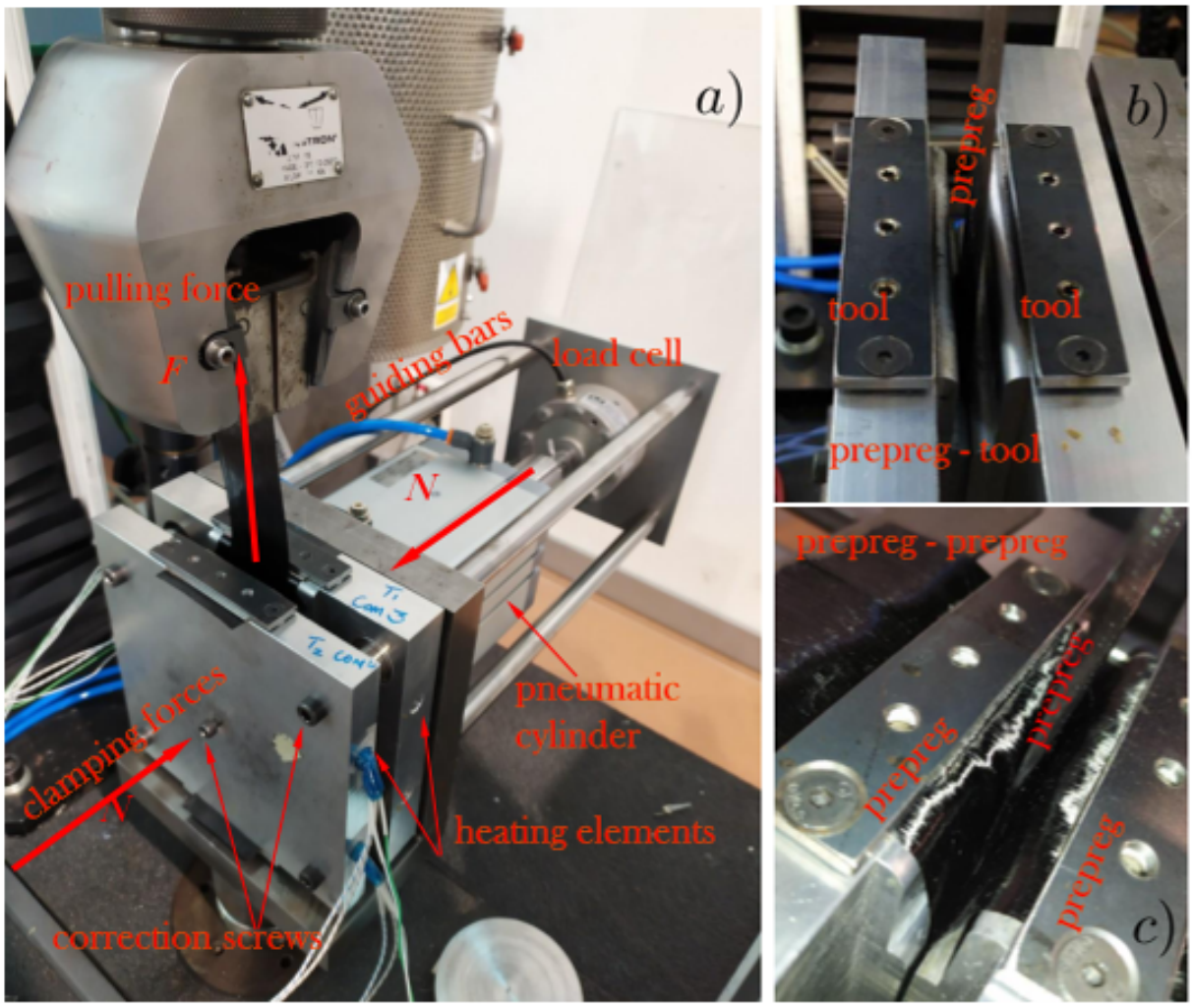

Figure 2.16: a) Experimental set-up used for measuring friction coefficient, b) Test for prepreg-tool friction measurement, c) Test for prepreg-prepreg friction measurement.

prepreg contact experiments. For the ply-ply tests, the aluminium plates are covered with wider prepreg sheets to keep the friction coupon in constant contact with the prepreg. The cover and sample fibres have the same orientation. The prepreg samples were also maintained at room temperature for at least one hour before the tests to unfreeze and climate them.

Before the tests, a procedure was carried out to guarantee uniformity of the clamping pressure. Such a procedure consisted of clamping the prepreg material sheet between the metal plates and inserting a set of eight pouch pressure sensors (Flexiforce A201 by Tekscan™Inc.). The five correction screws machined in the aluminium plate were manipulated, fastening or losing, until the voltage signals of the eight sensors were similar within the experimental scatter. The calibration procedure was carried out daily, setting the clamping pressure to an expected value. In this study, the clamping pressure p, temperature T and pulling speed $\dot{U}$ were 0.5, 1, 2 bars, 40 and 60 °C and 1, 3, 5 and 10 mm/min, respectively. These test settings were

chosen since they are the standard at which this specific material is thermally formed. At least five valid tests were performed for each of the conditions described to get statistical values of the frictional behaviour resulting in a total of 240 friction tests.

The coupons were 300×45 mm^2 in size and were tested with the longest dimension parallel to the fibres and pull-out direction. The friction coefficient is then obtained as the ratio $\mu = F/2N$ where F stands for the applied pulling force, and N is the normal clamping force. The factor of two used in the latter expression is because the contact surface of the pull-out specimen with the gripping system is double. The friction coefficient is calculated when the pulling load is sufficiently stabilised in the displacement range of the tests.

2.5 Compaction analysis of uncured prepreg composite laminates

The pursuit of ideal results in the thermoforming manufacturing process requires a comprehensive look at the consolidation process of thermoset composites, which includes the compaction effect of the plies within the laminate. By ensuring a strong bond between the fibres and the matrix, the consolidation process reduces the possibility of voids or air entrapment, both of which are unfavourable to the mechanical characteristics of composites. The phenomenon of fibre bed is a significant feature that is observed during the compaction of plies, and it is associated with the behaviour of fibres during compaction, wherein they tend to approach each other, releasing any excess resin or trapped air, and resolving voids or gaps within the laminate. This, consequently, results in enhanced load transfer and impedes the propagation of cracks. The potential manifestation of this effect may be subject to the influence of diverse process parameters, such as temperature, applied pressure, compaction velocity, and the sequence of plies in the laminate. The significance of analysing the fibre bed effect lies in its substantial impact on the final thickness profile of the component, proper distribution of residual stresses, reduction of distortion, and assurance of shape accuracy. Additionally, it plays an essential role in science-based process modelling. Comprehending the phenomenon of the fibre bed effect can assist in minimising process-induced imperfections such as wrinkles, bridging, and fibre misalignment while optimising process parameters such as vacuum debulking time, curing temperature, pressure, and resin viscosity. Typically, a compaction test is conducted using a universal testing machine that features compressive plates that are adjusted to be parallel to each other (Figure 2.17a). The sample is then positioned between these plates and subjected to compression loading. Numerous reports can be found in the literature regarding the implementation of compaction testing on prepreg composite materials, including both unidirectional (Hubert and Poursartip, 2001a; Nixon-Pearson et al., 2017; Valverde et al., 2021) and woven (Naresh et al., 2021) ply configurations. Usually, these inquiries are conducted with respect to industrial production consolidation as an ultimate step executed within an autoclave. Consequently, the experimental parameters are associated with this particular phase of the procedure. In the context of our case study, the compaction test will be related to a preliminary consolidation process that is executed during the lamination process against the metallic mould or any other forming system considered, immediately prior to the autoclaving stage. The primary distinctions between the two scenarios will certainly be

the applied pressure, the velocity of consolidation, and the duration of the process. Several similarities were identified, including the dimensions of the sample, the stacking sequences of the laminate, and the processing temperatures.

Some of the test conditions were simple to specify since they correlated to studies that have already been conducted or to actual manufacturing procedures used in the industries (Nixon-Pearson et al., 2017). The present investigation analysed the stacking sequences of $[0]_8$, $[0/90]_{4s}$, and $[90_4/0_4]_2$. The first stacking sequence is thought to be the most practicable for achieving a fibre bed effect since the fibres in this type of laminate lie parallel to each other, facilitating compaction and reducing the formation of resin-rich concentrations. The $[0/90]_{4s}$ laminate is widely regarded as the most suitable for demonstrating consolidation defects due to the perpendicular orientation of the fibres situated between the plies, which presents complications for fibre compaction (Valverde et al., 2021). The final stacking sequence under consideration aims to analyse the combined impact of the previously mentioned layouts. Throughout all aspects of the research, a consistent temperature range has been implemented. In the present testing instance, identical values of RT, 40°C, and 60°C were employed. Although the strain rate may not be a highly significant parameter in this analysis, it is interesting to point out that a value of 0.5 mm/min was established for this purpose. The previous value denotes the minimum velocity that has been taken into account in most of the testing procedures included in the present study. This value was selected due to the potential impact that a more abrupt strain rate could have on the disposition of the fibre during the compaction process. The dimensions of the sample were limited by the plates installed in the fixture. Consequently, a square sample measuring 30×30 mm^2 was customised, which closely resembles the sample utilised by Valverde et al., 2021. The samples utilising 8 plies are projected to have a thickness of 1.65 mm, whereas those utilising 16 plies are expected to have a thickness of 3.2 mm.

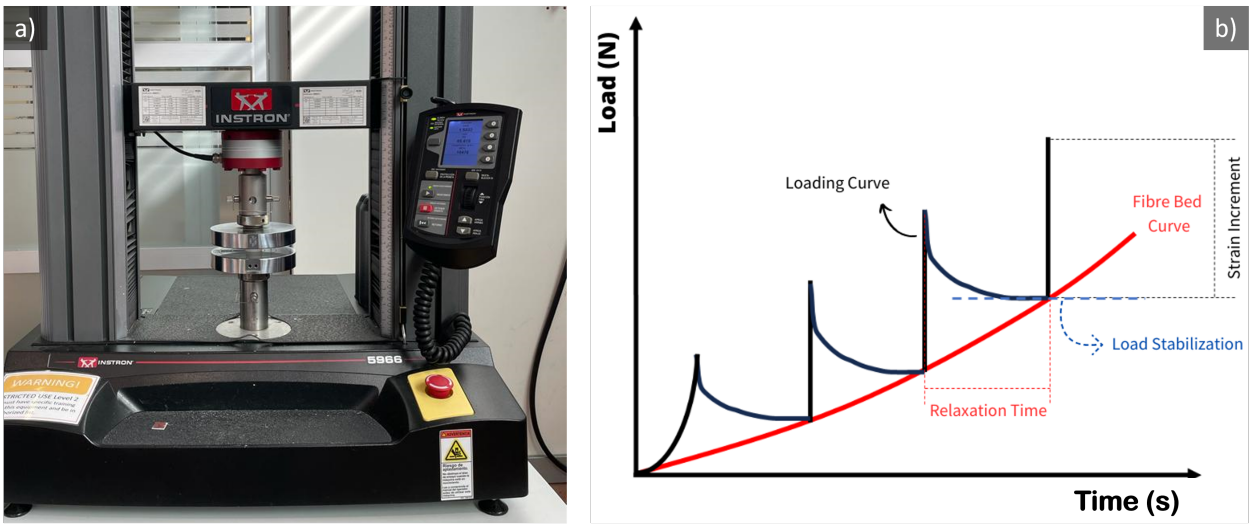

Figure 2.17: a) A fixture for the compaction test with two parallel plates mounted on a universal testing machine. b) A typical load vs displacement plot from the compaction test, displaying the fibre bed curve.

Despite the absence of a standardised method, there are various factors that necessitate

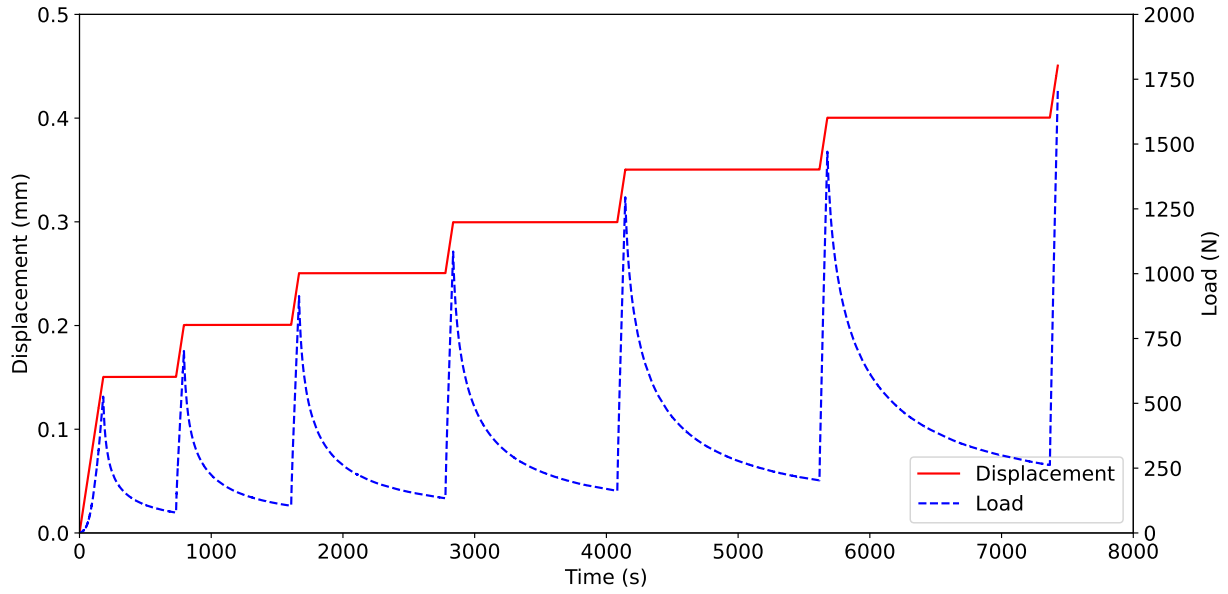

Figure 2.18: A visual representation of load and displacement curves plotted against time, providing insight into the displacement cycle and the corresponding load readings.

consideration when employing the compaction testing technique. The specimen undergoes compression through a strain control mechanism at regular intervals, utilising a procedure that comprises alternating periods of compaction and relaxation. The compressive action not only causes the fibre to concentrate, but it also causes the release of resin excess in a process known as resin bleed out or resin bleeding (Hubert and Poursartip, 1998a), which will consolidate the fibres inside the remaining resin, ensuring a final laminate thickness. As a result, it is critical to evaluate the features that regulate this phenomenom, which are the initial percentage of strain and relaxation time frame. In the preliminary phase, a determination was made to set the relaxation period at 10 minutes. However, this duration proved to be excessive for our specific scenario, as the load had already reached a state of equilibrium prior to the end of the specified time frame under the given initial strain of 20%. Considering the objective of maximising the overall testing efficiency, the relaxation period was set to a constant duration of 7 minutes. During the examination of the initial strain amount applied to the sample, various values, including 20%, 30%, and 40%, were taken into account. It was observed that the selected values have an impact on the stabilisation time and can either decrease or increase the relaxation time required. Similarly, the performance and response of the evaluated laminate layout will fluctuate. Hence, due to the numerous uncertainties involved and given that the primary objective of the experiment was to obtain the fibre bed effect curve, a variable relaxation time was utilised based on the observations made during the real-time data acquisition process reflected in Figure 2.18. The stabilisation of the load is considered the primary criterion for indicating the conclusion of the relaxation process, which refers to the point at which the load value ceases to vary and remains constant. This behaviour is visually depicted in Figure 2.17b by a segmented blue line.

In the context of strain, it has been established that an initial value of 10% yields a satisfactory

force response for initiating compression. Subsequently, incremental compressions of 0.05 mm are applied, corresponding to a strain of 3% for a sample with a thickness of 1.65 mm (See Figure 2.18). For the samples with a thickness of 3.6 mm, the initial strain value of 10% will be utilised, however, the required increments need to be larger, with values of 0.1 mm comparable to 2.75%. The final result of the test is a curve of the relationship between load and displacement, which enables multiple observations of displacement increments and relaxation lapses. Certain authors decide to present this particular curve using stress and strain units. However, a shared practise involves the drawing of a line that connects the points where the relaxation process is interrupted by a new displacement or strain increment. Figure 2.17b depicts the Fibre Bed Curve, which is visually distinguished by the colour red, and it will be considered the main outcome of the test.

2.6 2-point flexural test of uncured composite laminates

The semi-solid state of the material under investigation limits its ability to conduct certain sorts of loading, as stated in another section of this thesis. The standard three-point and four-point bending tests come to be unsuitable due to the presence of rigid components in the test fixtures, which improperly trigger deformation of the sample and create a localised area of stress concentration rather than achieving the intended loading condition (Paimushin et al., 2019). In the context of these tests, it is observed that the sample tends to experience indentation of the rigid contact regions within its body rather than the concentration of bending energy in the central region of the sample. A novel two-point bending apparatus is conceptualised for conducting flexural testing on uncured preimpregnated composite laminates (Figure 2.19a), regarding that while minimising the contact points, the possibilities of a failed test are lowered, and more energy is used in the proper loading case. However, it is necessary to have a minimum of two contact points in order to conduct our test. It is important to carefully consider these contact points, as reinforcement of the sample edges may be necessary to concentrate the bending energy on the right area of the sample.

2.6.1 Components analysis of the bending device

The novel device conceptualised at the IMDEA facilities operates on the same fundamental principle as a standard torsion apparatus, consisting of two centrally aligned components: a stationary and a moving part that rotates around the axis. In a conventional torsion testing procedure, the specimen is oriented such that the larger sample's side is aligned parallel to the axis of rotation. The modification made to this particular apparatus enables the user to orient the specimen perpendicular to the axis of rotation. This is achieved through the implementation of a mounting device that includes two notches into which the sample is inserted. Such positioning facilitates the application of bending loads to the specimen using a torsion device. The mounting apparatus comprises two PLA components fabricated using 3D printing technology, which are attached to the stationary and rotating parts of the device using holders that resemble a drill chuck. The notches present in the PLA pieces possess an exact width of 20 mm and a thickness of 3 mm. Although the dimensions of the sample are predetermined, it is feasible to have varying thickness values at the centre of the sample,

as long as the edges achieve the same thickness values as the notches. The desired effect can be accomplished through the inclusion of additional prepreg plies on the edges (Figure 2.22). This approach serves a dual purpose: first, it effectively secures the sample within the notches, preventing any unexpected rotation or displacement; second, it reinforces the edges of the sample, resulting in a concentration of bending forces towards the centre of the sample. The elongated section of the PLA pieces, which is attached to both the rotating and fixed components of the fixture, could possess varying dimensions and can be attached at different points to accommodate samples of different lengths. The installation of a small mirror at an inclination of 45° relative to the large edge of the sample has been performed employing a supplementary frame fabricated with 3D printing technology to firmly hold the mirror (Figure 2.19b). A camera is mounted above the apparatus, aligned with the upper surface of the specimen, and directed towards the mirror. The camera will acquire a longitudinal side view of the sample as a consequence of reflection. During the loading procedure, a video recording is conducted with the primary objective of documenting two key aspects: the bending angle exhibited by the sample and the potential occurrence of wrinkles in the sample. Also, a Novotechnik RFD-4000 magnetic rotary position sensor was put into the device so that the rotation angle of its rotatory part could be captured and measured. The sensor comprises two distinct components: one is attached to a stationary part of the device, while the other is attached to the rotating part. In order to ensure optimal performance, it is necessary that both components are precisely aligned and oriented towards each other, respecting the separation distance as stipulated by the manufacturer (Figure 2.19a). The rotational movements detected by the sensor are processed into electrical voltage signals. These voltage signals undergo a series of calibration processes to accurately determine the corresponding rotation angles. The measured angle corresponds to the rotational angle of the rotary component and should not be confused with the angle displayed by the sample during testing. The measured angle serves as a fundamental indicator for subsequent calculations, such as acceleration or establishing reference points.

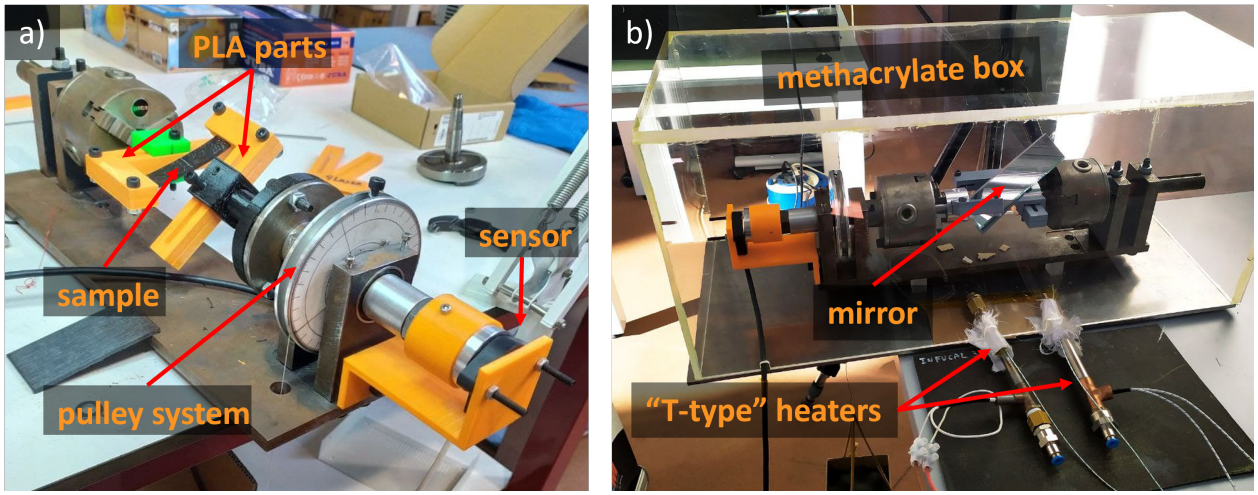

Figure 2.19: The two-points bending test (2PBT). a) Room temperature configuration and b) Increased temperature adaptation.

A transparent methacrylate frame was fabricated to facilitate the execution of tests at elevated

temperatures (Figure 2.19b). This frame serves the purpose of retaining heat within the system and enclosing the test rig, resembling a heat chamber. The frame underwent the drilling of two sockets on a singular side with the purpose of facilitating the connection of two "T-type" air process heaters (Figure 2.19b). These heaters are intended to generate and distribute hot air within the methacrylate box, maintaining a predetermined temperature as per the established requirements. The use of methacrylate, due to its translucency, enables the use of the camera without any disruptions or distortions in the captured images or multimedia content.

To facilitate the application of bending loading, a pulley system consisting of a wheel winding reel and a lightweight wire is installed within the rotatory component of the torsion fixture. On the opposite end of the wire, there is a small container that is securely attached. Within this container, small metallic blocks with specific weights are systematically placed one at a time. By utilising equation 2.7, it becomes possible to estimate the amount of load torsion (T_L) that is being transmitted to the sample by this pulley system.

$$T_L = mass \times gravity \times radius \tag{2.7}$$

2.6.2 Test Execution and Data Processing

The testing procedure begins by conducting an initial calibration of the device and its supplementary components. Given that the proper operation of the majority of device implementations is influenced by the accurate alignment of their components, it is imperative to meticulously examine each individual part within the test fixture. This examination should commence with an assessment of the stability of the working table, camera tripod, camera frame, mirror, device base, and sensor. In order to facilitate the positioning of the sample, the PLA components consist of two interconnected sections secured by five bolts and nuts. These fasteners can be disassembled to conveniently accommodate the sample within the designated notches. If a higher temperature is desired, the methacrylate frame is carefully positioned, initiating a pre-heat phase lasting for 10 minutes. The air process heaters are operated at an input temperature of around 200°C. This is done to facilitate the expulsion of hot air and maintain the test system at a steady temperature of 60°C. The temperature of the system is monitored through the use of thermocouples. After the fixture has been set up, there are certain steps that must be taken prior to loading the sample. It is necessary to prepare the appropriate weights intended for use in augmenting the load capacity. In our particular scenario, five weights weighing 100 grammes each were utilised, as depicted in Figure 2.21b. It is necessary to capture two photographs of the camera frame, ensuring that a scale, such as a ruler or other distance reference, is present within the frame. This is essential for subsequent calculations of the coordinates pertaining to various points of interest. We are now prepared to commence the recording process, which should ideally coincide with the initiation of the sensor acquisition system. This synchronisation is crucial for establishing a correlation between the visual images and the shifts in rotational position. Each increase in weight applied to the sample results in a corresponding bending of the sample until a specific angle is reached, at which point the sample will maintain the load and achieve equilibrium (see Figure 2.20a). The real-time data acquisition of the sensor allows for the observation of

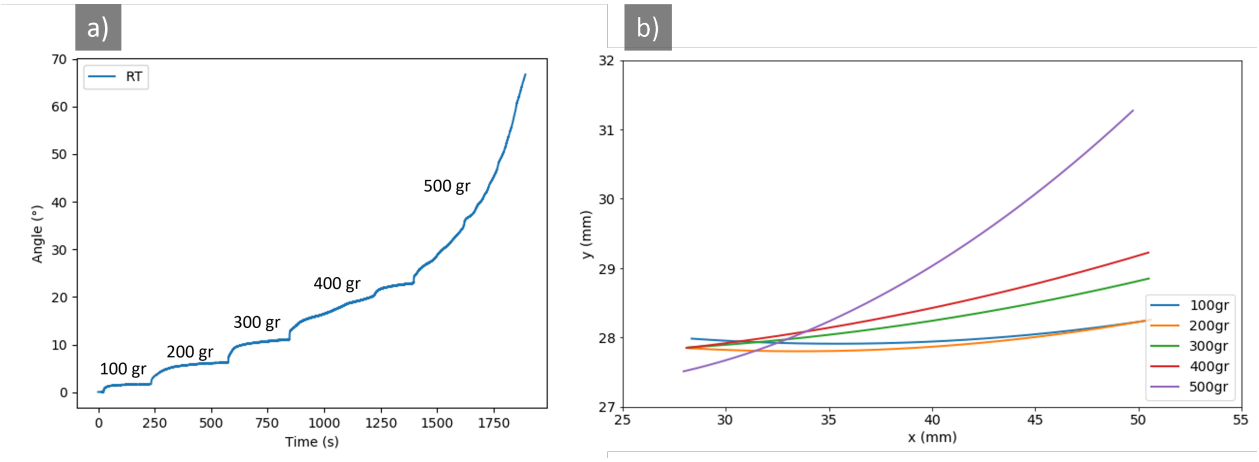

Figure 2.20: Real-time reading of bending test in progress. a) Angle variation over time due to weight increases as captured by the sensor. b) Estimation of sample curvature by fitting captured image coordinates at each weight increment.

this phenomenon. When no change in the angle is detected, it is appropriate to proceed with another weight increment.

The loading process will be completed after the sample reaches its maximum weight-bearing capacity and subsequently collapses. At this juncture, it is right to conclude the recording of both datasets and proceed to the subsequent phase of data analysis. The points of interest in our case study include the initial and final positions of the samples, the initiation and completion points of each weight increment, as well as any observed instances of wrinkle formation, which will be registered through picture capture from the video recording. This captured picture is thereafter subjected to processing using an image processor code. The specimen is marked with ten guiding lines that are spaced at 5 millimetre intervals to facilitate the recording of its coordinates at each increment of weight (See Figure 2.22). During the deformation of the sample, the coordinates provided will trace the arc deflection of the sample (see Figure 2.20b). This allows for the estimation of both the radius of the circumference and the angle produced between the fixed edge of the sample and a deflected point on the sample.

For every chosen point of interest, it is possible to approximate the coordinates of the market lines within the sample, determine the sample's curvature using a the polynomial function of degree two in equation 2.8, calculate the radius of curvature at the midpoint of the x domain following equation 2.9, verify the steady load torsion that the sample is capable of supporting with equation 2.7, determine the time of the event, and measure the rotation angle of the rotatory component of the device.

$$y(x) = ax^2 + bx + c \tag{2.8}$$

$$R = \frac{(1 + (2ax + b)^2)^{3/2}}{|2a|} \tag{2.9}$$

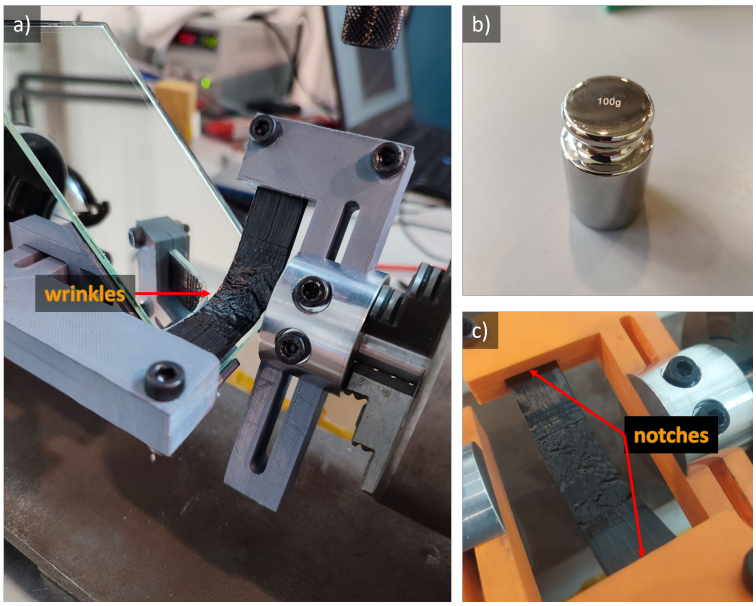

Figure 2.21: a) The presence of observable wrinkles on the surface of the sample, b) a standardised weight of 100g, and c) the positioning of the sample with the edges placed within the notches.

By calculating these variables, it is possible to construct diverse plots that can yield numerous conclusions. One potential capability provided by this device is the ability to analyse the formation of wrinkles on the sample. By utilising the aforementioned implementations, it is possible to visually record the precise instance at which wrinkles manifest on the surface or folds emerge along the edges of the specimen. Subsequently, these occurrences can be correlated with the specific bending force exerted or the bending angle maintained by the sample at the time of wrinkle formation. This knowledge could provide support for the implementation of damage theories in computational simulations that involve the bending deflections of preimpregnated composite laminates, particularly in the context of thermoforming manufacture.

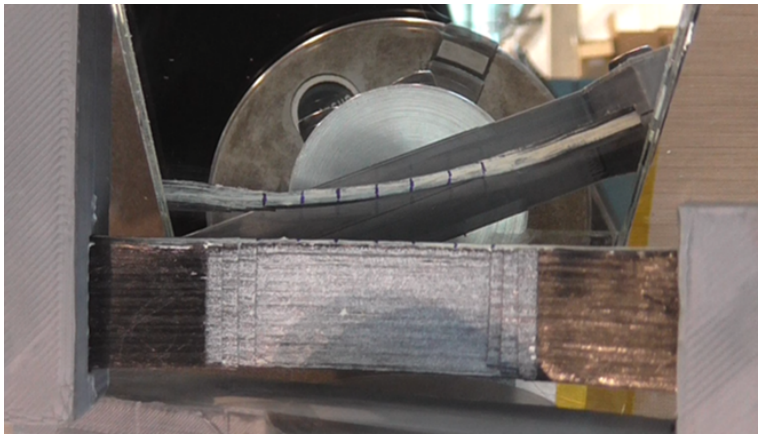

Figure 2.22: The camera frame captured during the testing process exhibits the upper portion of the sample, together with a longitudinal side view that shows a set of guiding marks.

Chapter 3

Experimental Results

A new experimental campaign was carried out, including the complete in-plane characterisation of the AS4/8552 prepreg composite and the interply friction study, after better understanding the behaviour of the uncured prepreg composite under specific testing conditions and making the necessary corrections to conduct its characterisation. As a solution to the interlayer sliding effect seen in untreated samples and responsible for inaccurately predicted mechanical properties, the novel partial curing manufacturing procedure explained in section 2.3.2, was put into effect for the samples used in the in-plane characterisation. Most recent measurements exhibit non-linear behaviour, and this chapter provides a thorough analysis of this phenomenon and the viscoelastic impact obtained by varying the test's displacement rate.

3.1 In-plane Mechanical Characterisation

3.1.1 Longitudinal Stress Test

Figure 3.1a displays the relation between stress and strain for the Normal Tensile Test at three different temperatures (RT, 40°C, and 60°C), with trends following a linear-elastic response exhibiting low values of strain due to the material's high stiffness along the fibre orientation. The curves for the temperatures of 40°C and 60°C are plotted until the sample reaches its maximum strength, which coincides with its failure. Since the DIC method cannot capture the strain after a sample has failed, its full extension has been omitted. Before reaching its maximum strength, the sample exhibits failure indicators, such as fissures in the matrix that separate the fibres into bundles. The 10 kN load cell integrated into the Instron machine constrained the data collected at room temperature.

Figure 3.1b shows a plot of the Young's Modulus vs temperature for the uncured AS4/8552 prepreg composite, which values can be found in table 3.1. Regardless of any limitations present during experimental testing, the quantity of data collected permits the Normal Tensile Modulus of the uncured prepreg to be calculated with accurate values based on the manufacturer-supplied values for the same material in its cured state. For the identical sample in its cured condition of the resin at 25°C, the manufacturer recorded a unique Young's Modulus of 141 GPa. The standard employed by the manufacturer for this test is left

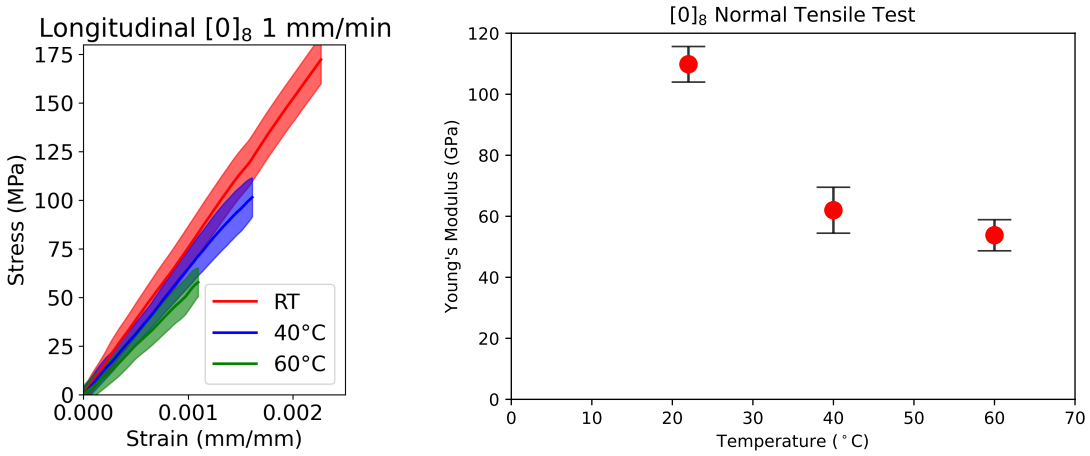

Figure 3.1: Stress-Strain curve for the normal tensile test at 22°(RT), 40°, and 60°.

unspecified. When we compare the young's modulus of cured and uncured samples under the same testing conditions, we find that the uncured sample strength is reduced approximately 50%. The normal elastic modulus of the uncured prepreg composite is reduced by another 13% when the temperature is raised from room temperature (RT) to 40°, and by almost another quarter (24%) when the temperature is raised to 60°.

Table 3.1: Uncured AS4/8552 0° Tensile Modulus for samples tested at a displacement rate of 1 mm/min at three different temperatures.

	RT(22 °C)	**40 °C**	**60 °C**
0° Tensile Modulus (GPa)	70,8 ± 4,4	62 ± 7,5	53,8 ± 5,1

3.1.2 Transverse Stress Test

The lack of resistance maintained by the fibres in the transverse loading direction puts in evidence the significant anysotropy found in laminated composite materials. In the context of composite laminates, it is commonly anticipated that a loading applied in the fibre direction will result in a high level of strength and stiffness. However, it is notable that the mechanical response of a composite lamina subjected to transverse loading tends to be poor. The transverse tensile test is a commonly used method to evaluate the mechanical response of both the matrix and the fiber/matrix interface. The early occurrence of damage in the laminate structure is a common issue with this tensile test. These damages typically originate as microflaws within the matrix and subsequently propagate throughout the interface. The ultimate breakdown of the composite material can be attributed to the process of microflaw nucleation, that eventually leads to the formation of a single crack. Initially, the existence of numerous microflaws does not indicate a decrease in the strength or rigidity of the material. However, over time, these microflaws may become the primary factor in determining the

outcome of the test. The plots in Figure 3.2 show the results of the tensile test conducted at temperatures of 40°C and 60°C, in which certain complications were experienced. Reducing the resin viscosity, along with the high volume of damage shown by this test, was producing several mismeasurements of the mechanical features with the samples exhibiting a rapid failure and unclear data acquisition at strain values above 5%.

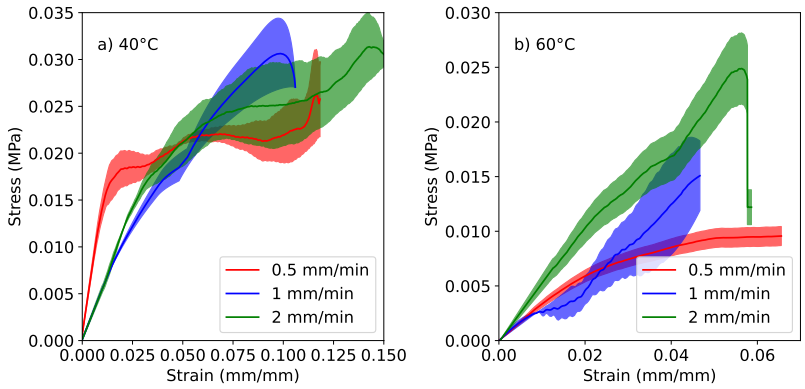

Figure 3.2: Mismeasurement of the transverse tensile test being conducted with the Instron universal testing machine together with a temperature chamber. a) Test conducted at 40°C degrees Celsius, and b) Test conducted at 60°C degrees Celsius.

Section 2.3.3 provides the analysis of the issue in question and a comprehensive description of the rheometer technique. This technique successfully yielded the desired stress-strain curve for each combination of conditions, surpassing the strain levels achieved in the previous standard transverse tensile test. Figure 3.3 depicts a comparative analysis of the Rheometer and Instron techniques, conducted at room temperature and a velocity of 2 mm/min.

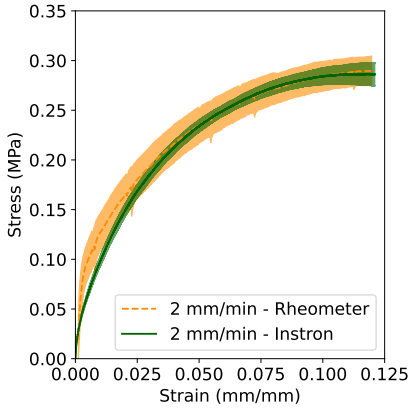

Figure 3.3: Comparative analysis of the stress vs strain response of a sample tested at room temperature with a strain rate of 2 mm/min using Rheometer and Universal testing machine.

The stress-strain response recorded during the transverse tensile test is depicted in Figure 3.4. In contrast to the longitudinal test, the experiment employed a variable displacement rate in order to measure the viscoelastic behaviour that arises from the resin's uncured condition.

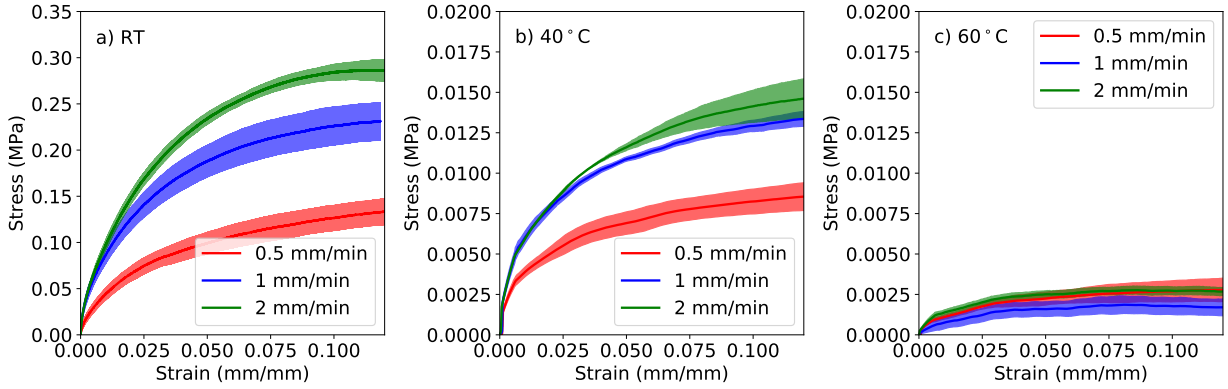

Figure 3.4: Stress-strain response of the transverse tensile test. a) The experiment was conducted at room temperature employing a universal testing machine to apply three different strain rates. b) The experiment was carried out at a temperature of 40°C using a rheometer to apply three different strain rates. c) The experiment was conducted at 40°C using a rheometer to apply three different strain rates.

Figure 3.4a shows the stress-strain response of the transverse tensile test carried out at room temperature while employing the Instron universal testing machine. This configuration did not display any complexities, and the curve demonstrated a non-linear characteristic corresponding to the expected behaviour of a semi-solid, given our consideration of the uncured resin. The test was terminated when a displacement of 15 mm was achieved by the clamps of the testing machine, equivalent to a strain of 12% and 30 minutes for the lower value of displacement rate. It is agreed that the specified strain level provides sufficient data to interpret the material's behaviour and that the thermoforming manufacturing process does not lead to large amounts of tensile deformation of the prepreg. The entire tensile test procedure reaches a point where the material's ultimate strength value is attained and then gradually decreases, nearly showing a "plateau" behaviour as the test progresses. Eventually, the propagation of cracks will gradually reduce the stress value until it reaches zero. The sample's failure is significantly impacted by fibre bridging, which possesses sufficient strength to prevent an abrupt reduction in the sample's strength despite the low stress level. Regarding the viscoelastic effect, it was simple to see how the change in strain rate affected the stress response by reporting a more significant strength as the strain rate increased. The "plateau" effect that was stated before was taking place at stress levels of 0.11, 0.225, and 0.28 MPa, which corresponded to strain velocities of 0.5, 1, and 2 mm/min, respectively. The stress levels increased by around 73% when the strain rate increased from 0.5 to 1 mm/min, and 115% increased from 0.5 to 2 mm/min.

Figure 3.4b illustrates the stress-strain behaviour of a transversal tensile test carried out in a rheometer with a chamber heated to 40°C. As at room temperature, the non-linear behaviour was again observed with similar development and morphology during testing. The most noticeable contrast observed corresponds to the reduction in stress levels, which accounts for nearly 95% of the loss in strength due to the impact of temperature for all three scenarios investigated. The study showed the presence of a viscoelastic phenomenon in which the stress level increased with a corresponding increase in the strain rate. However, a unique observation

was made when the strain rate was increased from 1 to 2 mm/min, as it did not cause a significant rise in the stress response. In the scenario of room temperature, an increase from 1 to 2 mm/min resulted in a stress response augmentation of nearly 25%. However, at 40 degrees, the stress response remained relatively constant until a strain value of 0.03 mm/mm was reached. Subsequently, a slight divergence was observed, with a strength differential of 12%. The earlier observation holds significant importance, and its analysis highlights the impact of temperature and velocity on uncured prepreg composite materials. In the case of RT scenarios, the viscoelastic behaviour of the material indicates that the uncured prepreg composite adheres to a Newtonian pattern (See Figure 3.5b) that is governed by the following equation:

$$\tau = \mu \times \frac{\delta v}{\delta y} \tag{3.1}$$

Where τ denotes the shear stress, also referred to as viscous stress, μ is the viscosity of the material, and $\frac{\delta v}{\delta y}$ is the shear velocity or shear rate represented in our particular case by the displacement rate and is the only parameter that varies in the equation (See Figure 3.5a). The lack of a significant difference in the stress response between the shear rates of 1 mm/min and 2 mm/min at a temperature of 40°C suggests that the shear velocity is not the only parameter that remains constant with these conditions. It is possible to conclude that an increment in the shearing velocity resulted in changes in the viscosity value. The definition states that the prepreg material in its uncured state demonstrates non-Newtonian characteristics at a temperature threshold of 40°C, going into effect from a strain rate of 1 mm/min. For a non-Newtonian fluid to maintain constant shear stress while increasing the strain rate (also known as shear rate), the fluid's viscosity must decrease. The variety of non-Newtonian fluid exhibiting such behaviour is commonly called pseudoplastic. The visual illustration of its shear stress response to shear rate appears in Figure 3.5b.

The existence of non-Newtonian qualities in the prepreg composite becomes more noticeable with a rise in temperature to 60°C and a corresponding reduction in viscosity. Figure 3.4c indicates that the stress response remains unaffected by the strain rate or shear rate, as evidenced by the overlapping of the three curves corresponding to the three strain rates tested. Similar behaviour of the sample was observed, although with a higher incidence of defects that resulted in the test stopped prematurely. Nevertheless, sufficient data was obtained for subsequent calculations, and the test achieved a strain value exceeding the requisite of 15%. Even in the absence of the viscoelastic effect and the low stress response, the stress-strain curve exhibits a plateau effect for this scenario. The convergent point of the three curves occurs at an approximate value of 0.0025 MPa. By considering the green curve, which corresponds to a strain rate of 2 mm/min for all plots, it can be calculated that the stress response decreased by 88% between 40 and 60 degrees and by 99% between room temperature and 60 degrees. At this temperature range, the resin undergoes a transition to a gel state, exhibiting a diminished solid-like behaviour and displaying more fluid-like characteristics.

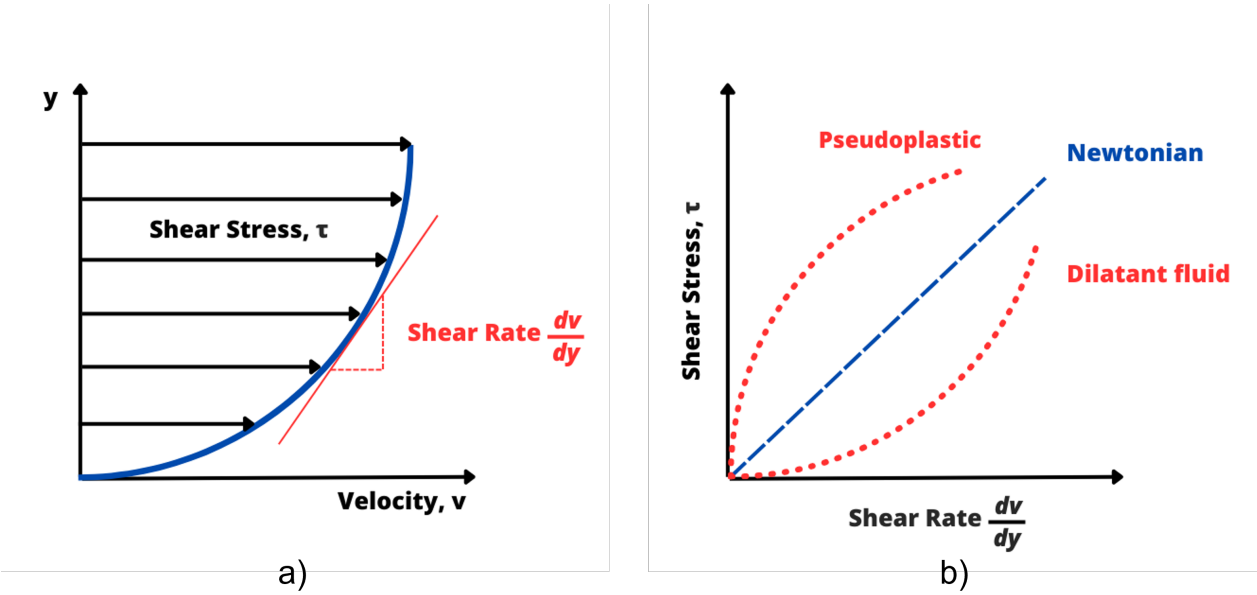

Figure 3.5: The viscosity's behaviour. a) Shear stress response dependent on shear rate, and b) Newtonian and non-Newtonian viscosity behaviour.

3.1.3 Shear Stress Test

The present tensile test methodology employs a specimen that exhibits a specific stacking sequence, wherein plies featuring fibre orientation at +45 and -45 degrees are arranged in an alternating sequence, settling in a laminate that fulfils an imposed symmetry condition. The main objective of imposing this symmetry is to ensure a uniform distribution of loads within the laminate during testing, considering that both tensile and compressive loads are expected. By achieving this uniformity, the methodology effectively prevents the occurrence of undesirable phenomena such as torsion or premature damage initiation, which have the potential to compromise stress measurements and yield an inaccurate representation of the material's behavior. This particular laminate configuration exhibits enhanced strength, thereby enabling the specimen to retain its structural integrity during testing, even under conditions of elevated temperature and reduced resin viscosity. This capability enables the utilisation of the universal testing machine for any of the mentioned cases along with the standard method D3518, 2007, overcoming the need for supplementary methodologies such as rheometry, which were previously necessary for conducting the transverse tensile test. Figure 3.6 provides a comprehensive overview of the outcomes, revealing a prevailing non-linear stress response across all cases, consistent with the findings of the prior testing configuration. The initial stress response of the RT and 40°C curves exhibits a nearly linear slope until a strain value of around 1.5%. Consequently, it was determined to augment the quantity of images captured for digital image correlation (DIC) analysis in the initial quarter to procure additional data for characterising this phenomenon. Subsequently, the number of images taken was reduced. It is feasible to observe the change in the rate of image capture by examining the curves, as a slight dent in the curve becomes visible at a shear strain value around 3%.

The curves exhibit properties that correspond to in-plane shear stress (τ_{12}) and ply shear

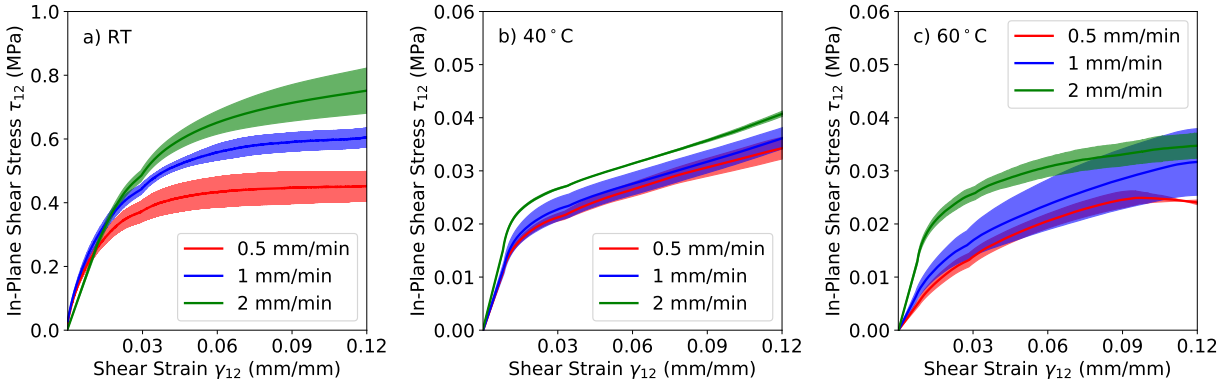

Figure 3.6: $[\pm 45]_{2s}$ Shear Tensile Test employing a universal testing machine at three different strain rates. a) Test conducted at RT, b) Test conducted at a temperature of 40°C and c) Test conducted at a temperature of 60°C.

strain (γ_{12}), which formulation was specified in section 2.3.2. In the case of RT, it is observable that the curves exhibit a plateau trend from the midpoint of the curve towards the reach of the maximum strain value, which is at 12%. This maximum strain value was selected because it is feasible to gather sufficient data for the analysis at this strain level, thereby shortening the time required for data acquisition while maintaining a similarity with the other test cases. Upon examination of the final stress level recorded during the test, specifically at the point where the plateau effect becomes apparent, stress values of 0.45, 0.57, and 0.72 MPa were identified. These values correspond to the three distinct strain rates that were evaluated, for instance, 0.5, 1, and 2 mm/min. The variations in stress level responses are associated with a 70% increase from the minimum strain rate to the maximum. However, if we focus on the increases from the first to the second and the second to the third, we may detect a stress increase of 35% and 26.5%, respectively. The strain rate undergoes a two-fold increase from its initial value, followed by a subsequent four-fold increase. However, the stress increments do not exhibit a similar trend. The presence of fibre resistance may exert an influence on the final stress estimation and may be accountable for the aforementioned effect.The RT evaluation was the only scenario where viscoelasticity could be seen clearly, and it has the peculiar feature that the effect begins at a stress level of 0.2 MPa, corresponding to about 1.5% of strain right after overpassing the first linear-like slope of the curve. The initial linear response of the material is attributed to the fibres influence during the initial loading stages, followed by the matrix deformation. The viscoelastic response observed is a result of the matrix's sensitivity to the strain rate. Given that the resin is presently in an uncured state, the tendency for failure in these specimens begins with the rotation of the fibres in an attempt to align with the loading direction, thereby resulting in an increase in the load that is no longer indicative of shear in the $\pm 45°$ direction. Upon the initiation of this phenomenon, it becomes visible that there is a detachment of the prepreg plies, leading to the separation of the fibres from the resin, ultimately culminating in rupture. With the exception of the time when the rupture takes place, this effect and behaviour remain true for all of the different temperature scenarios evaluated.

The primary consequence of increased temperature is the significant reduction of the viscoelastic effect to an almost negligible extent as observed in Figure 3.6b. Given our assumption that the viscoelastic phenomenon arises from the reaction of the resin, our initial deduction from the observed data is that the stress response exhibited by the $\pm 45_{2s}$ off-axis samples at a temperature of 40°C is mostly influenced by the fibres. Once again, it is feasible to identify two distinct slopes inside the curves, as was seen in the case of the RT scenario. In previous investigations conducted on cured prepreg composite samples subjected to the same test setup, it has been found that the change in slope can be attributed to the development of transverse cracks in the resin-rich regions, also known as the interply zones. After conducting a thorough examination of the material, it has been determined that the aforementioned cracks were initially not present in our case study. However, significant elasto-plastic deformations have been noticed, which can account for the alteration in the slope of the stress-strain curve. Subsequently, the deformations are succeeded by the rotational movement of the fibres, culminating in the ultimate collapse of the samples through different crack events. In contrast to what was observed in earlier test cases, this curve did not exhibit a plateau effect. The explanation for this occurrence is that the viscosity of the resin is lowered, which enables the fibre to undergo unrestricted rotation within the sample during deformation. Given the inherent tendency of fibres to align themselves with the direction of loading, it is anticipated that the stress will increase. Within the strain range considered in our testing scenario, the second slope, beginning at a strain value of 1.5%, exhibits an elevation in the stress response from 0.02 to 0.038 MPa approximately, displaying a consistent linear trend up for the three strain rates.According to the findings presented in section 3.1.2 regarding the transverse loading instance, it was seen that the viscoelastic effect ceased within a similar temperature range. Consequently, the sample returned to displaying a non-Newtonian characteristic, wherein the viscosity of the resin fluid exhibited pseudoplastic behaviour.

Despite the lack of a substantial difference in the measured stresses when using different strain rates, there are still pertinent insights that may be derived from the data. For the strain rates of 0.5, 1, and 2 mm/min, the experiment resulted in stress responses of 0.026, 0.028, and 0.032 MPa, respectively. When considering the subtle distinctions, analysing the percentage increases offers a more lucid viewpoint. The percentage increase from the initial strain rate of 0.5 mm/min to the subsequent strain rate of 1 mm/min is calculated to be 7.7%. Likewise, the observed increment in strain rate from the second to the third instance, specifically from 1 mm/min to 2 mm/min, amounts to 14.3%. When examining the cumulative impact over the three strain rates, it is observed that the increase from the lowest to the greatest is 23%. Nevertheless, the feature that is most captivating and deserving of attention is the notable decrease in stress levels noticed when comparing measurements collected at standard room temperature (RT) with a temperature of 40°C. The most significant divergence was observed across the various strain rates, with the strain rate of 2 mm/min exhibiting a remarkable reduction of stress levels by 95%. This highlights the significance of temperature in shaping the characteristics of prepreg composites, particularly when subjected to high strain rates.

The final test configuration to be discussed involves subjecting the sample and the test configuration to a temperature of 60°C. The evolution of the test exhibited a high degree of similarity to the preceding case at a temperature of 40°C. The presence of a distinct viscoelastic effect in this particular situation remains unclear, as there is a little variation

in the stress response when subjected to different strain rates. However, it is evident that there is an observable rise in the level of noise present in the load being measured by the load cell. This effect specifically indicates a distinction in the behaviour of the sample in comparison to samples at 40°C. Although the stress levels of the curves are similar, ranging between 0.02 and 0.038 MPa, the shape of the curves differs, exhibiting a less pronounced transition from one slope to another. The observation suggests that the initiation of damage within the sample may occur earlier due to the quite inferior contribution of the resin to the distribution of stress. Additionally, it could serve as an indicator of the earlier onset of elastoplastic deformation. The sample that was exposed to a strain rate of 2 mm/min exhibited a trend that closely resembled the previous temperature case. Notably, there was a distinct transition from one slope to another, indicating that the sample displayed an elastic response before the onset of damage and elastoplastic deformation. In all three instances, an apparent plateau trend in the curve was not detected, which can be attributed to the freedom of the fibres to rotate and align themselves with the direction of loading.

3.2 Results of the pull-out test and calculations of the friction coefficients

The representative load-displacement curves $F - U$ corresponding to the tests carried out to measure the prepreg-prepreg friction for the experimental conditions previously described are gathered in Figure 3.7. The shape of the $F - U$ curves exhibits an initial linear increase of the pulling force up to an onset point in which specimen relative sliding started. After that point, the specimen was continuously extracted up to load stabilisation.

The results obtained for the two different temperatures had similar shapes but with smooth transitions of the $F - U$ curves during the whole test. In both cases, the effect of temperature and velocity strongly influences the shape of the curves suggesting a film-sliding friction mechanism. As expected, the increase in the temperature decreased the pull-out forces while increasing the pulling velocity produced the opposite behaviour. It is important to mention that the pressure also modifies the pull-out force increasing the value when pressure increases.

The friction coefficient was obtained as the ratio $\mu = F/2N$ where F stands for the applied pulling force, and N is the normal clamping force. The factor of two used in the latter expression is because the contact surface of the pull-out specimen with the gripping system is double. The friction coefficient was calculated when the pulling load was sufficiently stabilised in the displacement range of the tests. The friction coefficient μ as a function of the pulling velocity $\dot{U}$ is presented in Figure 3.8 for the prepreg-prepreg and prepreg-tool configurations. Table 3.2 gathers a summary of the prepreg-prepreg and prepreg-tool contact friction coefficients for the combination of the abovementioned variables with their corresponding standard deviation.

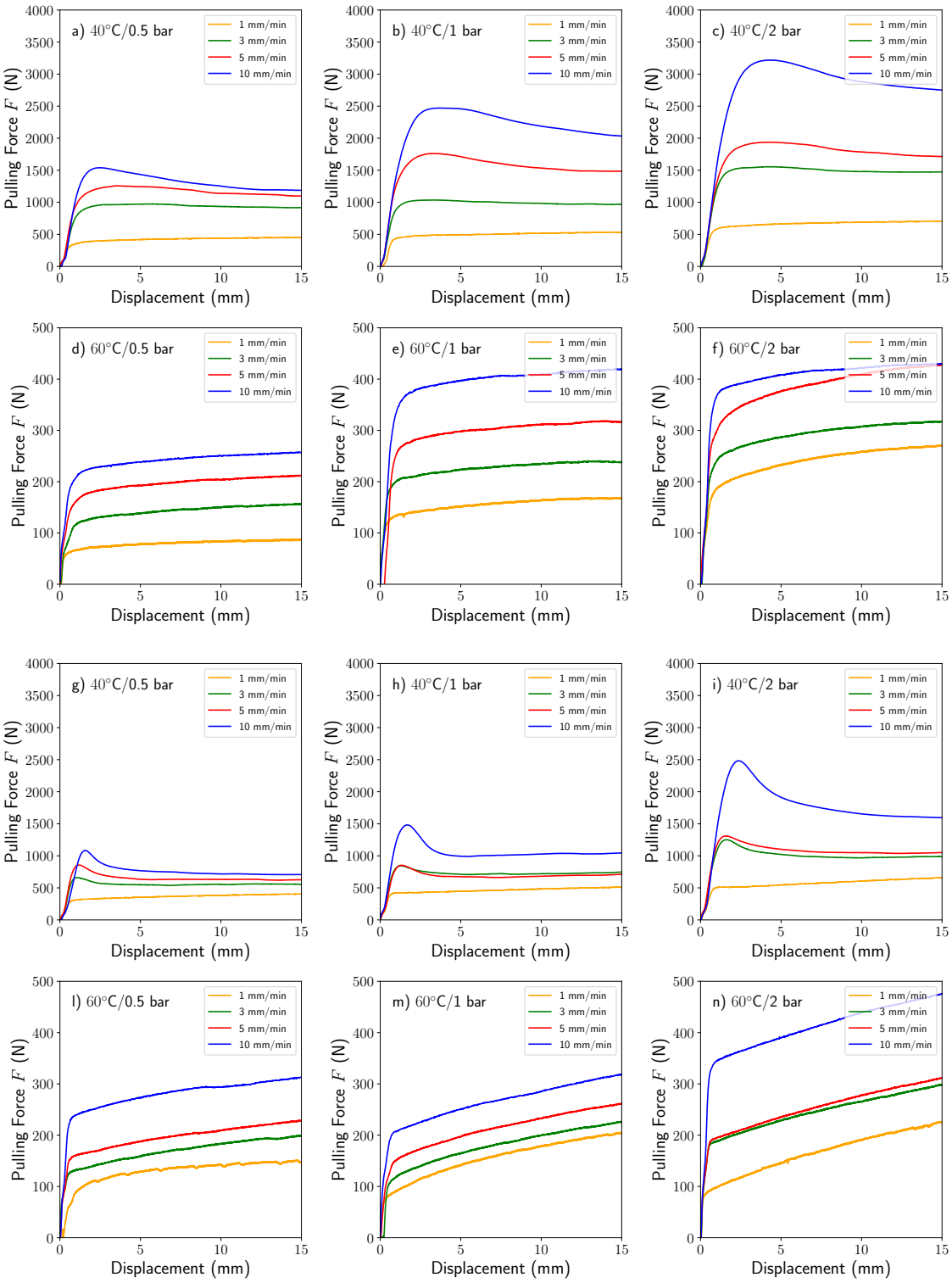

Figure 3.7: Pull-out load curves $F - U$ for prepreg-prepreg friction (**a**–**f**) and for prepreg-tool friction (**g**–**n**) tests carried out at 40 °C and 60 °C with pressure and sliding velocities ranging between 0.5–2 bars and 1–10 mm/min.

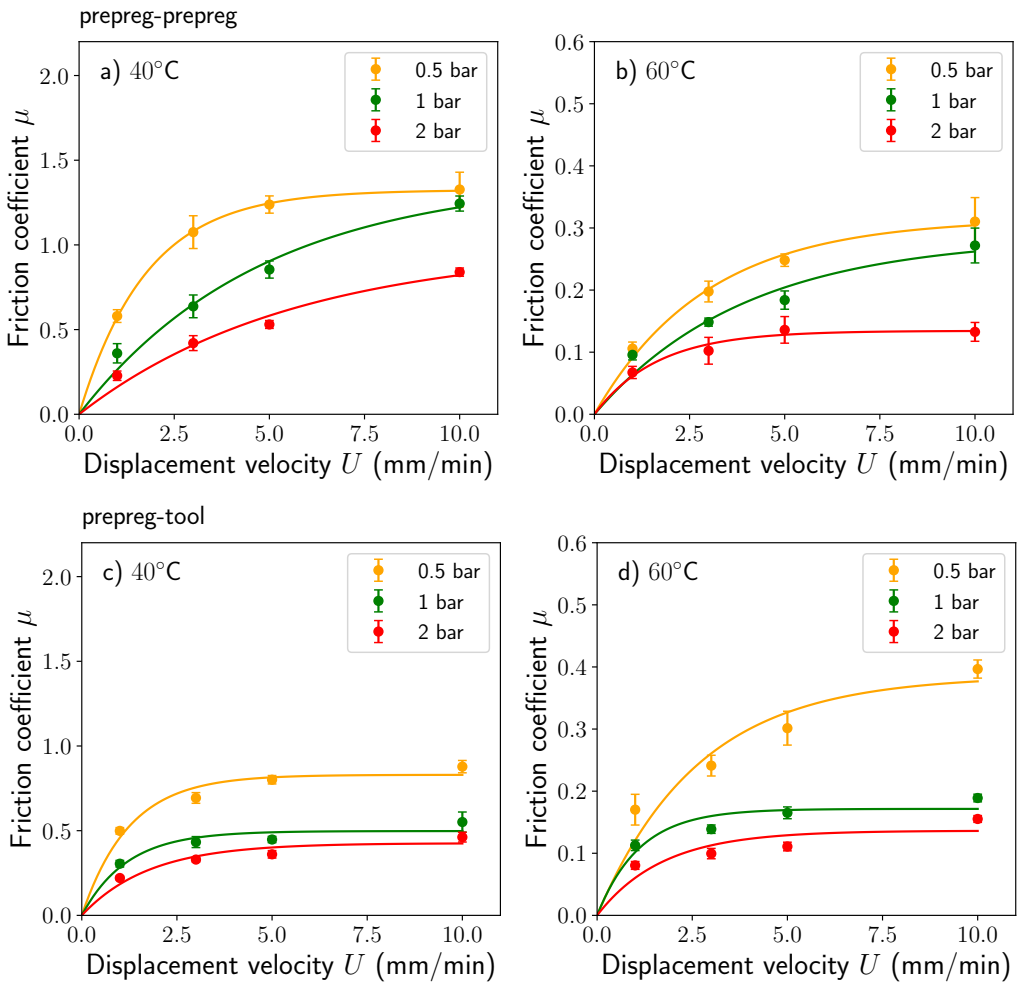

Figure 3.8: Average friction coefficient and standard deviation at 40 °C and 60 °C for prepreg-prepreg contact in (**a**,**b**) and prepreg-tool contact in (**c**,**d**).

When increasing the applied clamping pressure, the friction coefficient decreased considerably for both types of contacts (e.g., ≈1.75 for 0.5 bar and ≈1.00 for 2.0 bar for prepreg-prepreg contact) being this effect partially explained by the decrease of surface roughness with the increasing clamping pressure (Pasco et al., 2019). However, as shown in the force-displacement $F-U$ curves in Figure 3.7, the friction coefficient is, to an extent, sensitive to the pulling velocity. For velocities larger than 5 mm/min, the friction coefficient remains almost constant and only pressure produced a significant effect. Such behaviour is consistent with a lubricated regime where viscosity effects play a significant role. The resin film between plies is defined by the ratio of the theoretical film to the surface irregularity, as described by Shoaib and Espinosa-Marzal, 2020:

$$\lambda = \frac{h_{min}}{\sqrt{\sigma_1^2 + \sigma_2^2}} \tag{3.2}$$

Where σ_1 and σ_2 are the surface roughness amplitudes in the two main directions and h_{min} is the sliding layer thickness. If $\lambda > 3$, it will be possible to consider a lubrication regime in which the resin film completely separates the surface. In contrast, there is physical contact between surfaces when $\lambda < 3$. Profilometry, tomography, SEM, and optical microscopy were used to examinate the morphology and characterise the interlaminar resin layer's roughness, thickness, distribution, and homogeneity helping to develop an analytical model for the friction prediction between uncured prepreg layers.

Table 3.2: Average value and Standard deviation of friction coefficient for the ply-ply and ply-tool contact.

Clamping Pressure (bar)	**Pulling Velocity** (mm/min)	**Friction Coefficients at 40 °C Ply-Ply**	**Friction Coefficients at 40 °C Ply-Tool**	**Friction Coefficients at 60 °C Ply-Ply**	**Friction Coefficients at 60 °C Ply-Tool**
0.5	1	0.59 ± 0.03	0.47 ± 0.02	0.1 ± 0.004	0.17 ± 0.03
	3	1.08 ± 0.03	0.68 ± 0.02	0.19 ± 0.01	0.23 ± 0.02
	5	1.23 ± 0.03	0.78 ± 0.02	0.25 ± 0.005	0.28 ± 0.008
	10	1.31 ± 0.07	0.86 ± 0.04	0.3 ± 0.03	0.39 ± 0.01
1	1	0.33 ± 0.007	0.30 ± 0.02	0.09 ± 0.007	0.10 ± 0.008
	3	0.67 ± 0.04	0.42 ± 0.04	0.15 ± 0.001	0.13 ± 0.007
	5	0.85 ± 0.04	0.44 ± 0.02	0.19 ± 0.009	0.15 ± 0.008
	10	1.27 ± 0.03	0.55 ± 0.06	0.26 ± 0.02	0.18 ± 0.005
2	1	0.23 ± 0.03	0.21 ± 0.006	0.06 ± 0.003	0.07 ± 0.007
	3	0.41 ± 0.04	0.33 ± 0.01	0.09 ± 0.008	0.09 ± 0.007
	5	0.54 ± 0.01	0.35 ± 0.02	0.13 ± 0.01	0.19 ± 0.008
	10	0.85 ± 0.02	0.47 ± 0.02	0.14 ± 0.01	0.14 ± 0.005

3.2.1 Friction Interpretation and Interlayer Measurements

Upon evaluating the results of the pull-out test, it was realised that the most important aspect of friction characterisation is the interpretation of the mechanism being evaluated. In the case of prepreg composites, most researchers agreed that a thin layer of resin acts as a lubricating film between the two contact surfaces (Ten Thije et al., 2011; ten Thije et al., 2008). This assumption sets the stage for the use of tribological ideas such as the Lubrication Theory and the Reynold's equation. The Stribeck curve provides a simple visual representation of the friction experienced by two surfaces that are lubricated by a fluid. This representation enables the observation of the nonlinear response of this type of contact, which is expressed as a function of the contact load, the lubricant viscosity, and the lubricant entrainment speed. Contact between two rubbing surfaces is described as being between two opposing regimes. To begin, the boundary lubrication (BL) regime is defined as the contact between two surfaces in which the solid surface roughness contacts fully transmit the forces. Second, Elastohydrodynamic lubrication (EHL) sliding is defined as the regime in which a lubricant film separates the two contact surfaces, with friction regulated by the film thickness and rheological properties (Zhao et al., 2020). Between the two regimes, mixed lubrication (ML) implies that the fluid film penetrates inside the solid contacts, allowing for both forms of load transfer (Nikas, 2010).

The Stribeck hypothesis (Larberg and Åkermo, 2011), for our case study, presents the friction depending on a single variable termed Hersey number H, the following mathematical equation collects the effects of clamping pressure p, velocity $\dot{U}$, and temperature via the polymer viscosity $\eta(T, p, ...)$:

$$\mathrm{H} = \frac{\eta \dot{U}}{p} \tag{3.3}$$

The dynamic viscosity η is important during friction caused by film sliding. In the data sheet for the 8552 epoxy resin, Hexcel included measurements of its viscosity at different temperatures. The Arrhenius law was utilised once more to establish a correlation between the viscosity curve and the temperature values of significance, as defined in Section 2.3.1. The equation 2.2 represents the mathematical formulation, while the visual representation of the predictability of the fitting can be observed in Figure 2.16d. Figure 3.9 summarises the results of the friction coefficient dependence with the Hersey number obtained for all the frictional tests performed for the prepreg-prepreg and prepreg-tool contact. The minimum friction coefficient measured (0.06 ± 0.003 for prepreg-prepreg and 0.07 ± 0.007 for prepreg-tool contact, respectively) was obtained for tests carried out at the maximum temperature (minimum viscosity), the maximum pressure (2 bars) and the minimum sliding speed (1 mm/min). Similarly, the maximum coefficient recorded corresponded to minimum temperature tests with the lowest pressure and maximum displacement rate (1.31 ± 0.07 and 0.86 ± 0.04). In both cases (ply-ply and ply-tool), the Hersey number variation ranged two orders of magnitude $\Delta H \approx 5 \cdot 10^{-7} - 5 \cdot 10^{-5}$ m.

The surface roughness profile was acquired using the KLA Tencor D-500 profilometer. Five measurements were taken parallel to the fibre direction in various locations of the sample. The

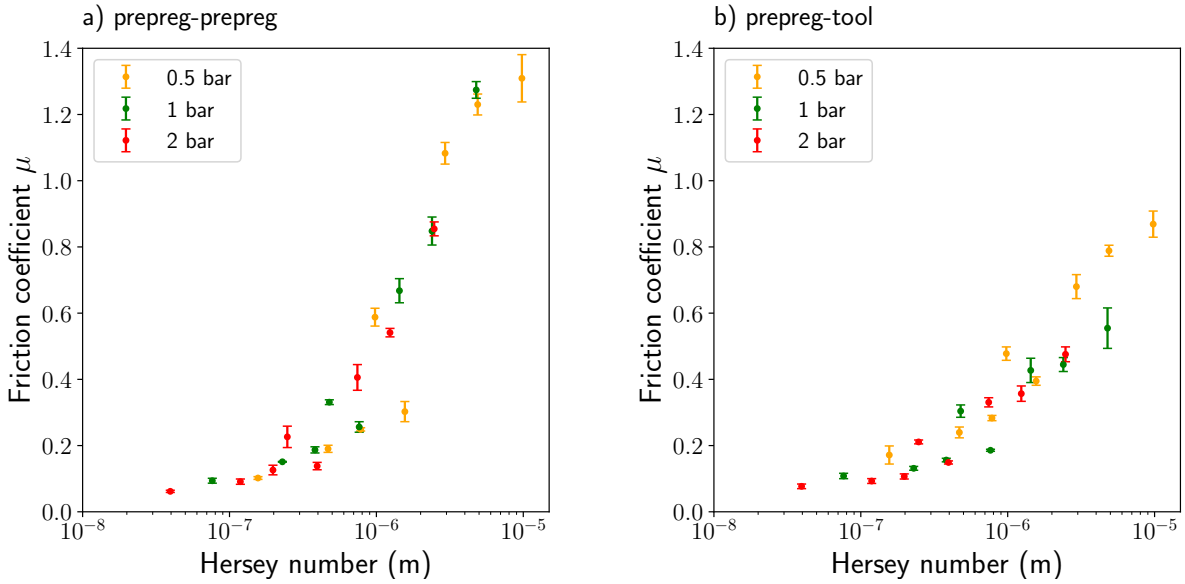

Figure 3.9: Stribeck curves for the friction coefficient: (a) Prepreg-prepreg contact, (b) Prepreg-tool contact.

Table 3.3: AS4/8552 Roughness Ra in μm for samples tested at 0.5 bar and pulled out at a displacement rate of 1 mm/min.

Contact Type	**40 °C**	**60 °C**
Prepreg-prepreg	3.22 ± 0.23	3.17 ± 0.66
Prepreg-tool	3.93 ± 0.46	3.10 ± 0.12

Ra roughness was calculated as the average of the profile height deviations from the surface geometry's mean line. Only specimens evaluated at 40°C and 60°C at 1 mm/min sliding speed and 0.5 bar clamping pressure were chosen for roughness measurements because they demonstrated better surface integrity. Table 3.3 displays the average value for all specimens studied, with the similarity of the results indicating the presence of a lubricating film smoothing the surface asperities and influencing the calculated roughness. These measurements assumed 3.5 μm roughness as a representative value for forward formulations.

It was anticipated that there would be a correlation between the conditions of the process and the thickness of the interlayer; however, when the Ra roughness was evaluated, there were no notable variations across contact types or testing settings. This indicates that even if the morphology of the thin layer changes, there is always a residual resin coating some parts of the surfaces, even after they have been frictioned. As a result of the observation of distinct patterns of resin dispersion, it was determined that the surface would also be analysed using optical micrographs (using an Olympus BX51) (See Figure 3.10). The research showed that some of the places had a high concentration of resin, while other areas seemed uncovered, leaving the fibres in their natural state. While looking at the areas where resin has accumulated, one can see with the naked eye that there is a pattern of resin waves running in

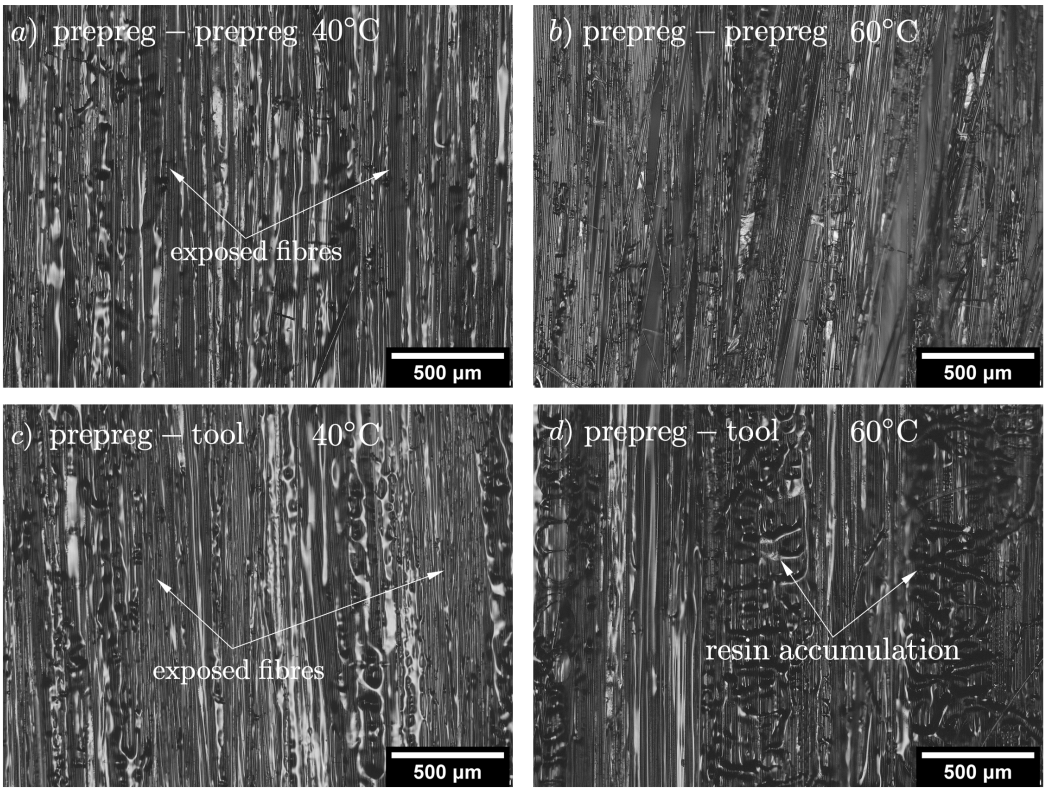

Figure 3.10: Optical micrographs of the contact surfaces after testing. In (**a**,**b**) is presented prepreg-prepreg contact surfaces for 40 °C and 60 °C; in (**c**,**d**) prepreg-tool contact surfaces respectively for 40 °C and 60 °C. Coupons were tested at 1 mm/min sliding speed.

the direction of the fibres on many of the surface areas, indicating that the distribution is unequal.

Furthermore, a deeper study was conducted through Scanning Electron Microscopy (SEM Apreo 2S LoVac) and X-ray computed tomography XCT. $[0°]_8$ prepreg laminates were prepared to resemble the state of the specimen at specific pressure and temperature combinations. Metallic plates, with an equivalent weight corresponding to a pressure of 0.5, 1, and 2 bars, were placed over the surface of the square rectangles. The coupons were introduced inside an environmental chamber at 40°C and 60°C for four entire days. This soft curing of the specimens was meant for freezing the material microstructure, including the lubrication film. Such conditions were only approximations of the actual situation of the prepreg contact surfaces during a real test. XCT images were acquired using a General Electric (former Phoenix) Nanotom 160 kV tomograph with a Hamamatsu 7942-25SK (2K×2K) detector and a nano focus X-ray tube with a molybdenum target. The target was installed during the scans, in nano focus mode 1, without adding any additional filter. The voltage and current of the X-ray tube for acquisition were set to 60 kV and 200 μA, respectively. Around 1800 radiographs were obtained for a complete 360° rotation in each tomographic inspection. The exposure time was set at 500 ms, taking nine images to make each radiography and lasting ≈2.5 h for each tomogram acquisition. Due to the relative position between the sample and

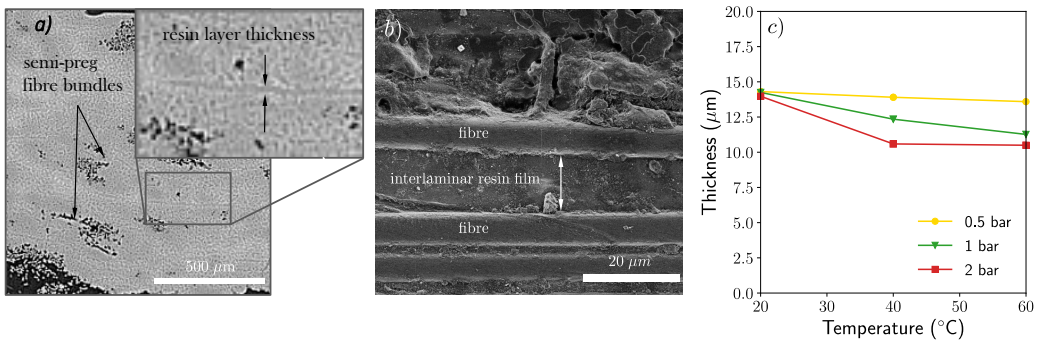

Figure 3.11: (**a**) XCT reconstruction of $[0°]_8$ laminates for the interlayer thickness determination, (**b**) SEM image with a detailed view of the space between two adjacent prepreg plies, (**c**) Average resin interlayer thickness as a function of the temperature and applied pressure.

the detector, a pixel size of 1.5 μm/pixel was achieved. The XCT scans were reconstructed using Phoenix datos|X 2.0 reconstruction v2.2.1 software by General Electric Sensing & Inspection Technologies and manipulated with ImageJ (Rueden et al., 2017). A cross-sectional view of the XCT reconstruction is presented in Figure 3.11a.

The film layer separation between two adjacent prepreg plies was clearly detected in the XCT images. The semi-preg fibre bundles within the different layers are observed as dark grey regions in the XCT and were indicative of the prepreg laminate's consolidation level when using the pressure-temperature cycle. The interlayer resin film can also be observed in the XCT reconstruction with a reasonably homogeneous thickness with an intricated geometry attributed to the fibre and fibre bundle rugosity. However, the resolution level obtained with the XCT was judged not enough for quantitative calculations, so SEM micrographs were used for this purpose. The interlayer thickness can be drastically reduced in poor resin regions with fibres close to each other. A representative cross-section acquired with the SEM is presented in Figure 3.11b. The thickness of the interlayer region was measured in a set of positions along the fibre direction, and the mean values and standard deviations are gathered in Figure 3.11c. The results showed an averaged interlaminar resin film of ≈12 μm. Regions with less or more resin accumulations were used in the measurement to enhance representativeness. The effect of the pressure on the interlaminar film thickness was negligible at room temperature. However, it was more evident as the temperature increased with the viscosity reduction, probably indicating light resin bleeding during testing operations.

3.3 Compaction test results

The compaction test was conducted without experiencing any difficulties, and it exhibited the characteristic resin bleeding commonly observed when doing this test on uncured plastic-reinforced composites. Three graphs can be obtained, each representing the temperature scenarios examined in our investigation. The load versus displacement response of the samples will be represented using varying shades of grey and line styles, which correspond to the evaluated stacking sequences. Additionally, yellow markers will be used to indicate the

conclusion of the relaxation phase and the initiation of a new displacement increment. By fitting these points, we can generate a red line that follows the curve of the fibre bed effect.

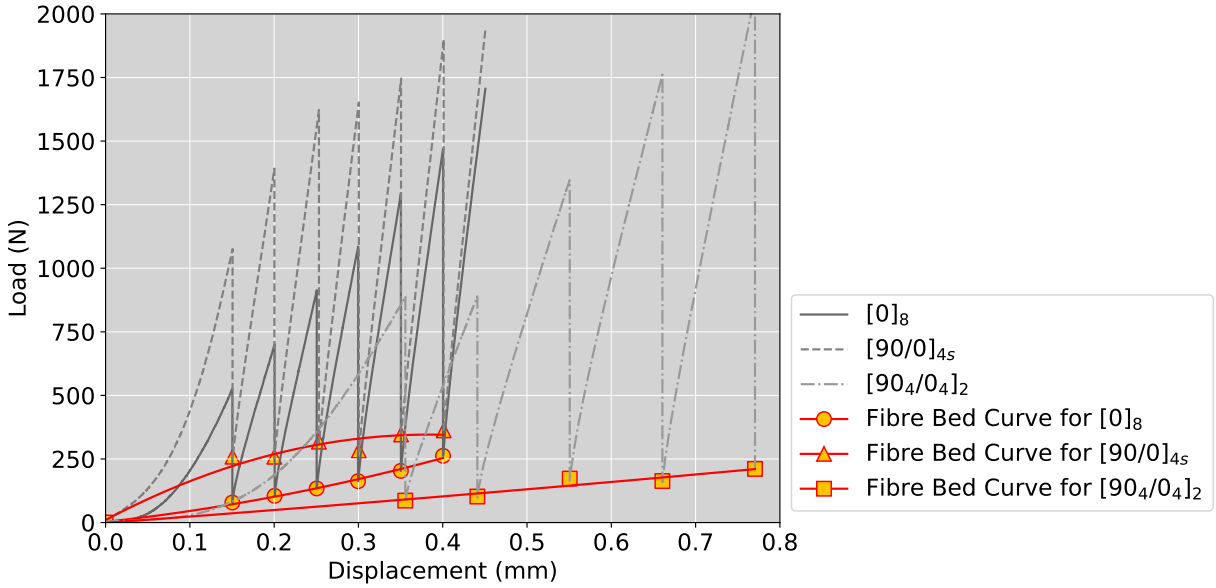

Figure 3.12: Comparison of load vs displacement response of AS4/8552 prepreg composite with different stacking sequences, assessed under compaction forces at room temperature A fitted red curve representing the fibre bed effect is shown in the plot.

As an initial remark regarding the scenario of room temperature, it is notable that the displacement cycle initially chosen for the sample with a $[90/0]_{4s}$ layup required modification due to the load response exceeding the measurement capacity of the load cell utilised in our testing fixture. The cycle was modified to align with the identical cycle for the $[0]_8$ layup scenario, resulting in no anomalies. In the instance of the $[90_4/0_4]_2$ layup, the displacement cycle was maintained as previously prescribed; however, the last increment was omitted due to the evident likelihood of surpassing the load cell's capacity.

The load response of the $[90/0]_{4s}$ sample is important to mention as it exhibited the largest fibre bed effect in terms of load among the three layup configurations investigated, across all temperature situations. The curve demonstrates a downward concave increase, leading to a steady load value of ≈300N. Eventually, it will align with the load-to-displacement values of the $[0]_8$ and $[90_4/0_4]_2$ layup samples, which exhibit an upward concave increase and a barely linear increase, respectively. The high load response seen in the $[90/0]_{4s}$ sample aligns with the phenomenon described in section 2.5, which states that the arrangement of fibres in a transverse orientation restricts the compaction of the laminate, leading to an increased load response. This phenomenon becomes even more evident when the percentage of thickness reduction is computed, revealing that this particular layup configuration demonstrates the lowest value among the other samples, measuring at 8%. In the scenario where a $[0]_8$ layup was employed, it was seen that the curve representing the fibre bed exhibited a notably higher magnitude compared to the curve obtained for the $[90_4/0_4]_2$ instance. This finding is relevant considering that the percentage of thickness reduction was greater in the former case,

with a value of 20%, as opposed to the 14% decrease observed in the latter condition. The observed outcome is noteworthy due to the fact that the $[0]_8$ layup exhibits greater capacity for compaction, corresponding to lower values of the fibre bed effect compared to the $[90_4/0_4]_2$ layup, which is anticipated to have internal interactions that offer challenges for compaction. This observation concludes that when a similar strain value is given to both $[0]_8$ and $[90_4/0_4]_2$ layups, the former is more likely to reduce its thickness compared to the latter. However, achieving this compaction in the former requires greater work. The compaction resistance may be reduced when many layers are stacked in the same fibre orientation. However, the presence of transversely positioned layers in the $[90_4/0_4]_2$ configuration restricts the resin bleeding process, leading to a lesser reduction in thickness. All of these percentages of thickness reduction and the equation for the fibre bed curves are presented in Table 3.4.

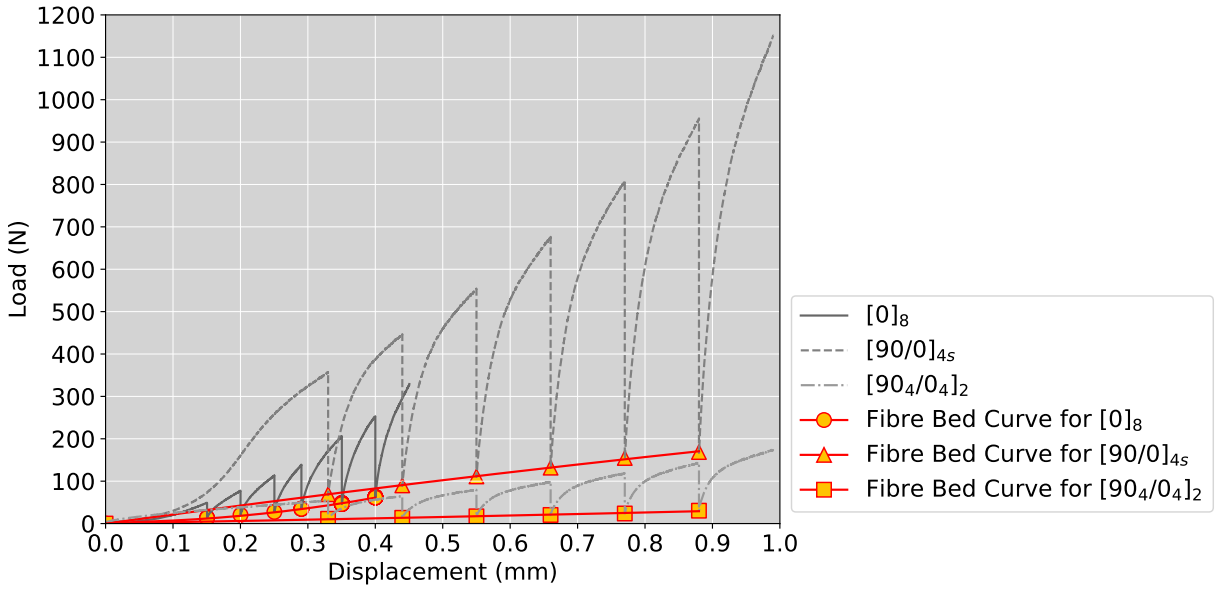

Figure 3.13: Comparison of load vs displacement response of AS4/8552 prepreg composite with different stacking sequences, assessed under compaction forces at 40°C. A fitted red curve representing the fibre bed effect is shown in the plot.

Upon raising the temperature to 40°C, a noticeable consequence is observed in the form of reduced load response across all tested samples, accompanied by a linear likelihood shape of the fibre bed curves. These observations may be attributed to the lack of viscoelastic behaviour exhibited by the resin when exposed to heat, as evidenced by the consistent findings across all mechanical tests conducted within this thesis. Another consequence of raising the temperature is the increased capacity of the resin to undergo flow or, in this particular instance, to be extruded. The previous effect can be observed by examining the percentage of thickness reduction presented in Table 3.4. It is evident that for the $[90/0]_{4s}$ layup, the value is three times greater than the percentage of the RT case, while for the $[90_4/0_4]_2$ case, it is twice as large. Although the total strain amount for the case of $[90/0]_{4s}$ is not equivalent, it is anticipated that the percentage of thickness reduction will double with an increase in temperature. For the case of $[0]_8$ layup, it has been shown that the percentage of thickness

reduction is equivalent to that of the RT condition. This finding supports the notion that the stacking sequence in question exhibits a low resistance to compaction, regardless of the resin's condition. After observing the fibre bed curves, it is evident that the curve corresponding to the $[90/0]_{4s}$ layup exhibits the highest load response, however not significantly differing from the fibre bed curve values exhibited by the $[0]_8$ layup. Despite the plies' transverse orientation, the $[90_4/0_4]_2$ layup shows extremely low load values on the fibre bed curve, indicating that it is very likely to be compacted, which results in a substantial amount of resin being pressed out.

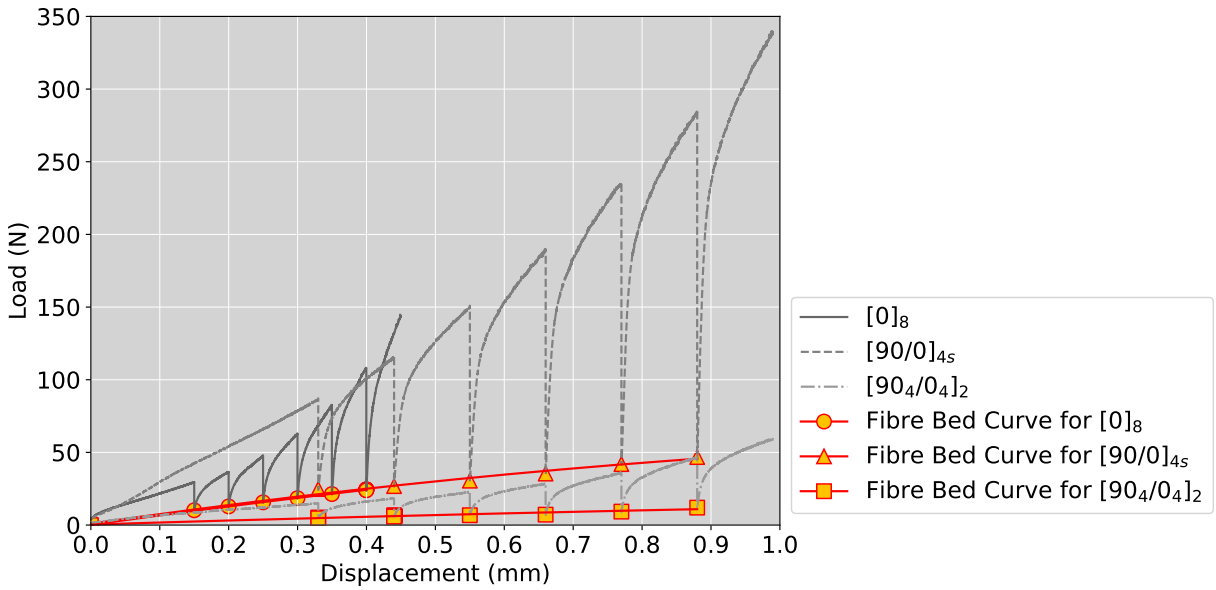

Figure 3.14: Comparison of load vs displacement response of AS4/8552 prepreg composite with different stacking sequences, assessed under compaction forces at 60°C. A fitted red curve representing the fibre bed effect is shown in the plot.

Notably, when a temperature of 60°C was considered, the fibre bed values of the $[90/0]_{4s}$ layup exhibited a similarity to those of the $[0]_8$ configuration. A consistent decrease in load is found across the three stacking sequences, as well as a linear trend exhibited by the fitted fibre bed curves. The observed curves do not yield unexpected results considering the previously assessed scenarios. However, the analysis of the percentage of thickness reduction does present noteworthy findings. The analysis of the percentage values reveals a notable similarity in the values of $[0]_8$ and $[90/0]_{4s}$ layups. This similarity may suggest that raising the temperature could mitigate any obstacle arising from the plies configuration during the compaction of the laminate. Another observation can be made by comparing the percentage values of thickness reduction obtained for the stacking sequences $[90/0]_{4s}$ and $[90_4/0_4]_2$ at temperatures of 40°C and 60°C. The similarity of these values suggests that within this temperature range, there may not be a significant difference in the amount of compaction accepted by the two stacking sequences. However, it is important to note the disparity in the load levels of the fibre bed curves.

Table 3.4: Thickness reduction and fibre bed equation for different laminates and temperatures.

	RT °C	40 °C	60 °C
Layup $[0]_8$			
Thickness Reduction	20%	20%	26%
Fibre Bed Equation	$667.2x^2 + 360x + 2.8$	$342.8x^2 + 8.3x + 2.9$	$-15.9x^2 + 66.7x + 0.1$
Layup $[90/0]_{2s}$			
Thickness Reduction	8%	25%	26%
Fibre Bed Equation	$120x^2 + 906.8x + 4.5$	$-28.8x^2 + 219.4x + 0.2$	$-19.5x^2 + 68x + 0.94$
Layup $[90_4/0_4]_2$			
Thickness Reduction	14%	34%	34%
Fibre Bed Equation	$38x^2 + 245.4x + 1.4$	$6.4x^2 + 27x + 0.4$	$-2.9x^2 + 14.5x + 0.3$

3.4 2-point bending test analysis

Given the focus of this thesis on characterising uncured pre-impregnated composite materials, driven by the aerospace part manufacturing process known as thermoforming, the experiments conducted with the 2-point bending test device were primarily aimed at the analysis of wrinkle formation. This emphasis was due to the fact that wrinkle formation stands out as the most prominent defect in the thermoforming process. Although our system has the capacity to do flexural testing for the purpose of extracting the mechanical properties of the material, we did not carry out such tests. The decision was based on two main reasons: Initially, our core focus was directed at comprehending and examining the mechanisms underlying wrinkle formation. Furthermore, a significant investment of time and resources was dedicated to the creation and optimisation of the device, subsequently constraining the opportunity to conduct more extensive mechanical tests.

In this section, we will explore the analysis of wrinkle formation. The data needed for this exploration are the angle versus time readings captured by the sensor, complemented by the camera's video footage showing the longitudinal side view of the sample as it bends. The load torsion vs. time plot depicted in Figure 3.15 can be derived from the first acquisition, as each increase in angle corresponds to a specific rise in load torsion resulting from the augmentation of weight in the pulley system. The video recording will be utilised for the purpose of identifying the formation of wrinkles and detecting the precise moment at which they initiated.

The initial observation derived from the plot is focused on the blue dashed line, which represents the rise in load torsion. It is evident that the loading time varies across multiple loading steps, since the bending of the sample at each interval may be influenced in distinct ways. The initial loading phase is brief as it does not generate a significant deformation of the sample and achieves stabilisation quickly. In contrast, the remaining processes require longer time to stabilise due to the existence of defects. The continuous red line in the same plot represents the variations in the curvature ratio exhibited by the sample during the bending process. Each curvature ratio value provided corresponds to a picture acquired from the video record, where equations 2.8 and 2.9 are performed to derive the respective value. The initial value is set to zero as the sample starts off with a flat shape. After the first loading, the curvature exhibits a ratio of approximately 450 mm, which will gradually decrease as the load torsion increases. Three curvature measurements are taken for each increment in torsion load, corresponding to three key points in the process: the initial stage, a midpoint, and the point at which the curvature stabilises. When further points are taken into account, the form represented by this line throughout each weight increment will exhibit a decreasing concave upward curve, with a flat segment towards the end indicating a stable state of the sample.

Once the registers from the acquisition devices have been comprehended and the plots have been prepared, the video footage can be utilised to conduct observations regarding to the development of defects. Figure 3.16 provides a brief description of the process involved in detecting the progression of wrinkles, emphasising three notable occurrences: the onset of wrinkles, the formation of multiple wrinkles, and the nucleation of wrinkles. It is possible to determine the time of each of these events, which will be translated to Figure 3.15 to match

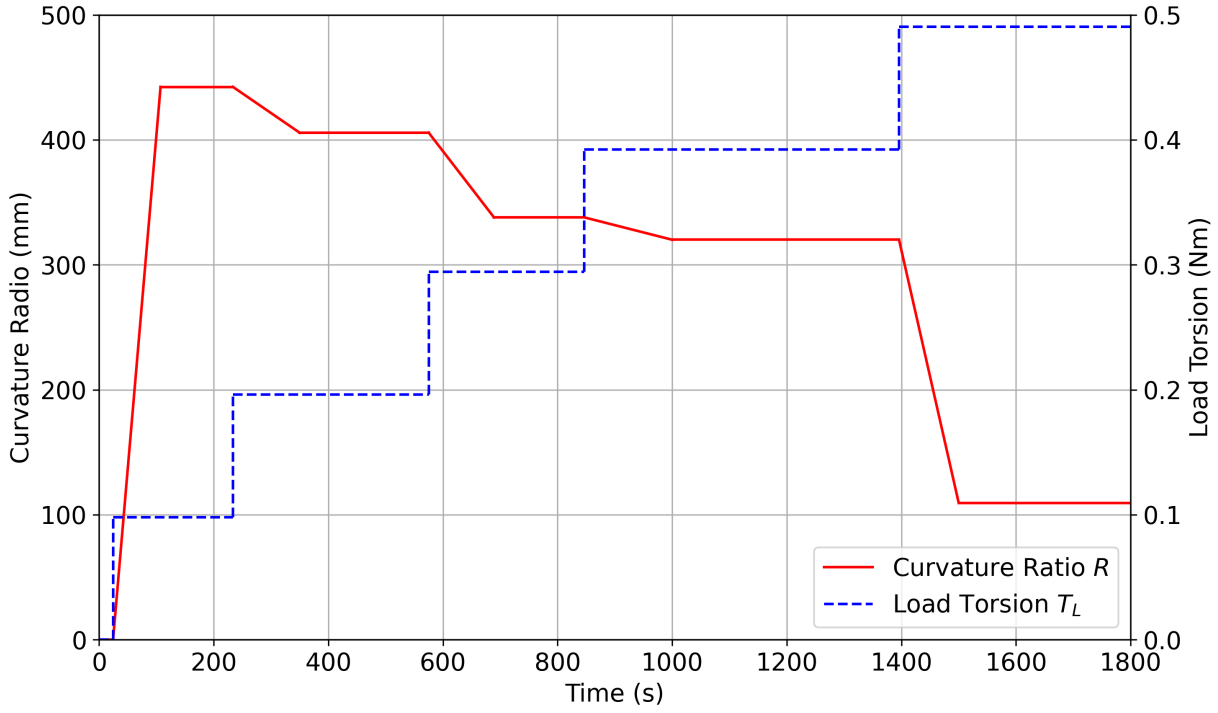

Figure 3.15: The loading cycle of a 2-points bending test and the reduction of the curvature ratio as the sample is being bent. The test corresponds to an 8-layer uncured prepreg laminate being tested at room temperature."

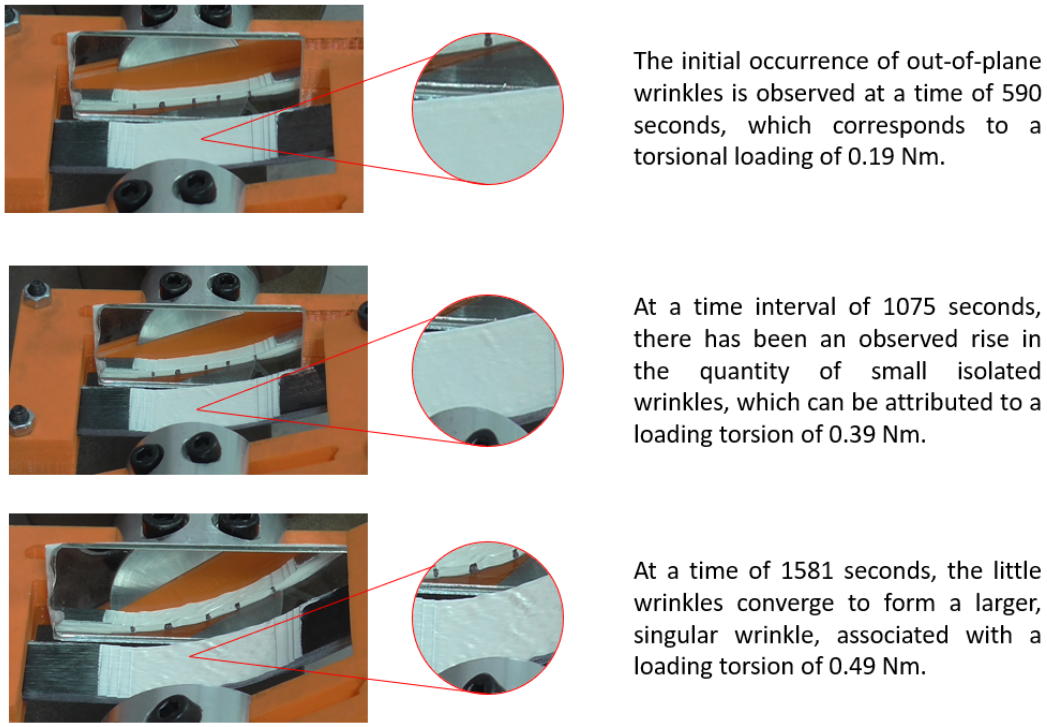

Figure 3.16: Sequencing the formation of wrinkling in an uncured prepreg laminate under bending loading. Time and loading identification for each occurrence.

the precise load torsion that the sample was able to withstand and the sample's curvature ratio at the instant that the wrinkle event occurred. In the initial register, a time of 490 seconds was captured, which corresponds to a torsional load of 0.19 Nm and a curvature ratio of 410 mm. The values shown in this instance pertain to the second loading phase executed during the experiment, wherein a noticeable increase in loading time is observed in comparison to the preceding step. This observation is logical as each occurrence of a defect is a result of the release of stress concentration, which then redistributes the stress to other regions of the sample. This redistribution leads to increased bending of the sample, hence requiring a longer period of stabilisation. In the third loading phase, an absence of new defects was observed, resulting in a rapid stabilisation of the sample. The observation of many wrinkles began at an exact time of 1075 seconds, which corresponded to a torsion load of 0.39 Nm. At this stage, the curvature radius is observed to correspond to 320 mm, gradually diminishing as additional minor wrinkles emerge until reaching a state of stability at 1400 seconds. The ultimate increase in torsional loading will lead to minor wrinkle nucleation at a time of 1581 seconds, eventually transforming into an individual large wrinkle. This increment will cause the torsion load to reach a value of 0.49 Nm, subsequently causing the sample to collapse and thereby concluding the experimental test.

The current scenario highlights just one of the many outcomes this device can offer in its early developmental phase. The analysis of wrinkles suggests the potential addition of a three-dimensional correlation system in future versions. This enhancement would allow measuring the wrinkle's out-of-plane dimensions, map strain distributions, and highlight potential stress

concentrations. Furthermore, exploring the effects of different laminate stacking sequences on torsion resistance becomes another important area of study. Additionally, if torsion is transferred through a mechanical transmission shaft, the ability to control torsion speed is introduced. This change brings in an extra test variable, expanding the scope for diverse examinations. In conclusion, the vast potential improvements to this device highlight its importance as a key tool for investigating the challenges of large bending deformations across various materials.

3.5 ±30° and ±60° Off-axis Test: Results and Comparison

The assessment of the fundamental characterisation of AS4/8552 uncured prepreg composite involved experiencing various unexpected events, such as the interlaminar slippage observed under tensile stress, together with expected events like the viscoelastic behaviour. While tensile loading samples aligned at 0°, 90°, and ±45° were used to successfully characterise the material, there may be a wide range of affects at other fibre orientations. The effects under consideration comprise various factors, such as the viscoelastic response of the material when deviating from the 0° fibre direction, the presence of defects during loading, the influence of temperature on the sample, and the distribution of strain. The presence of these uncertainties served as a motivation for exploring alternative fibre directions in order to establish a connection between the currently considered fibre directions. This analysis was also intended to expand our comprehension of the fibre direction influence on the stress-strain response, with the intention of implementing the findings into future computational modelling efforts based on this study. This section will provide a detailed analysis of the stress-strain response of the additional samples assessed at off-axis angles of ±30° and ±60°. The dimensions of the samples under consideration are consistent with those employed for the $[\pm 45]_{2s}$ samples, in accordance with the detailed procedure outlined in section 2.3.2. The number of samples, displacement rates, and temperature values were all the same as those used in the earlier tensile tests.

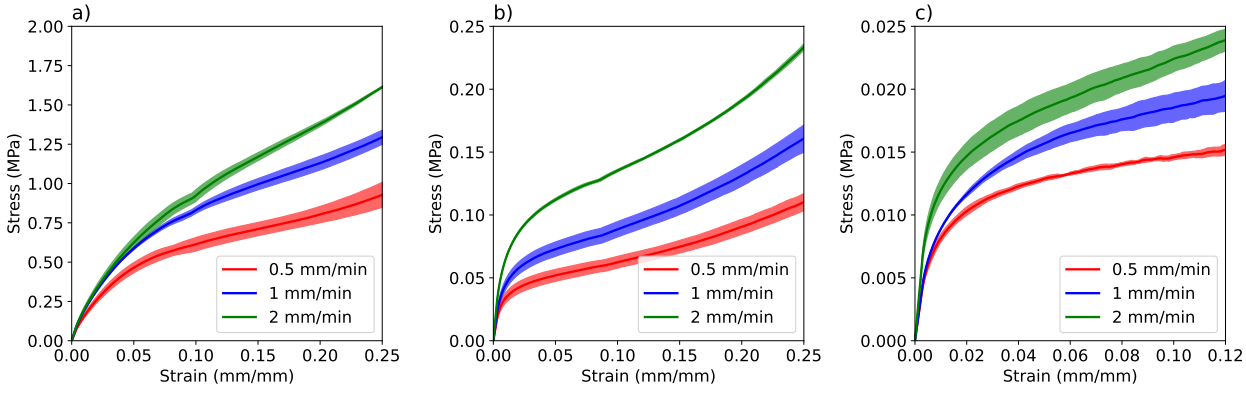

Figure 3.17: $[\pm 30]_{2s}$ Shear Tensile Test employing a universal testing machine at three different strain rates. a) Test conducted at RT, b) Test conducted at a temperature of 40°C and c) Test conducted at a temperature of 60°C.

During loading, rotations of the fibres have been observed for the $[\pm 30]_{2s}$ samples, which is translated in the stress-strain curve as a growing stress response that never stabilised at all of the strain ratios tested. The rotation of the fibre is reduced but still present in the case of 60°C. The stress values attained by these samples are intermediate between those obtained by the $[0]_8$ and $[\pm 45]_{2s}$ samples, but with a clear proximity to the values of $[\pm 45]_{2s}$, which is consistent with the fact that fibres within an uncured prepreg laminate have a minimal effect on the stress resistance unless they are aligned with the loading direction. The viscoelastic effect exhibits an evident manifestation across all scenarios, displaying a precise reaction to increments in strain rate. The repetitiveness of the test across all conditions was high, accompanied by a minimal occurrence of damage inside the sample and significant strain values achieved, even in instances conducted at a temperature of 60°C. The majority of the reported data could be expected based on prior tests. However, an intriguing finding in this study is the stress response exhibited by the samples evaluated at 60°C, since their values closely resemble those of the samples tested at $[\pm 45]_{2s}$ for the same temperature. As previously stated, the application of this specific temperature condition causes the resin to undergo a transition into a gel state. In this state, the presence of fibres has a reduced impact on the stress response. This phenomenon may account for the observed similarity in stress response across samples subjected to tensile loading at 60°C, with fibre directions of ±45° and ±30°.

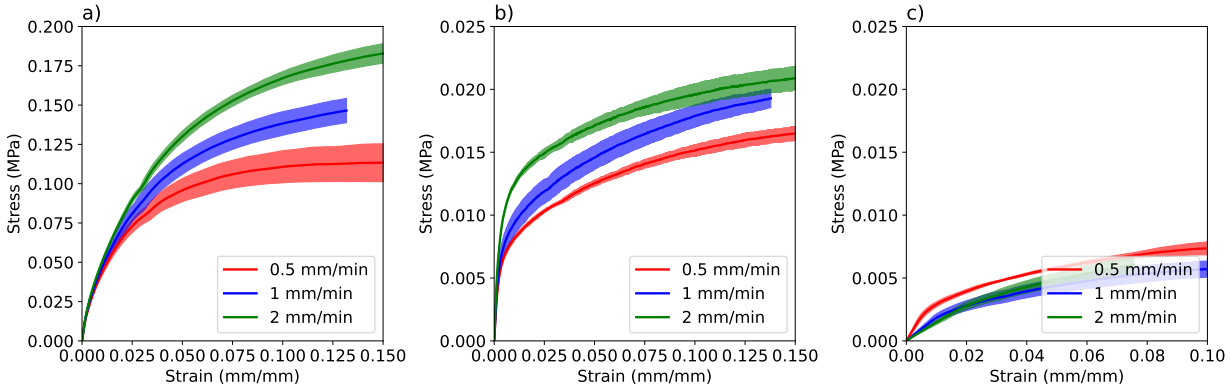

Figure 3.18: $[\pm 60]_{2s}$ Shear Tensile Test employing a universal testing machine at three different strain rates. a) Test conducted at RT, b) Test conducted at a temperature of 40°C and c) Test conducted at a temperature of 60°C.

In the case involving samples having fibres oriented at a 60° angle, it is evident that the stress-strain curves exhibit reduced prominence in comparison to the preceding example. Notably, certain curves even attain a state of equilibrium, characterised by a constant stress value. Negligible fibre rotation was detected during the loading process; however, a significant presence of damage was noted, which had an impact on the maximum strain achieved. It is evident that the maximum strain values in this case are lower compared to those observed in the prior scenario. One unexpected result pertains to the stress levels seen. It was initially anticipated that the stress values would fall between those found for the $[\pm 45]_{2s}$ and $[90]_8$ samples. However, the acquired values were either lower or very close to those observed for the $[90]_8$ samples. It can be inferred that at a particular angle of fibre direction,

the fibres exhibit insufficient strength to bear any minimal load, leading to similar stress measurements irrespective of the fibre angle (See Figure 3.19). A distinct viscoelastic effect is noticed, exhibiting a precise response to incremental strain rates, except in the case of samples subjected to a temperature of 60°C. In this instance, the viscoelastic effect is found to be diminished, with no obvious difference in response to changes in the strain rate.

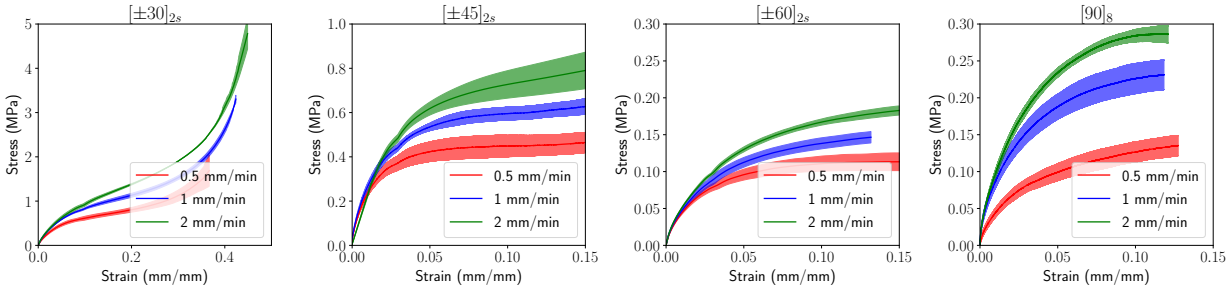

Figure 3.19: A comparison of stress levels and viscoelastic response was conducted on samples with four different fibre directions at room temperature.

Chapter 4

Modelling the mechanical behaviour of uncured composite materials

4.1 Advancements in Mathematical Modeling of Uncured Prepreg Composites

After finishing our experimental campaign and comprehensively analysing the data, we have acquired a detailed comprehension of the characteristics of uncured pre-impregnated composite materials. These materials demonstrate a poor stress reaction in the transverse and shear directions, in contrast to their rigid response in the longitudinal direction. These particular characteristics and the orthotropic properties of a composite laminate present considerable challenges in manufacturing structural components. The inherent adaptability of stacking prepreg laminates in layers, and its easy manipulation provide many design options, but it also brings about possible imperfections. Every distinct arrangement has the potential to cause flaws in the end product. These flaws can significantly affect the overall efficiency and longevity of the composite material. Several studies have aimed to investigate the origins of these flaws. Some attribute them to variances in material composition or production discrepancies, while others attribute them to damages caused by overloads or mismanagement during use (Cantwell and Morton, 1992). Thermoforming manufacturing technology is often linked to specific flaws, such as the formation of wrinkles, uneven distribution of resin, and folding of plies. The occurrence of these flaws has been linked to issues such as incompatible stacking sequences (Hallander et al., 2016), interlaminar shear stress (Larberg and Åkermo, 2011), compaction and flow behaviour (Naresh et al., 2022), and varying process conditions (Netzel et al., 2021). All of these factors can have a negative impact on the quality of the final product. Due to the many variables involved in the process and even slight alterations in part shape may require different combinations, depending entirely on a trial-and-error approach, it becomes impractical. This strategy is not only financially expensive but also consumes significant time.

The use of mathematical modelling has been used to support the construction of innovative and intricately shaped structural components. Prior research has presented many approaches

to prepreg modelling. Rogers, 1989b formulated a mathematical theory to describe the phenomenon of squeeze flow in composites. In contrast, Skartsis et al., 1992 constructed a model to simulate resin flow through a fibrous medium. ÓBrádaigh et al., 1993 conducted one of the initial studies on the development of wrinkles, which focused on sheet-forming mechanisms. Hubert and Poursartip, 2001b; Hubert and Poursartip, 1998a; Hubert et al., 1999 introduced an Abaqus model that describes the behaviour of a fibre bed made of prepreg material. The model incorporates the evolution of permeability based on changes in fibre volume. Bonet and Burton, 1998; Spencer, 2000 introduced the constitutive equation for viscous fluids that have been strengthened. Haanappel, 2013 examines the intraply behaviour of prepreg using experimental models, as well as Guzman-Maldonado et al., 2016. J. P. Belnoue et al., 2016, 2018b present a physics-based compaction model for simulating wrinkles across the thickness, proposing a framework for modelling prepregs, along with a series of experiments, in order to accurately represent the behaviour and underlying mechanisms of the prepreg material.

Our current investigation proposes an uncured prepreg model incorporating all mechanical aspects using a generalised Maxwell model. The topics of interest are intraply shear, compaction fibre bed behaviour, squeeze flow, and fibre tension. To accurately model the behaviour of uncured prepreg, it is essential to have a thorough understanding of all the mechanisms that occur during the forming process. Beginning with the constituents of the material, which includes two primary elements for our desired application: carbon fibre and epoxy resin. Even at elevated temperatures, carbon fibre has solid-like characteristics, while epoxy resin displays fluid-like behaviour and viscoelastic properties. Given the focus of this research on predicting the thermoforming process of unidirectional composite prepregs, it is crucial to incorporate models for both elastic and fluid mechanisms.

Composite processing involves the participation of two occurrences:

1. Elastic behaviour of the fibre network.
2. Viscous flow of resin within a porous medium.

The initial occurrence is documented in J. P. Belnoue et al., 2016; Cai and Gutowski, 1992; T. G. Gutowski, Cai, et al., 1987; T. G. Gutowski, Morigaki, and Cai, 1987; E. L. Wang and Gutowski, 1991, indicating that the behaviour of fibre beds is attributed to the inability to align all the threads in unidirectional composites properly. This leads to a slight waviness and the formation of a network of entwined fibres, known as the fibre bed effect. As a result, there are a few points of contact between fibres at the start of the deformation, and the compaction force is minimal, resulting primarily from squeezing flow. As the number of fibres in contact grows, load compression also rises, resulting in a non-linear increase in compaction force. Another process involving fibres is the tension fibre, where all the contribution comes from the fibres. A mechanism primarily impacts the Poisson components due to the waviness of the fibres, leading to a tendency to a zero Poisson ratio when the fibre bed is under tension.

For the second event, T. G. Gutowski, Cai, et al., 1987; Kelly, 2011; W. I. Lee and Springer, 1987; Rogers, 1989a; Shuler and Advani, 1996 state that many processes are involved, and it depends on whether the resin is thermoset or thermoplastic. T. G. Gutowski, Morigaki, and Cai, 1987 utilised the Darcy equation to describe the compaction flow while also including

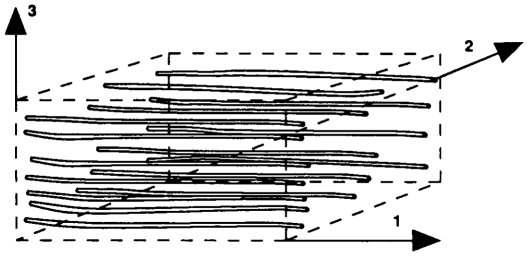

Figure 4.1: A fibre bundle displaying slight waviness

bleeding in the transverse direction. However, in the models proposed by the authors Engmann et al., 2005; Rogers, 1989b; Shuler and Advani, 1996; E. L. Wang and Gutowski, 1991, prepreg compaction is represented as a squeezing flow, with the assumption that no bleeding effects are occurring across the fibres. The squeeze flow approximation is mainly employed for thermoplastic materials because of their significantly higher viscosity compared to thermoset materials (E. L. Wang and Gutowski, 1991). In this approximation, both the resin and fibres deform similarly. Ultimately, two mechanisms may occur during formation from the matrix perspective: matrix leakage through fibre bed arrangement and simultaneous compression of both fibre and matrix. Both of these mechanisms can coincide, whether thermoset or thermoplastic, depending on the matrix type. One method to determine if squeeze flow occurs in thermoset prepreg is to use tomography to assess the distribution of fibres and quantify any distortion, network formation, or twisting of the fibres before and after compaction. If there is a significant rise in distortion, it can be attributed to squeeze flow rather than bleeding, as the latter does not impact fibre distribution (Barnes and Cogswell, 1989). Figure 4.2 illustrates many mechanisms (Hubert and Poursartip, 1998b; ÓBrádaigh et al., 1993), including percolation or Darcy flow, transverse and longitudinal shear, which can be represented as transverse squeezing flow or flow between longitudinal fibres, and anisotropic friction between plies at the inter-ply level. An essential challenge in modelling composite forming is to differentiate between the occurring mechanisms and provide a physical interpretation of the model inputs.

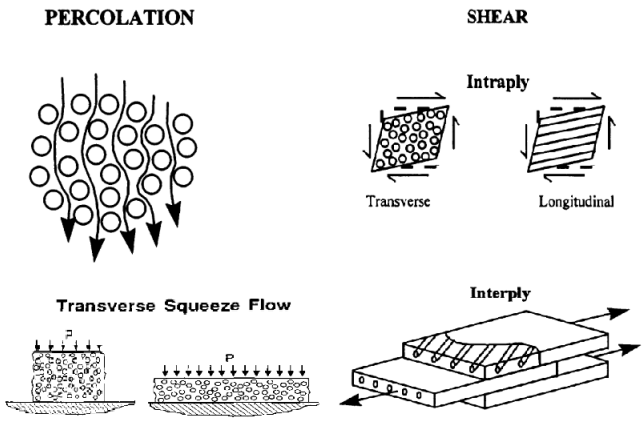

Figure 4.2: Recognition of the mechanics of resin flow during the forming process

The flow in the longitudinal fibre direction can only be simulated using Darcy's law, as the fibres in this direction are almost inextensible compared to the matrix. Interpreting flow under shear in the plane and out-of-plane is challenging because both the fibre and matrix contribute significantly to the shear behaviour. The fibres slide between each other due to the presence of a fluid (matrix), and additionally, the fibres resist movement by kinking when subjected to compression during shear loading. The behaviour of compaction prepreg can be represented as either squeeze flow or Darcy flow, incorporating the behaviour of the fibre bed. Accurately simulating a phenomenon in real-time is exceedingly challenging without empirical evidence supporting the model. At the onset of compaction, it is plausible to assume that the behaviour is primarily characterised by a squeeze flow, wherein the fibre and matrix move in unison. The initiation of the fibre bed results in the constriction of lateral motion and the flow of the matrix material via the fibres, leading to the occurrence of bleeding phenomena. This phenomenon is mathematically represented using Darcy equations.

4.2 Formulation for an anisotropic fibre-reinforced viscoelastic material model

This section describes the model for a fibre-reinforced anisotropic and viscoelastic material. The constitutive model has been implemented into Abaqus Explicit as a VUMAT user function. This subroutine utilises the Green-Nadghi stress rate as follows:

$$\boldsymbol{\sigma}^{\nabla G} = \dot{\boldsymbol{\sigma}} - \boldsymbol{\sigma} \cdot \boldsymbol{\Omega}_G - \boldsymbol{\Omega}_G \cdot \boldsymbol{\sigma} \tag{4.1}$$

Where $\dot{\boldsymbol{\sigma}}$ is the stress time derivative and $\boldsymbol{\Omega}_G = \dot{\boldsymbol{R}}\boldsymbol{R}^T$ with $\boldsymbol{R}$ as rotation tensor resulting from the polar decomposition of the deformation gradient tensor into the rotation and stretch $\boldsymbol{F} = \boldsymbol{R}\boldsymbol{U}$. Time integration between t^n and t^{n+1} assuming Δt small results in the stress increment using the mid-point rule.

$$\boldsymbol{\sigma}^{n+1}_{\{\vec{e}_i^{n+1} \otimes \vec{e}_j^{n+1}\}} = \boldsymbol{\sigma}^{n}_{\{\vec{e}_i^{n} \otimes \vec{e}_j^{n}\}} + \Delta\boldsymbol{\sigma}^{n+1/2}_{\{\vec{e}_i^{n+1/2} \otimes \vec{e}_j^{n+1/2}\}} \tag{4.2}$$

VUMAT time integration is carried out in the Green-Nadghi co-rotational frame defined as $\vec{e}_i = \boldsymbol{R}\vec{e}_{i0}$. In fibre-reinforced materials, the Green-Nadghi frame will not coincide with the material frame formed with the rotated fibre direction. Therefore, any stress increment computed at the constitutive level should be translated into the Green-Nadghi frame for consistent time integration.

We will assume the initial undeformed fibre direction as $\vec{f}_{10}$, the perpendicular-to-the-fibre direction contained the composite ply as $\vec{f}_{20}$, and $\vec{f}_{30}$ the corresponding orthogonal direction out-of-plane as $\vec{f}_{30} = \vec{f}_{10} \times \vec{f}_{20}$. These set of vectors forms the undeformed fibre frame $\{\vec{f}_{10}, \vec{f}_{20}, \vec{f}_{30}\}$. The unit vectors forming the orthogonal reference base in the undeformed state are $\{\vec{e}_{10}, \vec{e}_{20}, \vec{e}_{30} = \vec{e}_{10} \times \vec{e}_{20}\}$, respectively. Let us assume the deformation gradient and stretching tensors for time t^{n+1} are given by $\boldsymbol{F}^{n+1}$ and $\boldsymbol{U}^{n+1}$, respectively. Then, the corresponding rotation tensor is obtained by inverting $\boldsymbol{F}^{n+1} = \boldsymbol{R}^{n+1}\boldsymbol{U}^{n+1}$. The vector frame

formed by the rotating fibre direction $\vec{f_1}$ at t^{n+1} can be determined as follows. Firstly, the normalised fibre direction is computed as:

$$\vec{f_1}^{n+1} = \frac{\boldsymbol{F}^{n+1}\vec{f}_{10}}{\|\boldsymbol{F}^{n+1}\vec{f}_{10}\|} \tag{4.3}$$

Secondly, the second-order tensors $\boldsymbol{p}$ and $\boldsymbol{q}$ projecting any arbitrary vector along the deformed fibre direction $\vec{f_1}^{n+1}$ and perpendicular-to-the-fibre direction are constructed.

$$\boldsymbol{p} = \vec{f_1}^{n+1} \otimes \vec{f_1}^{n+1} \text{ and } \boldsymbol{q} = \mathbf{1} - \boldsymbol{p} \tag{4.4}$$

Lastly, the orthogonal direction of the fibre and the complete vector base is formed.

$$\vec{f_2}^{n+1} = \frac{\boldsymbol{q}(\boldsymbol{F}^{n+1}\vec{f}_{20})}{\|\boldsymbol{q}(\boldsymbol{F}^{n+1}\vec{f}_{20})\|} \text{ and } \vec{f_3} = \vec{f_1} \times \vec{f_2} \tag{4.5}$$

The fibre-deformed frame $\{\vec{f_1}, \vec{f_2}, \vec{f_3}\}$ is the one used to evaluate the constitutive behaviour of the material. The VUMAT user subroutine will receive apart of $\boldsymbol{F}^{n+1}$ and $\boldsymbol{U}^{n+1}$, the t^n stress state $\boldsymbol{\sigma}^n_{\{\vec{e}_i^n \otimes \vec{e}_j^n\}}$ and the mid-point strain increment $\Delta\boldsymbol{\epsilon}^{n+1/2}_{\{\vec{e}_i^{n+1/2} \otimes \vec{e}_j^{n+1/2}\}}$ in the respective Green-Nadghi frames. We define the rotation tensors $\boldsymbol{\Theta}$ and $\Delta\mathbf{R}$ to transport stresses between the Green-Nadghi frames at t^{n+1} and $t^{n+1/2}$, and the fibre deformed frame.

$$\boldsymbol{\Theta} = (\vec{f_i}^{n+1} \cdot \vec{e}_j^{n+1})\vec{e}_i^{n+1} \otimes \vec{e}_j^{n+1} \text{ and } \Delta\mathbf{R} = (\vec{e}_i^{n+1} \cdot \vec{e}_j^{n+1/2})\vec{e}_i^{n+1} \otimes \vec{e}_j^{n+1} \tag{4.6}$$

The strain increments are transported from the Green-Naghdi frame to the fibre deformed using the rotation tensor $\boldsymbol{\Theta}^{n+1}_{\{\vec{e}_i \otimes \vec{f}_j\}} = (\vec{e}_i \cdot \vec{f}_j)\vec{e}_i \otimes \vec{f}_j$ as:

$$\Delta\boldsymbol{\epsilon}^{n+1}_{\{\vec{f}_i \otimes \vec{f}_j\}} = (\boldsymbol{\Theta}^{n+1})^T \Delta\boldsymbol{\epsilon}^{n+1}_{\{\vec{e}_i \otimes \vec{e}_j\}} \boldsymbol{\Theta}^{n+1} \tag{4.7}$$

The VUMAT subroutine provides the mid-point strain increment $\Delta\boldsymbol{\epsilon}^{n+1/2}_{\{\vec{e}_i^{n+1/2} \otimes \vec{e}_j^{n+1/2}\}}$, which is first, rotated to the Green-Nadghi t^{n+1} frame $\{\vec{e}_i^{n+1}\}$ frame and subsequently to the fibre-deformed frame $\{\vec{f}_i^{n+1}\}$ with the respective rotation tensors $\Delta\mathbf{R}$ and $\boldsymbol{\Theta}$. After constitutive computation, the stresses in the fibre-deformed frame $\Delta\boldsymbol{\sigma}^{n+1}_{\{\vec{f}_i^{n+1} \otimes \vec{f}_j^{n+1}\}}$ will be back-rotated into the Green-Nadghi frame $\Delta\boldsymbol{\sigma}^{n+1}_{\{\vec{e}_i^{n+1} \otimes \vec{e}_j^{n+1}\}}$.

The model assumes the viscoelastic behaviour of the material without considering Poisson effects. The viscoelastic stiffness operator is described by a fourth-order creep tensor as follows:

$$\mathbb{L}(t) = E_L\mathbb{J}_1 + 2\mu_T(\mathbb{J}_2 + \mathbb{J}_5) + 2\mu_L\mathbb{J}_6 \tag{4.8}$$

Where E_L, μ_T, and μ_L stand for the fibre direction, transverse and longitudinal shear modulus creep laws, respectively. Such constitutive formulation will be used in the fibre-deformed frame $\{\vec{f}_i^{n+1} \otimes \vec{f}_j^{n+1}\}^{n+1}$. The Walpole spectral decomposition was used in this formulation (Lubarda and Chen, 2008). For simplicity, the vector $(1, 0, 0)$ is aligned with the fibre direction, so the transverse isotropy plane is formed by the $2-3$ directions. The tensors $\boldsymbol{p}$ and $\boldsymbol{q}$ can be formed, and the fourth order tensors necessary for the spectral decomposition determined as $\mathbb{J}_1 = \boldsymbol{p} \otimes \boldsymbol{p}$, $\mathbb{J}_2 = 1/2(\boldsymbol{q} \otimes \boldsymbol{q})$, $\mathbb{J}_5 = 1/2(\boldsymbol{q} \cdot \mathbf{q} - \boldsymbol{p} \otimes \boldsymbol{q})$, and $\mathbb{J}_6 = 1/2(\boldsymbol{q} \otimes \boldsymbol{q})$. In this spectral decomposition, the fourth-order tensors used verify $\mathbb{I} = \mathbb{J}_1 + \mathbb{J}_2 + \mathbb{J}_5 + \mathbb{J}_6$ with $\mathbb{I}$ the unit tensor. The corresponding inner products satisfy the orthogonality condition.

In this work, only the longitudinal shear and transverse shear components experience viscoelasticity effects, which are defined in Prony's series as:

$$\mu_L(t) = \mu_L(1 - \sum_{i=1}^{N} g_{Li}(1 - e^{-\frac{t}{\tau_{Li}}})) \tag{4.9}$$

$$\mu_T(t) = \mu_T(1 - \sum_{i=1}^{N} g_{Ti}(1 - e^{-\frac{t}{\tau_{Ti}}})) \tag{4.10}$$

Where μ_L and μ_T are the initial shear response of the material, and g_{Li}, g_{Ti} and τ_{Li}, τ_{Ti} the N Prony's relaxation parameters. Such a formulation corresponds with a generalised Maxwell model containing a series of connected spring dashpots. After complete relaxation, the response of the material is given by $\mu_{L\infty} = \mu_L(1 - \sum_{i=1}^{N} g_{Li})$ and $\mu_{T\infty} = \mu_T(1 - \sum_{i=1}^{N} g_{Ti})$, respectively. Additionally, the relaxation operator is easily obtained by direct inversion as:

$$\mathbb{S}(t) = \frac{1}{E_L}\mathbb{J}_1 + \frac{1}{2\mu_T}(\mathbb{J}_2 + \mathbb{J}_5) + \frac{1}{2\mu_L}\mathbb{J}_6 \tag{4.11}$$

The stress response for a given strain history can be determined by assuming viscoelasticity principles as:

$$\boldsymbol{\sigma}(t) = \mathbb{L}(t)\boldsymbol{\epsilon}_0 + \int_0^t \mathbb{L}(t-\tau)\dot{\boldsymbol{\epsilon}}(\tau)\, d\tau = \mathbb{L}(t)\boldsymbol{\epsilon}_0 + \mathbb{L}(t) \circ \dot{\boldsymbol{\epsilon}} \tag{4.12}$$

Where $\boldsymbol{\epsilon}_0$ and $\dot{\boldsymbol{\epsilon}}$ are the initial strain and the strain time derivative, respectively. The symbol $\circ$ denotes convolution operation. The numerical integration of the viscoelastic response was carried out according to the procedure described in Kaliske, 2000; Kaliske and Rothert, 1997. To this end, the longitudinal and transverse viscoelastic stresses in each of the Maxwell elements arms, $\boldsymbol{h}_{Li}$ and $\boldsymbol{h}_{Ti}$ can be determined by the following recursive relation (Kaliske and Rothert, 1997):

$$\boldsymbol{h}_{Li}^{n+1} \approx \boldsymbol{h}_{Li}^{n} e^{-\frac{t}{\tau_{Li}}} + 2\mu_{Li}\frac{1 - e^{-\frac{t}{\tau_{Li}}}}{\frac{t}{\tau_{Li}}}\mathbb{J}_6\Delta\boldsymbol{\epsilon} \tag{4.13}$$

$$\boldsymbol{h}_{Ti}^{n+1} \approx \boldsymbol{h}_{Ti}^{n} e^{-\frac{t}{\tau_{Ti}}} + 2\mu_{Ti} \frac{1 - e^{-\frac{t}{\tau_{Ti}}}}{\frac{t}{\tau_{Ti}}} (\mathbb{J}_2 + \mathbb{J}_5) \Delta\boldsymbol{\epsilon} \tag{4.14}$$

With μ_{Li} and μ_{Ti} stand for the elastic spring moduli of each Maxwell's, respectively. Such values can also be expressed in terms of Prony's coefficients as:

$$\mu_{Li} = \frac{g_{Li}}{1 - \sum_{i=1}^{N} g_{Li}} \text{ and } \mu_{Ti} = \frac{g_{Ti}}{1 - \sum_{i=1}^{N} g_{Ti}} \tag{4.15}$$

Lastly, the total stress carried by the generalised Maxwell system is computed as:

$$\boldsymbol{\sigma}^{n+1} = \boldsymbol{\sigma}_{\infty}^{n+1} + \sum_{i=1}^{N} \boldsymbol{h}_{Li}^{n+1} + \sum_{i=1}^{N} \boldsymbol{h}_{Ti}^{n+1} \text{ with } \boldsymbol{\sigma}_{\infty}^{n+1} = \mathbb{L}_{\infty} \boldsymbol{\epsilon}^{n+1} \tag{4.16}$$

With $\mathbb{L}_{\infty}$ as the viscoelastic operator after complete relaxation obtained with $\mu_{L\infty}$ and $\mu_{T\infty}$. For the case of two Maxwell viscoelastic branches, a total of five parameters for each deformation mode are necessary, namely $[\mu_L, g_{L1}, g_{L2}, \tau_{L1}, \tau_{L2}]$ and $[\mu_T, g_{T1}, g_{T2}, \tau_{T1}, \tau_{T2}]$ together with the elastic modulus in the fibre direction E_L which was assumed to be time-independent.

4.2.1 Validation and implementation of the VUMAT

This section is dedicated to validating the Abaqus user Fortran routine for the dynamic analysis of viscoelastic fibre-reinforced composites. By using equation 4.12, the evolution of the stress state $\boldsymbol{\sigma}(t)$ for a given strain history $\boldsymbol{\epsilon}(t)$ is determined by performing convolution operations following:

$$\boldsymbol{\sigma}(t) = \mathbb{L}(t)\boldsymbol{\epsilon}_0 + \mathbb{L}(t) \circ \dot{\boldsymbol{\epsilon}} \tag{4.17}$$

The correlation was done by comparing the VUMAT response with the direct analytical integration of the viscoelastic constitutive equation using the Laplace-Carson transform for simple loading cases. In this case, a constant velocity deformation history is used as $\boldsymbol{\epsilon}(t) = \boldsymbol{c}t$, where $\boldsymbol{c}$ is the strain rate tensor. For instance, if longitudinal or transversal shear strain rates are imposed, then $\gamma_L(t) = c\,t$ or $\gamma_T(t) = c\,t$ where c stands for the prescribed strain velocity. The Laplace-Carson transformed the time domain viscoelastic constitutive law (4.17) into the p domain as

$$\hat{\boldsymbol{\sigma}}(p) = \hat{\mathbb{L}}(p)\hat{\boldsymbol{\epsilon}}(p) \tag{4.18}$$

with $\hat{\mathbb{L}}(p) = E_L\mathbb{J}_1 + 2\hat{\mu}_T(p)(\mathbb{J}_2 + \mathbb{J}_5) + 2\hat{\mu}_L(p)\mathbb{J}_6$. If the strain history is $\boldsymbol{\epsilon}(t) = \boldsymbol{c}t$, then the Laplace-Carson transformed is $\hat{\boldsymbol{\epsilon}}(p) = \boldsymbol{c}/p$ so the calculation of the corresponding stress tensor is straightforward

$$\hat{\tau}_L(p) = 2\hat{\mu}_L(p)\frac{c}{p} \quad \text{and} \quad \hat{\tau}_T(p) = 2\hat{\mu}_T(p)\frac{c}{p} \tag{4.19}$$

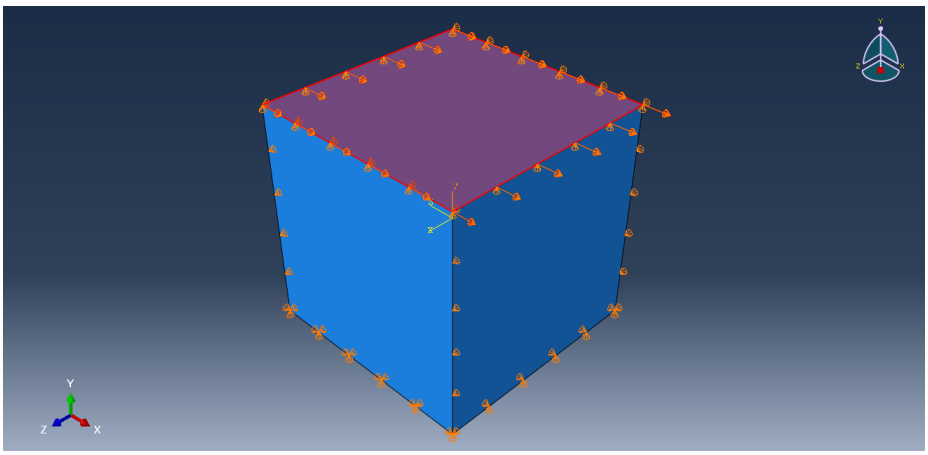

Figure 4.3: Abaqus model with a single element for validating the user subroutine. The model is subjected to simple shear by applying relative displacements between opposite faces of the element at different velocities.

with the Laplace-Carson transformed $\hat{\mu}_T(p)$ and $\hat{\mu}_L(p)$ Prony's series as as

$$\hat{\mu}_L(p) = \mu_L(1 - \sum_i^N \frac{g_{Li}}{\tau_{Li}} \frac{1}{p + \frac{1}{\tau_{Li}}}) \quad \text{and} \quad \hat{\mu}_T(p) = \mu_T(1 - \sum_i^N \frac{g_{Li}}{\tau_{Li}} \frac{1}{p + \frac{1}{\tau_{Li}}}) \tag{4.20}$$

Introducing equation 4.20 into equation 4.19, simplifying and applying the inverse transformation of the Laplace-Carson to return to the time domain t, the response in shear for constant velocity tests are obtained accordingly

$$\tau_L(t) = 2\mu_L c \left(t - \sum_i^N g_{Li} t + \sum_i^N g_{Li}\tau_{Li}(1 - e^{-\frac{t}{\tau_{Li}}}) \right) \tag{4.21}$$

$$\tau_T(t) = 2\mu_T c \left(t - \sum_i^N g_{Ti} t + \sum_i^N g_{Ti}\tau_{Ti}(1 - e^{-\frac{t}{\tau_{Ti}}}) \right) \tag{4.22}$$

Equations 4.21 and 4.22 were compared with the corresponding response obtained with the Kaliske integration of the viscoelastic response through the VUMAT under 0.006, 0.012 and 0.024 mm/min using arbitrary material properties with two Maxwell mechanisms for longitudinal and transverse shear. The agreement was excellent, with a clear identification of the velocity's role in the material's viscoelastic response.

4.2.2 Simulation of the $[\pm 45]_{2s}$ experimental case

After numerically validating the VUMAT using a single element, it is necessary to conduct a validation of the full tensile test. A specimen is modelled using the Finite Element Method (FEM) in the Abaqus software interface, considering an explicit solver. The model consists of 8 layers with a stacking sequence of $[\pm 45]_{2s}$. The total number of elements is 8720, with 19360 nodes. The model, designed specifically for this circumstance, faithfully reproduces the cured tabs, assuming tightly connected contacts between layers as an essential simplification to replicate the complexities of the real situation. The boundary conditions simulate the

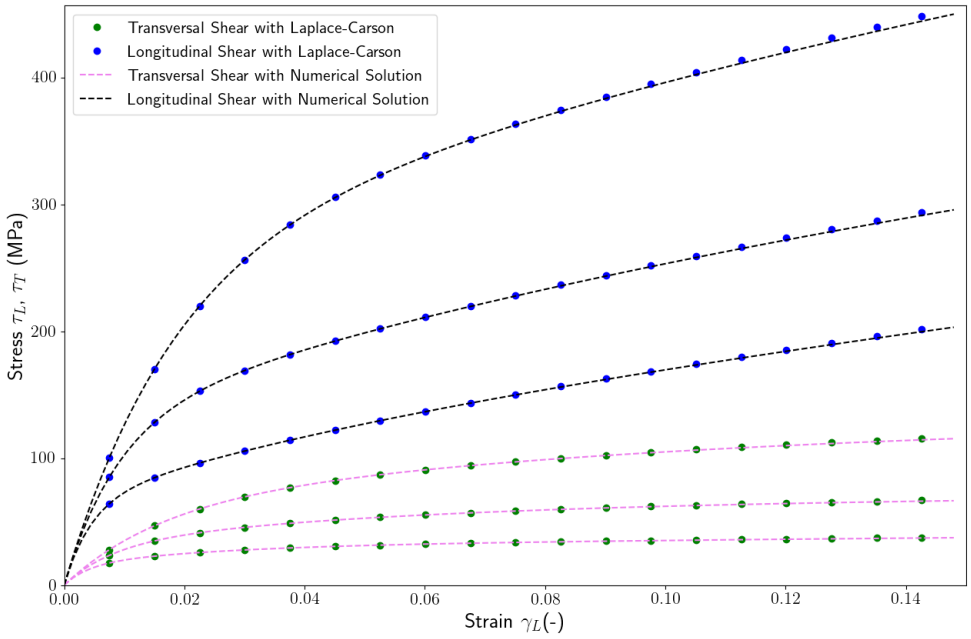

Figure 4.4: Validation of VUMAT time integration with an analytical model obtained by applying the Laplace-Carson transform to longitudinal and transverse shear tests at constant velocities of 0.006, 0.012, 0.024 mm/min.

tensile tests by fixing one end of the specimen and applying strain rate control to the opposite end. Figure 4.5 illustrates the design of the specimen.

In order to replicate the experimental testing, the simulated specimen is designed to have identical dimensions to the actual specimen, measuring 200x20 mm. Additionally, the grip used in the simulation measures 20x20 mm^2. Three velocities were employed to regulate the tensile test in the simulation: 0.5 mm/min, 1 mm/min, and 2 mm/min which correspond to the experimental testing conditions. This was done to examine the impact of the strain rate in the material and observe the viscoelastic effect.

Figure 4.6a demonstrates that the numerical simulation closely approximates the experimental data. The presence of variation in the curves is attributed to the boundary conditions employed in the simulation. In this simulation, the layers are assumed to be tied together, implying that the interactions between the plies are neglected and not considered. Enhanced outcomes can be achieved by considering the cohesive contact within the same layer and effectively utilising the findings from friction tests. Another unconsidered element was the impact of the observed fibre rotations during the experiments. Although the experiments were stopped prior to achieving a noticeable fibre rotation, a minor rotation may occur within the strain range we investigated. This minimal rotation may slightly modify the stress response, which is not taken into account in the current stage of the computer model. Due to time constraints and the need for conciseness, simulations with those conditions were not conducted. However, the implementation of contacts to more accurately align with the experimental results is left for future consideration.

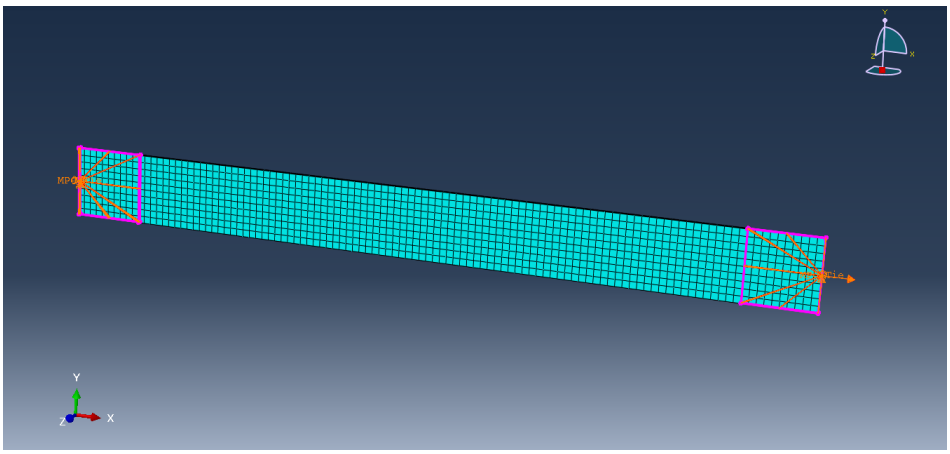

Figure 4.5: Numerical Model of the $[\pm 45]_{2s}$ specimen

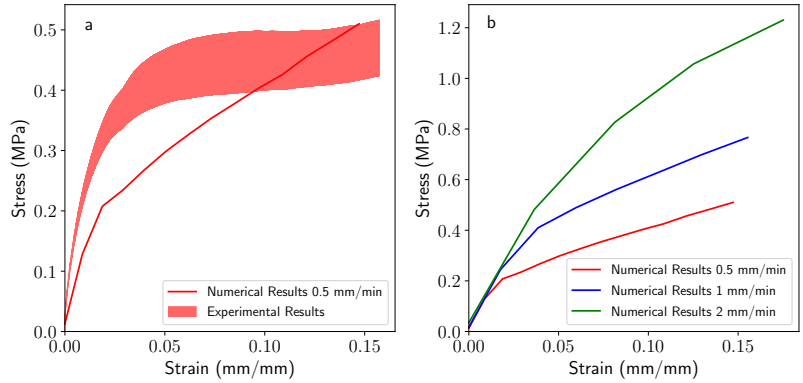

Figure 4.6: a) Impact of strain rate on the viscoelastic material in the numerical specimen when the VUMAT routine is utilised. b) Comparison between the Numerical Results obtained with Abaqus using the VUMAT and the experiments on the specimen $[\pm 45]_{2s}$.

Nevertheless, Figure 4.6b demonstrates the impact of strain rate on the $[\pm 45]_{2s}$ specimen. The results in this case are quite accurate. It is feasible to observe the impact of velocity on the viscoelastic behaviour of the material, just as this effect is observed in the experimental findings. This supports, affirms, and verifies the findings achieved with the VUMAT depicted in Figure 4.4 in the preceding paragraph.

4.3 Interply friction modelling: lubrication theory

The friction process in the range of the experimental data was modelled using the lubrication theory (Rashidi et al., 2021). The geometry of the rough surface of the prepreg ply was modelled as a sinusoidal function (Burstein, 2008), as sketched in Figure 4.7 where:

$$y^{+}(x) = \frac{h_0}{2} + A\cos(\frac{2\pi x}{L}) \tag{4.23}$$

$$y^{-}(x) = -\frac{h_0}{2} - A\cos(\frac{2\pi x}{L} + \delta) \tag{4.24}$$

In this expression, A stands for the wave amplitude, L is its wavelength, and $h_0/2$ is half of the total average thickness of the resin layer. The fibre direction is aligned with the x axis in Figure 4.7 a). The roughness measurement estimated the amplitude A of the rough surface, while the optical images were used to characterise the roughness wavelength L. The same amplitude and wavelength were used for all the calculations irrespective of the testing conditions (temperature, velocity and pressure). In the case of prepreg-prepreg contact, it can be assumed that both waves are equal but delayed with a phase angle $\delta[0, 2\pi]$. Therefore, the thickness of the resin layer can be calculated by subtracting $y^+(x) - y^-(x)$ as

$$h(x) = h_0 + 2A_0 \cos\delta \cos(\frac{2\pi x}{L} + \delta) \tag{4.25}$$

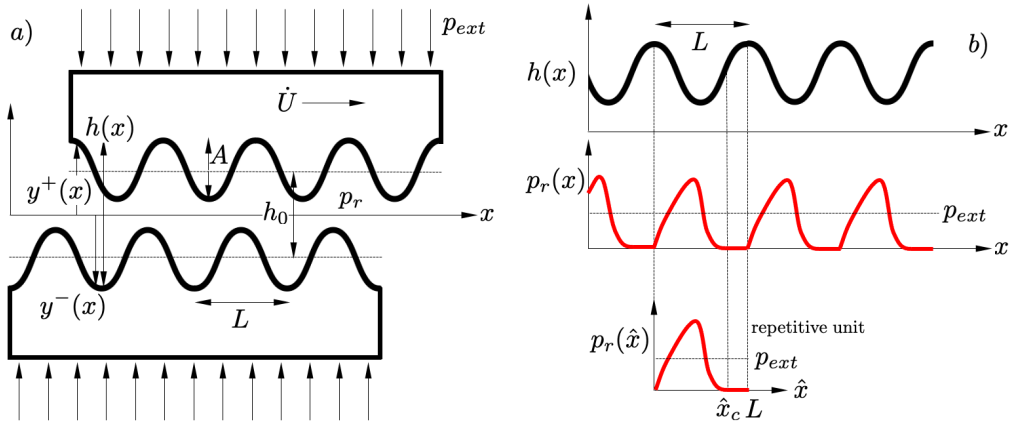

Figure 4.7: a) Geometry of the two rubbing surfaces, b) Sketch of the pressure distribution during sliding.

Assuming that the upper part of the model slides respecting the lower at a rate given by $\dot{U}$, the resin pressure inside the layer is developed according to the Reynolds theory. Without loss of generality, the resin pressure distribution p_r in the sliding length can be studied by analysing a repeating unit in the domain $\hat{x}[0, L]$, see Figure 4.7 b)

Under these assumptions, the pressure distribution $p_r(\hat{x})$ is governed by the one-dimensional Reynolds equation according to

$$\frac{\partial}{\partial \hat{x}}(\frac{h^3}{\eta}\frac{\partial p_r}{\partial \hat{x}}) = 6\dot{U}\frac{\partial h}{\partial \hat{x}} \tag{4.26}$$

This differential equation is solved with two zero pressure boundary conditions at the edges $p_r(\hat{x} = 0) = p_r(\hat{x} = x_c) = 0$. The point $\hat{x} = x_c$ is also known as the cavitation point at which the gradient of pressure becomes null; therefore, its spatial derivative is $\partial p_r/\partial \hat{x} = 0$.

The total averaged external pressure acting on the resin can be computed by integration of the pressure distribution over the domain $\bar{p}_r = \int_0^L p_r(\hat{x})\, d\hat{x}$ and due to equilibrium conditions it should be equal to the applied external pressure $\bar{p}_r = p_{ext}$. Given the applied external pressure p_{ext}, the Reynolds equation's solution is obtained using a finite difference scheme.

The details of the discretisation of the Reynolds equation can be found in Appendix A. The model calculations start by assuming the cavity thickness h_0, the wave amplitude and length A and L as inputs. For the given thickness h_0, the cavitation point $\hat{x}_c$ is first determined iteratively by solving the Reynolds equation until the condition $\partial p_r/\partial \hat{x} = 0$ is satisfied. The resin pressure field $p_r(\hat{x})$ is calculated, and the averaged value is assumed as the external pressure applied p_{ext}. Afterwards, the shear stress distribution $\tau_r(\hat{x})$ is determined according to

$$\tau_r(\hat{x}) = \eta \frac{\dot{U}}{h} + \frac{h}{2}\frac{\partial p_r}{\partial \hat{x}} \tag{4.27}$$

being the averaged value $\bar{\tau}_r$ the results of its integration over the domain as $\bar{\tau}_r = \int_0^L \tau_r(\hat{x})\, d\hat{x}$. Lastly, the friction coefficient is determined as $\mu = \bar{\tau}_r/\bar{p}_r$ as a function of the applied pressure, velocity and viscosity. The model outputs are summarised in terms of a curve with the dependence of the friction coefficient on the Hersey number as $\mu = \mu(H) = \mu(\eta\dot{U}/p)$. The model can also be applied for prepreg-tool contact by simply decreasing the amplitude in equation 4.25 to half of the current prepreg-prepreg value, although the model's sensitivity in this range is not remarkable.

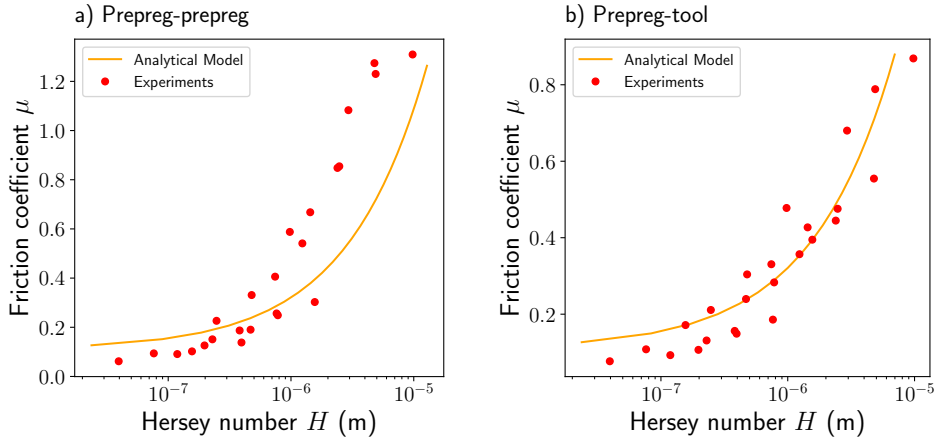

Figure 4.8: Comparisons between the analytical model and experimental results for the Stribeck curves for the friction coefficient: a) Prepreg-prepreg contact, b) Prepreg-tool contact.

According to the formulation described in the previous section, the model inputs necessary were the wavelength L and the surface roughness or wave amplitude A. The first variable is estimated from a distance between the accumulated resin peaks observed on the prepreg surface after friction and the second value from the mean amplitude corresponding to the rough surface geometry. The respective values were set from the profilometry analysis and the optical microscope examinations (Table 3.1) to $L \approx 64\mu$m and $A \approx 3.5\mu$m. For the case of Ply-Tool, it was considered that the rough surfaces involved in the friction mechanism were the same as the other case since the experimental analyses presented similar outcomes. The range of resin layer thickness was $h_0 = [3 - 15\mu\text{m}]$, covering the experimental values measured from the consolidated coupons presented in Figure 3.11 c). The predictions of the friction coefficient

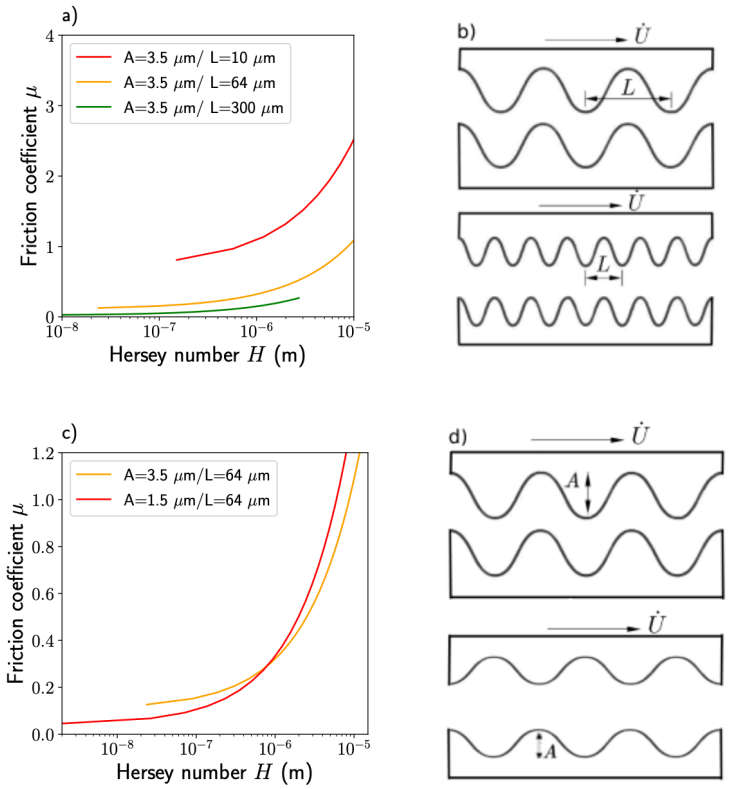

Figure 4.9: Model sensitivity analysis: a) Effect of wavelength L variation keeping a constant roughness A, b) schematic illustration of the wavelength changing. In c) is the effect of the roughness variation keeping constant wavelength L, in d) is the schematic illustration of Amplitude changing.

as a function of the Hersey number $\mu = \mu(H)$ obtained using the baseline model parameters are presented in Figure 4.8 a) for prepreg-prepreg and 4.8 b) prepreg-tool contacts. Each experimental case tested is represented by solid symbols, while the continuous line represents the analytical prediction with the Reynolds model. As shown, the model reasonably suits the experimental results for both cases with a slight discrepancy with the prepreg-prepreg contact case at high values of the Hersey number. The friction coefficients in this part of the curve correspond with the experiments carried out at 40°C. At this temperature, the resin was less viscous and sliding can be interpreted as dry lubrication, producing an increase in the shear stress and, consequently, higher friction values (Burstein, 2008; Heshmat and Walton, 2016). This effect is not observed for the prepreg-tool case since the metal surface contains fewer asperities, allowing an easier slide and, therefore, lower friction value.

The model sensitivity to the input parameters was inspected by varying the values of wavelength L and roughness A. From Figure 4.9 a) can be concluded that a higher wavelength value L significantly reduces the friction coefficients. The resin build-up pressure p_r due to the geometrical effects is less pronounced as L increases. The illustration presented in Figure 4.9 b) evidences this occurrence by representing the effect of having a high or low wavelength on the same rough surface. The presence of more resin accumulations (i.e. low wavelength

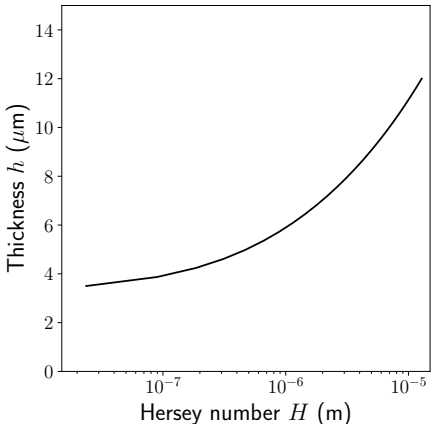

Figure 4.10: Interlayer resin thickness, predicted with the developed model, as a function of the Hersey number.

value) restrains the slide between both surfaces. In comparison, fewer resin accumulations (i.e. high wavelength value) make the prepreg surface easier to pull out. On the other side, by changing the roughness value A, the curve tends to change the friction slope against the Hersey number. However, by exploring the scatter values observed in the roughness A (see Table 3.1), no significant variation was observed, see Figure 4.9 c) and the corresponding representative illustration 4.9 d).

In addition to the analytical model's estimation of friction coefficients and Hersey numbers, a range of resin layer thicknesses associated with a Hersey number is obtained as an auxiliary outcome of the model. The results are presented in Figure 4.10. This output can be employed to obtain the value of the parameters governing the phenomenon, i.e. the expected thickness of the equivalent sliding layer if the Hersey number is estimated.

4.3.1 Resolution of the Reynolds equation

The Reynolds equation is solved employing finite differences by discretising the $\hat{x}$ domain between $[0, L]$ with n divisions.

$$\frac{\partial}{\partial \hat{x}}(\frac{h^3}{\eta}\frac{\partial p_r}{\partial \hat{x}}) = 6\dot{U}f(x) \tag{4.28}$$

where $f(x) = \frac{\partial h}{\partial \hat{x}}$ is the analytical derivative of the cavity thickness function. The first and second derivatives of the equation were discretised using central differences leading to the following 3-point stencil

$$(\frac{1}{\Delta x^2} + \frac{3f_i}{2\Delta x h_i})p_{i+1} - \frac{2}{\Delta x^2}p_i + (\frac{1}{\Delta x^2} - \frac{3f_i}{2\Delta x h_i})p_{i-1} = 6\eta\dot{U}\frac{f_i}{h_i^3} \tag{4.29}$$

The resulting linear equation system is constrained with the resin pressure at boundaries $p_r(\hat{x} = 0)$ and $p_r(\hat{x}_c) = 0$. The selection of x_c is achieved iteratively until the additional cavitation condition is fulfilled $\partial p_r(\hat{x}_c)/\partial \hat{x} = 0$. Pressure and shear stress for $\hat{x} > \hat{x}_c$

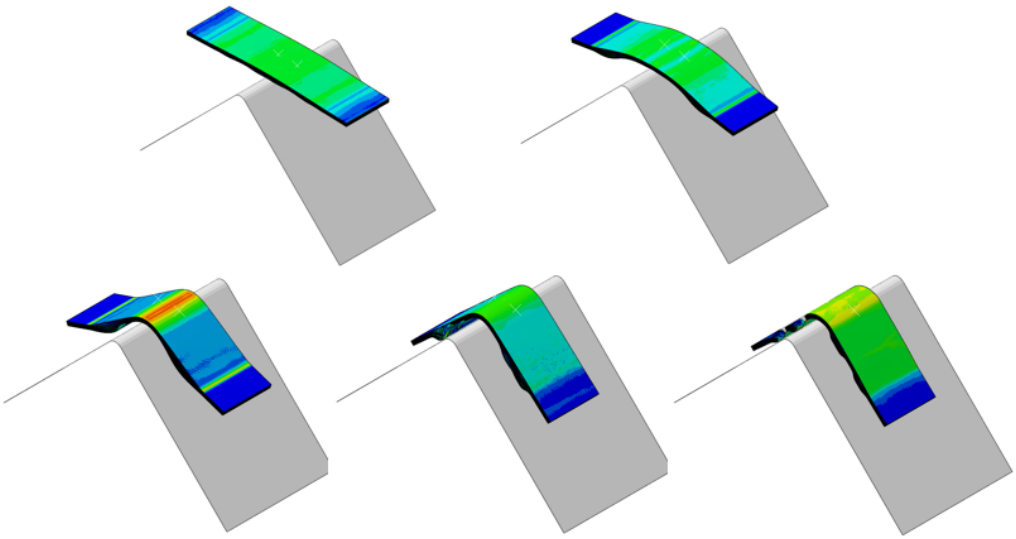

Figure 4.11: Representation of thermoforming geometry

were assumed to be zero. Once x_c is found, the thickness average cavity thickness h_0 is increased/decreased until the average pressure is equal to the external one. Then, the corresponding shear stress and the friction coefficient are computed for the given friction conditions (pressure, temperature and sliding velocity).

4.4 Thermoforming Modeling

The overall objective of this study is to contribute to the thermoforming production process by comprehending the occurrence of defects such as wrinkles and seeking to determine the optimal combination of process parameters to improve production. A model was designed to simulate the consolidation process of a rectangular unidirectional prepreg laminate $[0]_{32}$ with a thickness of 6.4 mm. The laminate was placed on a rigid angular surface with a radius of 10mm. Figure 4.11 illustrates the geometric configuration of the stress distribution problem, which comprises a curved tool and two closing components that induce the bending of the laminate around the filled corner. As the forming parts are lowered, the laminate experiences tension, leading to the compression of layers, subsequent buckling in a direction perpendicular to the plane, and ultimately, the creation of wrinkles.

Simultaneously, a fresh prepreg laminate consisting of 4 layers and a laminate sequence of $[0]_4$ is employed to explore the difficulties with reduced computing time. Both configurations are positioned on a hard surface that forms a 90° angle with an established radius of 10 mm. The force is applied through a membrane, producing a displacement of 120mm. This displacement corresponds to the actual movement of the membrane in a real thermoforming production process. At the same time, a pressure of 1 bar is applied to compress the membrane. This compression allows the laminate to adapt to the tool once the displacement movement is

finished.

The mesh employed is solid, consisting of 8 nodes per element. The 4-layer model comprises 275,000 elements, while the 32-layer model comprises 515000 elements. The computation approach used is explicit. Figure 4.12 displays the initial arrangement of the simulation for the 4-layer carbon and its related mesh. The 32-layer laminate yields a comparable arrangement.

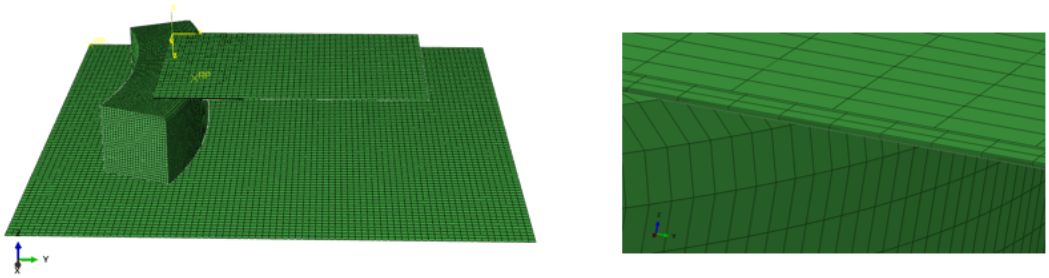

Figure 4.12: Example of the mesh used in the simulation of thermoforming process

Throughout the production process, the laminates undergo different stress states. One distinctive characteristic is that the fresh prepreg exhibits a low level of adhesion between its layers, resulting in the layers sliding in relation to each other during the displacements. This impacts the density of the laminate, resulting in imperfections such as wrinkles. This phenomenon may be effectively visualised through modelling, wherein the bending of both the 4-layer and 32-layer laminates demonstrated a noticeable absence of adhesion between layers and the creation of wrinkles. The contact between the layers is established through a cohesive interlayer, while the damage is simulated using the Benzeggagh-Kenane cohesive surface law and a traction-separation law. As demonstrated in the previous chapters, the energy and stress values utilised are derived from friction tests conducted exclusively on laminates.

Figure 4.13 depicts the industrial production process of a curved prepreg composite part using the thermoforming technique. This example focuses on the intentional creation of defects by constraining certain edges of the laminate with a layer of cork.

The simulations attempt to recreate the identical circumstances found in actual production settings accurately. Every numerical calculation yields an output that accurately replicates the angular component. The imperfections formed in a curved 4-layer composite are prominently exhibited in Figure 4.14. The membrane is evidently lowered to exert pressure on the laminate, resulting in the delamination of the layers and the creation of wrinkles. The leading cause of wrinkle formation is inadequate adhesion resulting from incomplete prepreg curing, as previously stated. The lack of sufficient adhesion between the layers and the shear force causes the uncured resin to insufficiently resist friction, resulting in the sliding of the fibre plies.

By employing a simulation that closely replicates the actual scenario, one may effectively observe the complete progression of deformation over time and the subsequent separation and sliding of layers. Figure 4.15 depicts the complete progress of the 32-layer model, focusing specifically on the development of wrinkles.

Figure 4.13: Experimental thermoforming production process of prepreg with wrinkle formation

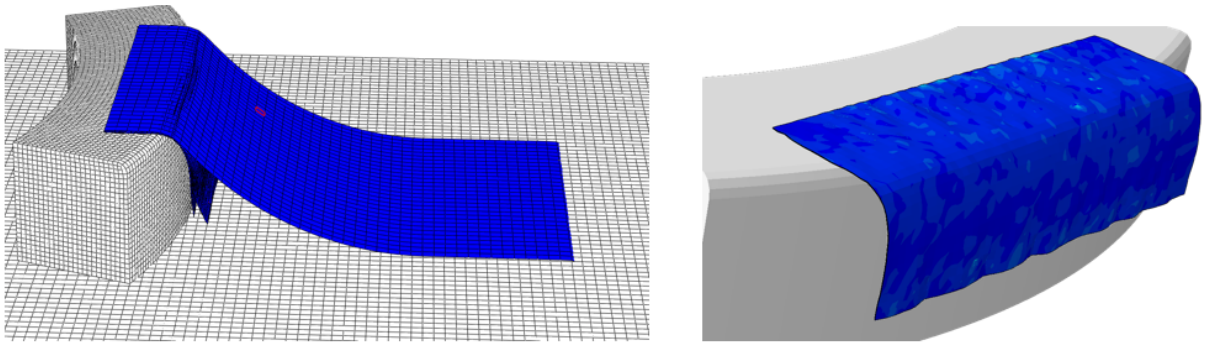

Figure 4.14: Simulation results of thermoforming process for the 4 layer laminate

At last, Figure 4.16 compares the computer model and the actual result created using a thermoforming technique. Both exhibit visible wrinkles, along with other shared characteristics such as the shape of the wrinkles and the sliding of layers.

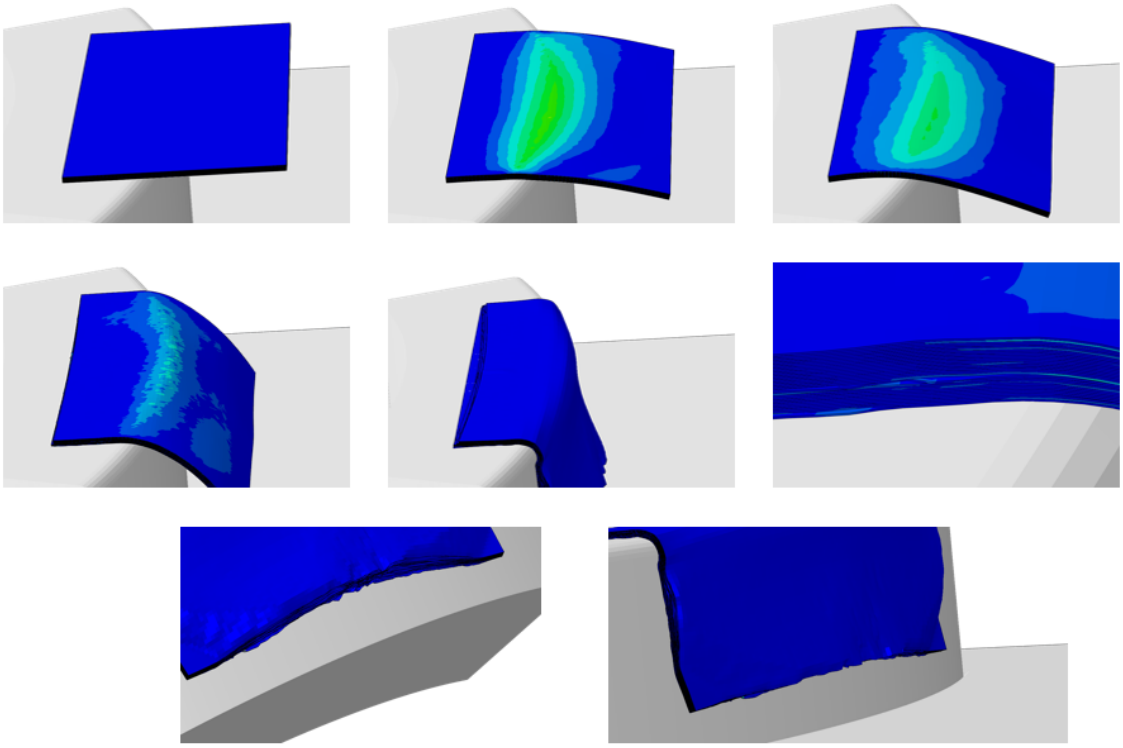

Figure 4.15: Evolution in the time of the simulation of the thermoforming process for the 32-layer laminate.

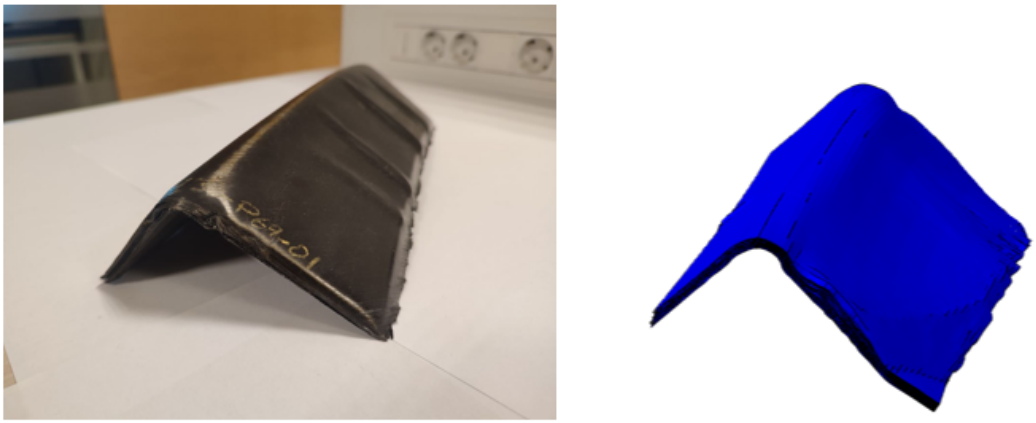

Figure 4.16: A comparison between the results of the numerical model of a 32-layer thermoformed prepreg and a real manufactured product

Chapter 5

Conclusions and Future Work

A thorough investigation and mechanical characterisation of the uncured preimpregnated AS4/8552 composite material were conducted as part of this research. This comprehensive investigation was motivated by the industrial application of the material in a thermoforming process that is frequently used in the aeronautical manufacturing industry. The exploration was carefully organised, considering a range of significant factors present during the processing, including temperature, speed of compaction, pressure during consolidation, friction, and the order in which laminates were stacked. The objective was to reveal detailed and subtle observations about the behaviour and reactions of the material under different testing and operational circumstances. The findings established a firm basis for practical use in the manufacturing process and as a standard for computational models and additional simulations of the process that involve uncured prepreg composite.

5.1 Conclusions

In terms of the experimental aspect of the study, the key finding was the observation of the distinctive features of this specific material in its uncured stage when exposed to the mechanical forces usually encountered during thermoforming procedures. The proposed sample production method of selectively curing the coupons' edges while leaving the middle part uncured was critical in the construction of this thesis. It allowed for detailed mechanical characterisation, demonstrating a considerable difference of around 50% in the material's stress capacity compared to when the edges were not cured in the most significant case. The issue of the interface slipping in the uncured prepreg laminate was effectively overcome by introducing a partial curing mechanism (See section 2.3.2). Subsequent experiments revealed a substantial relationship between the stress reaction and the working temperature, making it the most impactful variable during testing. Even though heat reduces the material's stress resistance significantly, friction, compaction, and laminate freedom to deformation frequently cause defects in the thermoforming manufacturing process. The mechanical response will vary depending on the resin migration from semi-solid to fluid upon heat application. Testing the material at various strain rates causes a viscoelastic impact that affects this response, which can have both linear-elastic and non-linear stress-strain responses.

In the case of a longitudinal tensile test, the mechanical reaction was purely linear-elastic. This is because the stress in this direction is mostly carried by the solid carbon fibres, which are slightly influenced by the heating conditions. The absence of a viscoelastic effect was observed, as it is primarily a resin property that has a negligible impact on the stress in this particular direction.

The transverse tensile test revealed the anisotropy commonly observed in UD fibre-reinforced laminates, highlighting the matrix's crucial function in supporting the composite structure under lateral stresses. However, when exposed to elevated temperatures, the resin's resistance was insufficient to conduct a transverse tensile test on a universal tensile machine at the necessary dimensions due to pre-loading damages in the sample. This inconvenience has resulted in adopting alternate testing approaches, such as using a specialised rheometer that enables the execution of the identical test but on a smaller scale. The outcome yielded a significantly improved analysis of the stress-strain behaviour and the viscoelastic phenomenon. The stress-strain curve exhibits a consistent non-linear pattern in all cases involving limited tensile deformation, accompanied by clear indications of damage and fibre-bridging. A notable observation made from this test was the diminishing impact of varying strain rates on the stress response as the temperature increased. This phenomenon indicates that the material exhibits non-Newtonian behaviour at a specific temperature. This is evident since the material reaches the same stress level at different strain rates, which indicates varied viscosity. The specific type of non-Newtonian fluid was identified as pseudoplastic.

The same phenomenon is shown in the case of tensile shear stress, where an identical stress response is observed for all applied strain rates at temperatures of 40°C and 60°C. In both cases, the curves exhibited distinct slopes that can be attributed to an initial elastic reaction before the occurrence of damage, followed by an elastoplastic deformation. At this temperature, the samples exhibited a degree of freedom for the fibres to rotate, resulting in a consistent increase in stress until the damage progresses and the testing is completed. On the contrary, the samples at room temperature exhibited a distinctive viscoelastic effect characterised by a non-linear pattern.

Concerning the analysis of friction, a device was designed to conduct experiments on uncured prepreg composite, enabling the examination of the interaction between the composite layers and between the material and the mould. The observed results generated multiple uncertainties, forcing a more thorough examination using supplementary techniques such as profilometry, tomography, and microscopic analyses. Upon examination of the material surface before and after the test, distinct geometric features were seen, including resin accumulations, exposed fibres, and, most notably, a lubricant layer between the surfaces. The experimental outcomes were mathematically represented using analytical theories such as the lubrication theory and the Reynolds equation. The Stribeck curve was used to understand better the hydrodynamic lubrication regime observed in our case study. The result is a set of formulae that enable us to calculate friction values based on knowledge of the material viscosity and the process parameters.

The investigation into the compaction behaviour of uncured prepreg laminates reveals the significant influence of layup configuration and temperature on the compaction process. Layups incorporating transverse fibres demonstrate increased resistance to compaction, reflecting in

lesser thickness reduction, a manifestation of the fibre bed effect. This resistance is notably due to the fibres hindering resin flow during compaction, resulting in a higher load response. Elevating the temperature alters the resin's characteristics, reducing its viscoelastic behaviour and enhancing its capacity to flow. Such changes lead to a diminished fibre bed effect and decreased load response during compaction, enabling more consistent and uniform compaction across various layup configurations. The impact of temperature is particularly pronounced at higher levels, where it substantially lessens the differences in compaction resistance between layups with varying fibre orientations. As a result, at increased temperatures, the laminate's ability to compact is less affected by the ply configuration, allowing for a more efficient compaction process. This suggests that temperature-conditioned resin behaviour is a critical factor in the laminate compaction outcome, providing insights into optimising manufacturing processes for composite materials.

When subjected to bending loads, the two-point bending test accurately captures wrinkle formation in composite materials. The test's ability to establish a connection between increases in torsional strain and the onset and development of wrinkles offers a vital understanding of the mechanics of defect creation. By conducting meticulous monitoring, the test uncovers the correlation between the material's reaction to stress and the formation of wrinkles, which serves as a crucial indicator of composites' structural boundaries and restrictions. Adopting this scientific approach is crucial for enhancing our comprehension of material behaviour and the adverse impact of wrinkle formation in manufacturing processes for composite constructions.

This research has made significant progress in characterising the behaviour of uncured prepreg materials in the numerical aspect. The study successfully captures the complex viscoelastic features of these materials by employing a methodology grounded in the generalised Maxwell model. This method was essential in precisely replicating the material's behaviour, especially when dealing with different shear and velocity circumstances.The numerical study revealed that the model effectively replicated the viscoelastic behaviour of the material, as demonstrated by its agreement with theoretical predictions and proven integration methods. The work demonstrates the capacity to establish a connection between shear response and various velocity tests, emphasising the significance of strain rate in determining material behaviour. These findings provide useful insights for practical applications.

The integration of the VUMAT subroutine into the Finite Element Method (FEM) using Abaqus software was successful in accurately simulating the behaviour of a $[\pm 45]_{2s}$ specimen. The numerical simulations correctly replicated real-world conditions, demonstrating the model's ability to capture the viscoelastic behaviour of the material at different strain rates with a high degree of fidelity. It is valuable to acknowledge that there were slight discrepancies detected in the simulation curves. The inconsistencies are mostly caused by the particular boundary conditions used in the simulation.

The last segment of the numerical simulations focused on achieving one of the goals of this thesis, which was to computationally model the thermoforming manufacturing process. Two laminates were consolidated onto a curved metallic mould using a regular thermoforming process with restricted deformation to intentionally create imperfections in the final product. Computational simulations and our vectorized user material were used to process the stress and strain distributions in order to replicate the same process. The simulations accurately

represented the occurrence of low adhesion between layers, resulting in the sliding of layers and the creation of wrinkles in both 4-layer and 32-layer laminates. The friction outcomes were used as parameters to indicate the energy and stress in the cohesive interlayer of the Benzeggagh-Kenane model. This model represented the insufficient adhesion caused by incomplete prepreg curing, which ultimately led to the whole progression of deformation, layer separation, and sliding. The definitive comparison between the computer model and the physical thermoformed result revealed notable resemblances, such as observable wrinkles and other common attributes, including wrinkle shape and deformations.

5.2 Future research

The journey towards accurately characterising the material involved unexpected obstacles, uncertainties, and several decisions. These were necessary to establish a foundation for accurately describing the thermoforming manufacturing process and developing an initial material model. Certain aspects of the material were neglected, along with numerous possible suggestions to characterise or thoroughly investigate the behaviour of the laminate during the production process. This thesis will provide suggestions and information about potential future research that could enhance and complement the investigation.

- Initially, it was discovered that there is a lack of viscosity data for the AS4/8552 material at temperatures lower than 40°C. In order to fill this void, the viscosity was approximated using the Arrhenius equation. To facilitate future research, it is recommended to experimentally measure the viscosity of this prepreg material at temperature ranges where data are currently unavailable.
- An important focus of research involves investigating the rotation of fibres that occurs during the mechanical testing of uncured prepreg materials. Although attempts were taken to limit this occurrence by keeping the strain range free from fibre rotation, it would be remarkable to conduct additional research on its impact on mechanical behaviour and the interaction of laminates. Considering the rotation of fibres could allow for investigations with greater strain ranges, therefore enabling more comprehensive simulations. These simulations would be useful in investigating the shapes of components that experience significant deformation, leading to a more comprehensive comprehension of material properties under different circumstances.
- Additional defects detected during the high strain test included fibre bridging, fibre breakage, and resin bleeding (particularly in situations involving compaction). These defects were not considered in our existing calculations and formulations, so analysing their behaviour could be critical to understanding the failure modes of uncured prepreg laminates. Exploring these events has the potential to provide significant parameters for developing more detailed damage models.
- The stacking sequence in a laminate is a crucial factor in the design of new components, as it directly influences their behaviour. Examining various stacking sequences commonly seen in aerospace applications or new stacking proposals in conjunction with various tests, such as tensile, compaction, and friction testing, has the potential to create an

extensive database. This database would be invaluable in understanding the impact of varying stacking sequences on the performance of composite components under different scenarios. Moreover, the development of algorithms that establish a connection between stacking sequence and processing conditions in order to estimate mechanical reactions could be highly advantageous.

- The two-point bending test device designed in this study has substantial potential for producing data related to imperfections in the thermoforming process. The device provides diverse evaluative options due to its capacity to handle various process variables, including specimen dimensions, stacking sequences, torque, and temperature. Given that bending plays a crucial role in thermoforming, this device can be used to predict the behaviour of a laminate when subjected to different combinations of process variables during thermoforming moulding. Furthermore, its capacity to provide real-time visualisation of the development of wrinkles in the laminate enables both qualitative and quantitative evaluation of this frequent defect. Better integration of this equipment into this research could greatly improve our comprehension of the behaviour of uncured prepreg laminates during thermoforming.
- It is crucial to further investigate the capabilities and limitations of the numerical model in order to find potential areas for improvement. An effective initial step would be to perform simulations utilising a single element, similar to the one described in Section 4.2.1, but with varying fibre orientations as considered in Section 3.5. This technique would facilitate a more thorough comprehension of the model's suitability across different laminate configurations.
- Although the generalised Maxwell technique yielded satisfactory outcomes in our specific scenario, it is important to acknowledge the existence of several models that can be employed to represent mechanical responses, including viscoelastic effects. Exploring the implementation of alternative models in our scenario could be beneficial for research. The Kelvin-Voigt model, Standard Linear Solid model, and Burgers model, among others, could provide enhanced computational representation of the thermoforming process.
- Ultimately, it is clear that simulations require a more precise representation of the interactions between layers in laminates. Although the Benzeggagh-Kenane model has potential utility, it may not be adequate to rely exclusively on friction coefficients within this model. Usually, the parameters for this model are supplied with fracture resistance values acquired from tests such as the Double Cantilever Beam (DCB) and End-Notch Flexure (ENF), which are used to determine the interlaminar fracture resistance in Modes I and II. Nevertheless, performing these tests on uncured prepreg composite laminates is impractical, indicating the necessity for other approaches. A potential suggestion is to do peel adhesion tests, as their outcomes may fit better the Benzeggagh-Kenane model compared to friction parameters.

References

Adams, D. O., Moriarty, J. M., Gallegos, A. M., & Adams, D. F. (2007). The v-notched rail shear test. *Journal of composite materials*, *41*(3), 281–297.

Ahmed, A., Zillur Rahman, M., Ou, Y., Liu, S., Mobasher, B., Guo, S., & Zhu, D. (2021). A review on the tensile behavior of fiber-reinforced polymer composites under varying strain rates and temperatures. *Construction and Building Materials*, *294*, 123565. https://doi.org/10.1016/J.CONBUILDMAT.2021.123565

Alshahrani, H., & Hojjati, M. (2017). Bending behavior of multilayered textile composite prepregs: Experiment and finite element modeling. *Materials and Design*, *124*, 211–224. https://doi.org/10.1016/j.matdes.2017.03.077

Asim, M., Saba, N., Jawaid, M., Nasir, M., Pervaiz, M., & Alothman, O. Y. (2018). A Review on Phenolic Resin and its Composites. *Current Analytical Chemistry*, *14*(3), 185–197. https://doi.org/10.2174/1573411013666171003154410

ASTM D3039. (2014). Standard Test Method for Tensile Properties of Polymer Matrix Composite Materials D3039.

Aveiga, D., Gómez, D. G., Mocerino, D., López-Romano, B., & González, C. (2023). Friction Resistance of Uncured Carbon/Epoxy Prepregs under Thermoforming Process Conditions: Experiments and Modelling. *Journal of Manufacturing and Materials Processing*, *7*(1), 14. https://doi.org/10.3390/jmmp7010014

Bacon, R. (1960). Growth, structure, and properties of graphite whiskers. *Journal of Applied Physics*, *31*(2), 283–290. https://doi.org/10.1063/1.1735559

Balasubramanian, K., Sultan, M. T., & Rajeswari, N. (2018). Manufacturing techniques of composites for aerospace applications. In *Sustainable composites for aerospace applications* (pp. 55–67). Elsevier. https://doi.org/10.1016/B978-0-08-102131-6.00004-9

Barnes, J. A., & Cogswell, F. N. (1989). Transverse flow processes in continuous fibre-reinforced thermoplastic composites. *Composites*, *20*(1), 38–42. https://doi.org/10.1016/0010-4361(89)90680-0

Belnoue, J. P., Nixon-Pearson, O. J., Ivanov, D., & Hallett, S. R. (2016). A novel hyper-viscoelastic model for consolidation of toughened prepregs under processing conditions. *Mechanics of Materials*, *97*, 118–134. https://doi.org/10.1016/j.mechmat.2016.02.019

Belnoue, J. P., Nixon-Pearson, O. J., Thompson, A. J., Ivanov, D. S., Potter, K. D., & Hallett, S. R. (2018a). Consolidation-driven defect generation in thick composite parts. *Journal of Manufacturing Science and Engineering, Transactions of the ASME*, *140*(7). https://doi.org/10.1115/1.4039555

Belnoue, J. P., Nixon-Pearson, O. J., Thompson, A. J., Ivanov, D. S., Potter, K. D., & Hallett, S. R. (2018b). Consolidation-driven defect generation in thick composite parts. *Journal of Manufacturing Science and Engineering, Transactions of the ASME*, *140*(7). https://doi.org/10.1115/1.4039555

Belnoue, J. P., Mesogitis, T., Nixon-Pearson, O. J., Kratz, J., Ivanov, D. S., Partridge, I. K., Potter, K. D., & Hallett, S. R. (2017). Understanding and predicting defect formation in automated fibre placement pre-preg laminates. *Composites Part A: Applied Science and Manufacturing*, *102*, 196–206. https://doi.org/10.1016/J.COMPOSITESA.2017.08.008

Berry, D. (2002). Use of victrex® PEEK™ thermoplastic to drive new designs, processing flexibility, and cost reduction in aerospace components. https://doi.org/10.4271/2002-01-2923

Bhudolia, S. K., Gohel, G., Leong, K. F., & Islam, A. (2020). Advances in Ultrasonic Welding of Thermoplastic Composites: A Review. *Materials 2020, Vol. 13, Page 1284*, *13*(6), 1284. https://doi.org/10.3390/MA13061284

Bloom, L. D., Wang, J., & Potter, K. D. (2013). Damage progression and defect sensitivity: An experimental study of representative wrinkles in tension. *Composites Part B: Engineering*, *45*(1), 449–458. https://doi.org/10.1016/J.COMPOSITESB.2012.05.021

Boisse, P., Colmars, J., Hamila, N., Naouar, N., & Steer, Q. (2018). Bending and wrinkling of composite fiber preforms and prepregs. A review and new developments in the draping simulations. *Composites Part B: Engineering*, *141*, 234–249. https://doi.org/10.1016/J.COMPOSITESB.2017.12.061

Boisse, P., Hamila, N., Vidal-Sallé, E., & Dumont, F. (2011). Simulation of wrinkling during textile composite reinforcement forming. Influence of tensile, in-plane shear and bending stiffnesses. *Composites Science and Technology*, *71*(5), 683–692. https://doi.org/10.1016/j.compscitech.2011.01.011

Bonet, J., & Burton, A. J. (1998). A simple orthotropic, transversely isotropic hyperelastic constitutive equation for large strain computations. *Computer Methods in Applied Mechanics and Engineering*, *162*, 151–164. https://doi.org/10.1016/S0045-7825(97)00339-3

Broughton, W., Kumosa, M., & Hull, D. (1990). Analysis of the iosipescu shear test as applied to unidirectional carbon-fibre reinforced composites. *Composites Science and Technology*, *38*(4), 299–325.

Browning, C., & Mair, A. (1974). Analysis of the flexure test for laminated composite materials. *Composite materials: Testing and design*, *546*, 30–45.

Buragohain, M. K. (2017, August). Manufacturing Methods for Polymer Matrix Composites. In *Composite structures* (pp. 489–536). CRC Press. https://doi.org/10.1201/9781315268057-10

Burstein, L. (2008). Effect of sinusoidal roughened surfaces on pressure in lubricating film. *International Journal of Surface Science and Engineering*, *2*(1-2), 52–70. https://doi.org/10.1504/IJSURFSE.2008.018968

Cai, Z., & Gutowski, T. (1992). The 3-D Deformation Behavior of a Lubricated Fiber Bundle. *Journal of Composite Materials*, *26*(8), 1207–1237. https://doi.org/10.1177/002199839202600808

Cantwell, W. J., & Morton, J. (1992). The significance of damage and defects and their detection in composite materials: A review. The Journal of Strain Analysis for Engineering Design. *The Journal of Strain Analysis for Engineering Design*, *27*(1), 29–42.

Centea, T., Grunenfelder, L. K., & Nutt, S. R. (2015). A review of out-of-autoclave prepregs – Material properties, process phenomena, and manufacturing considerations. *Composites Part A: Applied Science and Manufacturing*, *70*, 132–154. https://doi.org/10.1016/J.COMPOSITESA.2014.09.029

Chen, X., Wang, X., Wang, L., Shi, Q., & Li, Y. (2018). Uncertainty quantification of multi-dimensional parameters for composite laminates based on grey mathematical theory. *Applied Mathematical Modelling*, *55*, 299–313.

Chohan, J. S., Boparai, K. S., Singh, R., & Hashmi, M. S. (2020). Manufacturing techniques and applications of polymer matrix composites: a brief review. *https://doi.org/10.1080/2374068X.2020.183* *8*(1), 884–894. https://doi.org/10.1080/2374068X.2020.1835012

Cornelissen, B., Sachs, U., Rietman, B., & Akkerman, R. (2014). Dry friction characterisation of carbon fibre tow and satin weave fabric for composite applications. *Composites Part A: Applied Science and Manufacturing*, *56*, 127–135. https://doi.org/10.1016/J.COMPOSITESA.2013.10.006

D3039, A. (2008). Standard test method for tensile properties of polymer matrix composite.

D3410, A. (1987). Standard test method for compressive properties of unidirectional or crossply fiber-resin composites. *American Society for Testing and Materials*.

D3518, A. (2007). Standard test method for in-plane shear response of polymer matrix composite materials by tensile test of a±45° laminate.

D5379, A. (2012). Astm d5379/d5379m-12-standard test method for shear properties of composite materials by the v-notched beam method.

D6641, A. (2014). D6641/d6641m-14. *Standard Test Method for Compressive Properties of Polymer Matrix Composite Materials Using a Combined Loading Compression (CLC) Test Fixture*.

D695, A. (2015). Standard test method for compressive properties of rigid plastics.

D7078, A. (2005). D7078/d7078m-19 standard test method for shear properties of composite materials by v-notched rail shear method.

D7264, A. (2015). D7264 standard test method for flexural properties of polymer composite materials. *American Society for Testing and Materials, Philadelphia*.

Daso, F. O. (2019). *Manufacture of Aerospace-Grade Thermoset and Thermoplastic Composites via Nanoengineered Thermal Processing* [Doctoral dissertation, Massachusetts Institute of Technology].

de Bruyne, N. A. (1937). Plastic Materials for Aircraft Construction. *The Journal of the Royal Aeronautical Society*, *41*(319), 523–590. https://doi.org/10.1017/s0368393100107655

Denault, J., & Dumouchel, M. (1998). Consolidation process of PEEK/carbon composite for aerospace applications. *Advanced Performance Materials*, *5*(1-2), 83–96. https://doi.org/10.1023/A:1008638105370/METRICS

Dörr, D., Schirmaier, F. J., Henning, F., & Kärger, L. (2017). A viscoelastic approach for modeling bending behavior in finite element forming simulation of continuously fiber reinforced composites. *Composites Part A: Applied Science and Manufacturing*, *94*, 113–123. https://doi.org/10.1016/J.COMPOSITESA.2016.11.027

Dutta, A., Hagnell, M. K., & Åkermo, M. (2023). Interply friction between unidirectional carbon/epoxy prepreg plies: Influence of fibre orientation. *Composites Part A: Applied Science and Manufacturing*, *166*, 107375. https://doi.org/10.1016/J.COMPOSITESA.2022.107375

Duvaut, G., Terrel, G., Léné, F., & Verijenko, V. E. (2000). Optimization of fiber reinforced composites. *Composite Structures*, *48*(1-3), 83–89. https://doi.org/10.1016/S0263-8223(99)00077-X

Ekuase, O. A., Anjum, N., Eze, V. O., & Okoli, O. I. (2022). A Review on the Out-of-Autoclave Process for Composite Manufacturing. *Journal of Composites Science 2022, Vol. 6, Page 172*, *6*(6), 172. https://doi.org/10.3390/JCS6060172

Engmann, J., Servais, C., & Burbidge, A. S. (2005). Squeeze flow theory and applications to rheometry: A review. *Journal of Non-Newtonian Fluid Mechanics*, *132*(1-3), 1–27. https://doi.org/10.1016/j.jnnfm.2005.08.007

Eric Pierrejean. (2022). *Composites Sustainability Report 2022* (tech. rep.). JEC Group. Paris. https://doi.org/978-2-490263-09-7

Ersoy, N., Potter, K., Wisnom, M. R., & Clegg, M. J. (2005). An experimental method to study the frictional processes during composites manufacturing. *Composites Part A: Applied Science and Manufacturing*, *36*(11), 1536–1544. https://doi.org/10.1016/j.compositesa.2005.02.010

Falzon, B. G., & Pierce, R. S. (2020). Thermosetting Composite Materials in Aerostructures. In S. Pantelakis & K. Tserpes (Eds.), *Revolutionizing aircraft materials and processes* (pp. 57–86). Springer International Publishing. https://doi.org/10.1007/978-3-030-35346-9{_}3

Fernberg, P., Gong, G., Mannberg, P., & Tsampas, S. (2018). Development of novel high Tg polyimide-based composites. Part I: RTM processing properties. *Journal of Composite Materials*, *52*(2), 253–260. https://doi.org/10.1177/0021998317705705

Fetfatsidis, K. A., Gamache, L. M., Gorczyca, J. L., Sherwood, J. A., Jauffrès, D., & Chen, J. (2013). Design of an apparatus for measuring tool/fabric and fabric/fabric friction of woven-fabric composites during the thermostamping process. *International Journal of Material Forming*, *6*(1), 1–11. https://doi.org/10.1007/s12289-011-1058-3

Ford, C., & Mitchell, C. (1963). Fibrous Graphite.

Garcia-Gil, R. (2003). Forming and consolidation of textile composites, 194.

Ghiasi, H., Fayazbakhsh, K., Pasini, D., & Lessard, L. (2010). Optimum stacking sequence design of composite materials Part II: Variable stiffness design. *Composite Structures*, *93*(1), 1–13. https://doi.org/10.1016/j.compstruct.2010.06.001

Gibson, A. G., & Månson, J. A. (1992). Impregnation technology for thermoplastic matrix composites. *Composites Manufacturing*, *3*(4), 223–233. https://doi.org/10.1016/0956-7143(92)90110-G

Gorczyca-Cole, J. L., Sherwood, J. A., & Chen, J. (2007). A friction model for thermostamping commingled glass–polypropylene woven fabrics. *Composites Part A: Applied Science and Manufacturing*, *38*(2), 393–406. https://doi.org/10.1016/J.COMPOSITESA.2006.03.006

Goyal, S., & Cochran, E. W. (2022). Cyanate ester composites to improve thermal performance: a review. *Polymer International*, *71*(5), 583–589. https://doi.org/10.1002/pi.6373

Groves, D. J. (1989). A characterization of shear flow in continuous fibre thermoplastic laminates. *Composites*, *20*(1), 28–32. https://doi.org/10.1016/0010-4361(89)90678-2

Gutowski, T. G., Cai, Z., Bauer, S., Boucher, D., Kingery, J., & Wineman, S. (1987). Consolidation Experiments for Laminate Composites. *Journal of Composite Materials*, *21*(7), 650–669. https://doi.org/10.1177/002199838702100705

Gutowski, T. G., Morigaki, T., & Cai, Z. (1987). The Consolidation of Laminate Composites. *Journal of Composite Materials*, *21*(2), 172–188. https://doi.org/10.1177/002199838702100207

Guzman-Maldonado, E., Hamila, N., Boisse, P., & Bikard, J. (2015). Thermomechanical analysis, modelling and simulation of the forming of pre-impregnated thermoplastics composites. *Composites Part A: Applied Science and Manufacturing*, *78*, 211–222. https://doi.org/10.1016/J.COMPOSITESA.2015.08.017

Guzman-Maldonado, E., Hamila, N., Naouar, N., Moulin, G., & Boisse, P. (2016). Simulation of thermoplastic prepreg thermoforming based on a visco-hyperelastic model and a thermal homogenization. *Materials and Design*, *93*, 431–442. https://doi.org/10.1016/j.matdes.2015.12.166

Guzman-Maldonado, E., Wang, P., Hamila, N., & Boisse, P. (2019). Experimental and numerical analysis of wrinkling during forming of multi-layered textile composites. *Composite Structures*, *208*, 213–223. https://doi.org/10.1016/J.COMPSTRUCT.2018.10.018

Haanappel, S. (2013). *Forming of UD fibre reinforced thermoplastics*.

Hallander, P., Sjölander, J., & Åkermo, M. (2015). Forming induced wrinkling of composite laminates with mixed ply material properties; an experimental study. *Composites Part A: Applied Science and Manufacturing*, *78*, 234–245. https://doi.org/10.1016/j.compositesa.2015.08.025

Hallander, P., Sjölander, J., Petersson, M., & Åkermo, M. (2016). Interface manipulation towards wrinkle-free forming of stacked UD prepreg layers. *Composites Part A: Applied Science and Manufacturing*, *90*, 340–348. https://doi.org/10.1016/j.compositesa.2016.07.013

Hamerton, I., & Mooring, L. (2012). The Use of Thermosets in Aerospace Applications. *Thermosets: Structure, Properties and Applications*, 189–227. https://doi.org/10.1533/9780857097637.2.189

Hamidi, Y. K., & Altan, M. C. (2017). Process induced defects in liquid molding processes of composites. *International Polymer Processing*, *32*(5), 527–544. https://doi.org/10.3139/217.3444

Hassan, M. H. (2021). A mini review on manufacturing defects and performance assessments of complex shape prepreg-based composites. *International Journal of Advanced Manufacturing Technology*, *115*(11-12), 3393–3408. https://doi.org/10.1007/s00170-021-07421-8

Henriquez, R. G., & Mertiny, P. (2018). 3.21 Filament Winding Applications. *Comprehensive Composite Materials II*, 556–577. https://doi.org/10.1016/B978-0-12-803581-8.10313-3

Heshmat, H., & Walton, J. F. (2016). Starved Hydrodynamic Gas Foil Bearings-Experiment, Micromechanical Phenomenon, and Hypotheses. *Journal of Tribology*, *138*(4), 1–14. https://doi.org/10.1115/1.4032911

Holmes, M. (2019). Additive manufacturing continues composites market growth. *Reinforced Plastics*, *63*(6), 296–301. https://doi.org/10.1016/J.REPL.2018.12.070

Hsiao, K.-T., & Heider, D. (2012). Vacuum assisted resin transfer molding (VARTM) in polymer matrix composites. *Manufacturing Techniques for Polymer Matrix Composites (PMCs)*, 310–347. https://doi.org/10.1533/9780857096258.3.310

Hsissou, R., Bekhta, A., Dagdag, O., El Bachiri, A., Rafik, M., & Elharfi, A. (2020). Rheological properties of composite polymers and hybrid nanocomposites. *Heliyon*, *6*(6), e04187. https://doi.org/10.1016/j.heliyon.2020.e04187

Hubert, P., & Poursartip, A. (2001a). A method for the direct measurement of the fibre bed compaction curve of composite prepregs. *Composites Part A: Applied Science and Manufacturing*, *32*(2), 179–187. https://doi.org/10.1016/S1359-835X(00)00143-3

Hubert, P., & Poursartip, A. (2001b). Method for the direct measurement of the fibre bed compaction curve of composite prepregs. *Composites Part A: Applied Science and Manufacturing*, *32*(2), 179–187. https://doi.org/10.1016/S1359-835X(00)00143-3

Hubert, P., & Poursartip, A. (1998a). A Review of Flow and Compaction Modelling Relevant to Thermoset Matrix Laminate Processing. *Journal of Reinforced Plastics and Composites*, *17*(4), 286–318. https://doi.org/10.1177/073168449801700402

Hubert, P., & Poursartip, A. (1998b). A review of flow and compaction modelling relevant to thermoset matrix laminate processing. *Journal of Reinforced Plastics and Composites*, *17*(4), 286–318. https://doi.org/10.1177/073168449801700402

Hubert, P., Vaziri, R., & Poursartip, A. (1999). A two-dimensional flow model for the process simulation of complex shape composite laminates. *International Journal for Numerical Methods in Engineering*, *44*(1), 1–26. https://doi.org/10.1002/(SICI)1097-0207(19990110)44:1<1::AID-NME481>3.0.CO;2-K

Joven, R., Tavakol, B., Rodriguez, A., Guzman, M., & Minaie, B. (2013). Characterization of shear stress at the tool-part interface during autoclave processing of prepreg composites. *Journal of Applied Polymer Science*, *129*(4), 2017–2028. https://doi.org/10.1002/app.38909

Kaliske, M. (2000). A formulation of elasticity and viscoelasticity for fibre reinforced material at small and finite strains. *Computer Methods in Applied Mechanics and Engineering*, *185*, 225–243. https://doi.org/10.1016/S0045-7825(99)00261-3

Kaliske, M., & Rothert, H. (1997). Formulation and implementation of three-dimensional viscoelasticity at small and finite strains. *Computational Mechanics*, *19*, 228–239. https://doi.org/10.1007/S004660050171/METRICS

Karami, G., & Garnich, M. (2005). Effective moduli and failure considerations for composites with periodic fiber waviness. *Composite Structures*, *67*(4), 461–475. https://doi.org/10.1016/J.COMPSTRUCT.2004.02.005

Kaushik, V., & Raghavan, J. (2010). Experimental study of tool-part interaction during autoclave processing of thermoset polymer composite structures. *Composites Part A: Applied Science and Manufacturing*, *41*(9), 1210–1218. https://doi.org/10.1016/j.compositesa.2010.05.003

Kelly, P. A. (2011). A viscoelastic model for the compaction of fibrous materials. *Journal of the Textile Institute*, *102*(8), 689–699. https://doi.org/10.1080/00405000.2010.515103

Kim, J. Y., Hwang, Y. T., Baek, J. H., Song, W. Y., & Kim, H. S. (2021). Study on inter-ply friction between woven and unidirectional prepregs and its effect on the composite forming process. *Composite Structures*, *267*(March), 113888. https://doi.org/10.1016/j.compstruct.2021.113888

Kiskan, B., Ghosh, N. N., & Yagci, Y. (2011). Polybenzoxazine-based composites as high-performance materials. *Polymer International*, *60*(2), 167–177. https://doi.org/10.1002/pi.2961

Koumoulos, E. P., Trompeta, A. F., Santos, R. M., Martins, M., Dos Santos, C. M., Iglesias, V., Böhm, R., Gong, G., Chiminelli, A., Verpoest, I., Kiekens, P., & Charitidis, C. A. (2019). Research and Development in Carbon Fibers and Advanced High-Performance Composites Supply Chain in Europe: A Roadmap for Challenges and the Industrial Uptake. *Journal of Composites Science 2019, Vol. 3, Page 86*, *3*(3), 86. https://doi.org/10.3390/JCS3030086

Kratz, J., Galvez-Hernandez, P., Pickard, L. R., Belnoue, J., & Potter, K. (2021). Lab-based in-situ micro-CT observation of gaps in prepreg laminates during consolidation and cure. *Composites Part A: Applied Science and Manufacturing*, *140*, 106180. https://doi.org/10.1016/J.COMPOSITESA.2020.106180

Larberg, Y. R., & Åkermo, M. (2011). On the interply friction of different generations of carbon/epoxy prepreg systems. *Composites Part A: Applied Science and Manufacturing*, *42*(9), 1067–1074. https://doi.org/10.1016/j.compositesa.2011.04.010

Lebrun, G., Bureau, M. N., & Denault, J. (2004). Thermoforming-stamping of Continuous Glass Fiber/Polypropylene Composites: Interlaminar and Tool-Laminate Shear Properties. *Journal of Thermoplastic Composite Materials*, *17*(2), 137–165. https://doi.org/10.1177/0892705704035411

Lee, J. M., Kim, B. M., Lee, C. J., & Ko, D. C. (2017). A characterisation of tool-ply friction behaviors in thermoplastic composite. *Procedia Engineering*, *207*, 90–94. https://doi.org/10.1016/j.proeng.2017.10.743

Lee, S., & Munro, M. (1986). Evaluation of in-plane shear test methods for advanced composite materials by the decision analysis technique. *Composites*, *17*(1), 13–22. https://doi.org/10.1016/0010-4361(86)90729-9

Lee, W. I., & Springer, G. S. (1987). A Model of the Manufacturing Process of Thermoplastic Matrix Composites. *Journal of Composite Materials*, *21*(11), 1017–1055. https://doi.org/10.1177/002199838702101103

Li, Y., Xiao, Y., Yu, L., Ji, K., & Li, D. (2022). A review on the tooling technologies for composites manufacturing of aerospace structures: materials, structures and processes. *Composites Part A: Applied Science and Manufacturing*, *154*, 106762. https://doi.org/10.1016/J.COMPOSITESA.2021.106762

Liang, B., Hamila, N., Peillon, M., & Boisse, P. (2014). Analysis of thermoplastic prepreg bending stiffness during manufacturing and of its influence on wrinkling simulations. *Composites Part A: Applied Science and Manufacturing*, *67*, 111–122. https://doi.org/10.1016/j.compositesa.2014.08.020

Lightfoot, J. S., Wisnom, M. R., & Potter, K. (2013). A new mechanism for the formation of ply wrinkles due to shear between plies. *Composites Part A: Applied Science and Manufacturing*, *49*, 139–147. https://doi.org/10.1016/J.COMPOSITESA.2013.03.002

Liu, D., Chen, P., Su, J., Ning, B., Liu, S., & Yan, J. (2022). Compression properties of unidirectional over-braided multilayer composites. *Composites Science and Technology*, *230*, 109791. https://doi.org/https://doi.org/10.1016/j.compscitech.2022.109791

Liu, S.-J. (2012). Injection molding in polymer matrix composites. *Manufacturing Techniques for Polymer Matrix Composites (PMCs)*, 15–46. https://doi.org/10.1533/9780857096258.1.13

Lubarda, V. A., & Chen, M. C. (2008). On the elastic moduli and compliances of transversely isotropic and orthotropic materials. *Journal of Mechanics of Materials and Structures*, *3*, 153–171. https://doi.org/10.2140/JOMMS.2008.3.153

Mallick, P. (2007). Fiber-Reinforced Composites : Materials, Manufacturing, and Design, Third Edition. https://doi.org/10.1201/9781420005981

Mangino, E., Carruthers, J., & Pitarresi, G. (2007). The future use of structural composite materials in the automotive industry. *International Journal of Vehicle Design*, *44*(3-4), 211–232. https://doi.org/10.1504/IJVD.2007.013640

Marsh, G. (2011). Automating aerospace composites production with fibre placement. *Reinforced Plastics*, *55*(3), 32–37. https://doi.org/10.1016/S0034-3617(11)70075-3

Martin, C. J., Seferis, J. C., & Wilhelm, M. A. (1996). Frictional resistance of thermoset prepregs and its influence on honeycomb composite processing. *Composites Part A: Applied Science and Manufacturing*, *27*(10), 943–951. https://doi.org/10.1016/1359-835X(96)00037-1

Martin, P. (2009, January). Thermoforming of polymers. In *Advances in polymer processing* (pp. 352–383). Elsevier. https://doi.org/10.1533/9781845696429.3.352

Mesogitis, T. S., Skordos, A. A., & Long, A. C. (2014). Uncertainty in the manufacturing of fibrous thermosetting composites: A review. *Composites Part A: Applied Science and Manufacturing*, *57*, 67–75. https://doi.org/10.1016/J.COMPOSITESA.2013.11.004

Morris, S. R., & Sun, C. T. (1994). An investigation of interply slip behaviour in AS4/PEEK at forming temperatures. *Composites Manufacturing*, *5*(4), 217–224. https://doi.org/10.1016/0956-7143(94)90136-8

Mouritz, A. P., Gellert, E., Burchill, P., & Challis, K. (2001). Review of advanced composite structures for naval ships and submarines. *Composite Structures*, *53*(1), 21–42. https://doi.org/10.1016/S0263-8223(00)00175-6

Muc, A., Romanowicz, P., & Chwał, M. (2019). Description of the Resin Curing Process—Formulation and Optimization. *Polymers*, *11*(1), 127. https://doi.org/10.3390/polym11010127

Mulvihill, D. M., & Sutcliffe, M. P. (2017). Effect of tool surface topography on friction with carbon fibre tows for composite fabric forming. *Composites Part A: Applied Science and Manufacturing*, *93*, 199–206. https://doi.org/10.1016/j.compositesa.2016.10.017

Murtagh, A. M., Lennon, J. J., & Mallon, P. J. (1995). Surface friction effects related to pressforming of continuous fibre thermoplastic composites. *Composites Manufacturing*, *6*(3-4), 169–175. https://doi.org/10.1016/0956-7143(95)95008-M

Naresh, K., Salem, A., Khan, K. A., Cantwell, W. J., & Umer, R. (2022). Isothermal compaction-creep-recovery behavior and statistical void analysis of prepregs under various process parameters. *Composites Part A: Applied Science and Manufacturing*, *152*(October 2021), 106663. https://doi.org/10.1016/j.compositesa.2021.106663

Naresh, K., Khan, K. A., Cantwell, W. J., & Umer, R. (2021). Viscoelastic and cyclic compaction response of prepregs tested under isothermal temperatures and various compaction speeds. *Polymer Composites*, *42*(12), 6928–6940. https://doi.org/10.1002/pc.26351

Netzel, C., Hoffmann, D., Battley, M., Hubert, P., & Bickerton, S. (2021). Effects of environmental conditions on uncured prepreg characteristics and their effects on defect generation during autoclave processing. *Composites Part A: Applied Science and Manufacturing*, *151*(September), 106636. https://doi.org/10.1016/j.compositesa.2021.106636

Newcomb, B. A. (2016). Processing, structure, and properties of carbon fibers. *Composites Part A: Applied Science and Manufacturing*, *91*, 262–282. https://doi.org/10.1016/J.COMPOSITESA.2016.10.018

Nikas, G. (2010). *Recent developements in wear prevention, friction, and lubrication*. Research Signpost.

Nixon-Pearson, O., Belnoue, J.-H., Ivanov, D., Potter, K., & Hallett, S. (2017). An experimental investigation of the consolidation behaviour of uncured prepregs under processing conditions. *Journal of Composite Materials*, *51*(13), 1911–1924. https://doi.org/10.1177/0021998316665681

Nunes, J., Pouzada, A., & Bernardo, C. (2002). The use of a three-point support flexural test to predict the stiffness of anisotropic composite plates in bending. *Polymer testing*, *21*(1), 27–33.

ÓBrádaigh, C. M., McGuinness, G. B., & Pipes, R. B. (1993). Numerical analysis of stresses and deformations in composite materials sheet forming: central indentation of a circular sheet. *Composites Manufacturing*, *4*(2), 67–83. https://doi.org/10.1016/0956-7143(93)90074-I

Offringa, A. R. (1996). Thermoplastic composites—rapid processing applications. *Composites Part A: Applied Science and Manufacturing*, *27*(4), 329–336. https://doi.org/10.1016/1359-835X(95)00048-7

Paimushin, V. N., Kholmogorov, S. A., Makarov, M. V., Tarlakovskii, D. V., & Lukaszewicz, A. (2019). Mechanics of fiber composites: Forms of loss of stability and fracture of test specimens resulting from three-point bending tests. *ZAMM - Journal of Applied Mathematics and Mechanics / Zeitschrift für Angewandte Mathematik und Mechanik*, *99*, e201800063. https://doi.org/10.1002/zamm.201800063

Pantelakis, S. (2020). *Historical Development of Aeronautical Materials*. https://doi.org/10.1007/978-3-030-35346-9{_}1

Parandoush, P., & Lin, D. (2017). A review on additive manufacturing of polymer-fiber composites. *Composite Structures*, *182*, 36–53. https://doi.org/10.1016/J.COMPSTRUCT.2017.08.088

Pasco, C., Khan, M., Gupta, J., & Kendall, K. (2019). Experimental investigation on interply friction properties of thermoset prepreg systems. *Journal of Composite Materials*, *53*(2), 227–243. https://doi.org/10.1177/0021998318781706

Qiao, Y., Fring, L. D., Pallaka, M. R., & Simmons, K. L. (2022). A review of the fabrication methods and mechanical behavior of continuous thermoplastic polymer fiber–thermoplastic polymer matrix composites. *Polymer Composites*. https://doi.org/10.1002/PC.27139

Rajak, D. K., Pagar, D. D., Menezes, P. L., & Linul, E. (2019). Fiber-Reinforced Polymer Composites: Manufacturing, Properties, and Applications. *Polymers 2019, Vol. 11, Page 1667*, *11*(10), 1667. https://doi.org/10.3390/POLYM11101667

Ramaswamy Setty, J., Upadhya, A., Dayananda, G., Kamalakannan, G., & Christopher Daniel, J. (2011). Autoclaves for aerospace applications: Issues and challenges. *International Journal of Aerospace Engineering*. https://doi.org/10.1155/2011/985871

Rashidi, A., Crawford, B., Olfatbakhsh, T., & Milani, A. S. (2021). A mixed lubrication model for inter-ply friction behaviour of uncured fabric prepregs. *Composites Part A: Applied Science and Manufacturing*, *149*(June), 106571. https://doi.org/10.1016/j.compositesa.2021.106571

Rashidi, A., Keegan, C., & Milani, A. S. (2019). Analysis of inter-ply friction in consolidation process of thermoset woven prepregs. *AIP Conference Proceedings*, *2113*(July), 1–7. https://doi.org/10.1063/1.5112528

Rashidi, A., Montazerian, H., Yesilcimen, K., & Milani, A. S. (2020). Experimental characterization of the inter-ply shear behavior of dry and prepreg woven fabrics: Significance of mixed lubrication mode during thermoset composites processing. *Composites Part A: Applied Science and Manufacturing*, *129*, 105725. https://doi.org/10.1016/J.COMPOSITESA.2019.105725

Rogers, T. G. (1989a). Rheological characterization of anisotropic materials. *Composites*, *20*(1), 21–27. https://doi.org/10.1016/0010-4361(89)90677-0

Rogers, T. G. (1989b). Squeezing flow of fibre-reinforced viscous fluids. *Journal of Engineering Mathematics*, *23*(1), 81–89. https://doi.org/10.1007/BF00058434

Ropers, S., Kardos, M., & Osswald, T. A. (2016). A thermo-viscoelastic approach for the characterization and modeling of the bending behavior of thermoplastic composites. *Composites Part A: Applied Science and Manufacturing*, *90*, 22–32. https://doi.org/10.1016/J.COMPOSITESA.2016.06.016

Rosen, B. W. (1972). A simple procedure for experimental determination of the longitudinal shear modulus of unidirectional composites. *Journal of Composite Materials*, *6*, 552–554. https://doi.org/10.1177/002199837200600310

Rueden, C. T., Schindelin, J., Hiner, M. C., DeZonia, B. E., Walter, A. E., Arena, E. T., & Eliceiri, K. W. (2017). ImageJ2: ImageJ for the next generation of scientific image data. *BMC Bioinformatics*, *18*(1), 529. https://doi.org/10.1186/s12859-017-1934-z

Russo, A., Zarrelli, M., Sellitto, A., & Riccio, A. (2019). Fiber Bridging Induced Toughening Effects on the Delamination Behavior of Composite Stiffened Panels under Bending Loading: A Numerical/Experimental Study. *Materials 2019, Vol. 12, Page 2407*, *12*(15), 2407. https://doi.org/10.3390/MA12152407

Saba, N., Jawaid, M., & Sultan, M. T. (2019). An overview of mechanical and physical testing of composite materials. *Mechanical and Physical Testing of Biocomposites, Fibre-Reinforced Composites and Hybrid Composites*, 1–12. https://doi.org/10.1016/B978-0-08-102292-4.00001-1

Sachs, U., Akkerman, R., Fetfatsidis, K., Vidal-Sallé, E., Schumacher, J., Ziegmann, G., Allaoui, S., Hivet, G., Maron, B., Vanclooster, K., & Lomov, S. V. (2014). Characterization of the dynamic friction of woven fabrics: Experimental methods and benchmark results. *Composites Part A: Applied Science and Manufacturing*, *67*, 289–298. https://doi.org/10.1016/J.COMPOSITESA.2014.08.026

Sachs, U. (2014). *Friction and bending in thermoplastic composites forming processes*. https://doi.org/10.3990/1.9789462594838

Scherer, R., & Friedrich, K. (1991). Inter- and intraply-slip flow processes during thermoforming of cf/pp-laminates. *Composites Manufacturing*, *2*(2), 92–96. https://doi.org/10.1016/0956-7143(91)90185-J

Shaik, F., Ramakrishna, M., & Varma, P. D. (2021). A review on fabrication of thermoset prepreg composites using out-of-autoclave technology. *INCAS Bulletin*, *13*(2), 133–149. https://doi.org/10.13111/2066-8201.2021.13.2.13

Shekar, R. I., Kotresh, T. M., Rao, P. M., & Kumar, K. (2009). Properties of high modulus PEEK yarns for aerospace applications. *Journal of Applied Polymer Science*, *112*(4), 2497–2510. https://doi.org/10.1002/APP.29765

Shindo, A. (1964). 130. On the carbonization of polyacrylonitrile fiber. *Carbon*, *1*(3), 391–392. https://doi.org/10.1016/0008-6223(64)90421-X

Shoaib, T., & Espinosa-Marzal, R. M. (2020). Advances in Understanding Hydrogel Lubrication. *Colloids and Interfaces*, *4*(4), 54. https://doi.org/10.3390/colloids4040054

Shuler, S. F., & Advani, S. G. (1996). Transverse squeeze flow of concentrated aligned fibers in viscous fluids. *Journal of Non-Newtonian Fluid Mechanics*, *65*(1), 47–74. https://doi.org/10.1016/0377-0257(96)01440-1

Skartsis, L., Khomami, B., & Kardos, J. L. (1992). Polymeric flow through fibrous media. *Journal of Rheology*, *36*(4), 589–620. https://doi.org/10.1122/1.550365

Skordos, A., Monroy Aceves, C., & Sutcliffe, M. (2007). A simplified rate dependent model of forming and wrinkling of pre-impregnated woven composites. *Composites Part A: Applied Science and Manufacturing*, *38*(5), 1318–1330. https://doi.org/10.1016/j.compositesa.2006.11.005

Slange, T. S. (2019, March). *Rapid Manufacturing of Tailored Thermoplastic Composites by Automated Lay-up and Stamp Forming, A Study on the Consolidation Mechanisms* [Doctoral dissertation, University of Twente]. https://doi.org/10.3990/1.9789036547284

Soutis, C. (2005). Carbon fiber reinforced plastics in aircraft construction. *Materials Science and Engineering: A*, *412*(1-2), 171–176. https://doi.org/10.1016/J.MSEA.2005.08.064

Spencer, A. J. (2000). Theory of fabric-reinforced viscous fluids. *Composites Part A: Applied Science and Manufacturing*, *31*(12), 1311–1321. https://doi.org/10.1016/S1359-835X(00)00006-3

Sun, J., Gu, Y., Li, M., Ma, X., & Zhang, Z. (2012). Effect of forming temperature on the quality of hot diaphragm formed C-shaped thermosetting composite laminates. *Journal of Reinforced Plastics and Composites*, *31*(16), 1074–1087. https://doi.org/10.1177/0731684412453778

Sun, J., Li, M., Gu, Y., Zhang, D., Li, Y., & Zhang, Z. (2014). Interply friction of carbon fiber/epoxy prepreg stacks under different processing conditions. *Journal of Composite Materials*, *48*(5), 515–526. https://doi.org/10.1177/0021998313476320

Tadini, P., Grange, N., Chetehouna, K., Gascoin, N., Senave, S., & Reynaud, I. (2017). Thermal degradation analysis of innovative PEKK-based carbon composites for high-temperature aeronautical components. *Aerospace Science and Technology*, *65*, 106–116. https://doi.org/10.1016/J.AST.2017.02.011

Talreja, R. (2019). Manufacturing defects in composites and their effects on performance. *Polymer Composites in the Aerospace Industry*, 83–97. https://doi.org/10.1016/B978-0-08-102679-3.00004-6

Technology update: Prepregs. (2003). *Reinforced Plastics*, *47*(6), 20–21. https://doi.org/10.1016/S0034-3617(03)00627-1

Ten Thije, R. H., Akkerman, R., Ubbink, M., & Van Der Meer, L. (2011). A lubrication approach to friction in thermoplastic composites forming processes. *Composites Part A: Applied Science and Manufacturing*, *42*(8), 950–960. https://doi.org/10.1016/j.compositesa.2011.03.023

ten Thije, R. H., Akkerman, R., van der Meer, L., & Ubbink, M. P. (2008). Tool-ply friction in thermoplastic composite forming. *International Journal of Material Forming*, *1*(SUPPL. 1), 953–956. https://doi.org/10.1007/s12289-008-0215-9

Throne, J. (2011). Thermoforming. *Applied Plastics Engineering Handbook: Processing and Materials*, 333–358. https://doi.org/10.1016/B978-1-4377-3514-7.10019-4

Uriya, Y., Ikeuch, K., & Yanagimoto, J. (2014). Cold and warm V-bending test for carbon-fiber-reinforced plastic sheet. *Procedia Engineering*, *81*, 1633–1638. https://doi.org/10.1016/j.proeng.2014.10.203

Vaidya, U. (2015). Thermoplastic composites for aerospace applications. In S. Pantelakis & K. Tserpes (Eds.), *Jec composites magazine* (pp. 41–44, Vol. 52). Springer International Publishing. https://doi.org/10.1007/978-3-030-35346-9{_}4

Valverde, M. A., Belnoue, J. P., Kupfer, R., Kawashita, L. F., Gude, M., & Hallett, S. R. (2021). Compaction behaviour of continuous fibre-reinforced thermoplastic composites under rapid processing conditions. *Composites Part A: Applied Science and Manufacturing*, *149*, 106549. https://doi.org/10.1016/j.compositesa.2021.106549

Velu, R., Vaheed, N. M., Venkatesan, C., Raspall, F., & Krishnan, M. (2019). Experimental investigation on fabrication of thermoset prepreg composites using automated fibre placement process and 3D printed substrate. *Procedia CIRP*, *85*, 296–301. https://doi.org/10.1016/J.PROCIR.2019.09.049

Vogler, T. J., Hsu, S. Y., & Kyriakides, S. (2000). Composite failure under combined compression and shear. *International Journal of Solids and Structures*, *37*(12), 1765–1791. https://doi.org/10.1016/S0020-7683(98)00323-0

Wang, E. L., & Gutowski, T. G. (1991). Laps and gaps in thermoplastic composites processing. *Composites Manufacturing*, *2*(2), 69–78. https://doi.org/10.1016/0956-7143(91)90182-G

Wang, J. L. (2012). Application of Composite Materials on Sports Equipments. *Applied Mechanics and Materials*, *155-156*, 903–906. https://doi.org/10.4028/www.scientific.net/AMM.155-156.903

Wang, L., Xu, P., Peng, X., Zhao, K., & Wei, R. (2019). Characterization of inter-ply slipping behaviors in hot diaphragm preforming: Experiments and modelling. *Composites Part A: Applied Science and Manufacturing*, *121*(September 2018), 28–35. https://doi.org/10.1016/j.compositesa.2019.03.012

Wang, Y., Chea, M. K., Belnoue, J. P.-H., Kratz, J., Ivanov, D. S., & Hallett, S. R. (2020). Experimental characterisation of the in-plane shear behaviour of ud thermoset prepregs under processing conditions. *Composites Part A: Applied Science and Manufacturing*, *133*, 105865.

Wang, Y., Chea, M. K., Belnoue, J. P., Kratz, J., Ivanov, D. S., & Hallett, S. R. (2020). Experimental characterisation of the in-plane shear behaviour of UD thermoset prepregs

under processing conditions. *Composites Part A: Applied Science and Manufacturing*, *133*, 105865. https://doi.org/10.1016/J.COMPOSITESA.2020.105865

Whitney, J., Stansbarger, D., & Howell, H. (1971). Analysis of the rail shear test-applications and limitations. *Journal of Composite Materials*, *5*(1), 24–34.

Wolthuizen, D. J., Schuurman, J., & Akkerman, R. (2014). Forming limits of thermoplastic composites. *Key Engineering Materials*, *611-612*, 407–414. https://doi.org/10.4028/WWW.SCIENTIFIC.NET/KEM.611-612.407

Xu, Y., Guo, L., Zhang, H., Zhai, H., & Ren, H. (2019). Research status, industrial application demand and prospects of phenolic resin. *RSC Advances*, *9*(50), 28924–28935. https://doi.org/10.1039/C9RA06487G

Yokohara, T., Nobukawa, S., & Yamaguchi, M. (2011). Rheological properties of polymer composites with flexible fine fibers. *Journal of Rheology*, *55*(6), 1205–1218. https://doi.org/10.1122/1.3626414

Zhao, Y., Zhang, T., Li, H., & Zhang, B. (2020). Characterization of prepreg-prepreg and prepreg-tool friction for unidirectional carbon fiber/epoxy prepreg during hot diaphragm forming process. *Polymer Testing*, *84*(January), 106440. https://doi.org/10.1016/j.polymertesting.2020.106440